DIELECTRIC PROPERTY-MICROSTRUCTURE RELATION IN $MgTiO_3$-$CaTiO_3$ CERAMICS

A THESIS SUBMITTED TO
THE GRADUATE SCHOOL OF NATURAL AND APPLIED SCIENCES
OF
MIDDLE EAST TECHNICAL UNIVERSITY

BY

MERVE ERGİN ÖREK

IN PARTIAL FULFILLMENT OF THE REQUIREMENTS
FOR
THE DEGREE OF MASTER OF SCIENCE
IN
METALLURGICAL AND MATERIALS ENGINEERING

SEPTEMBER 2019

Approval of the thesis:

DIELECTRIC PROPERTY-MICROSTRUCTURE RELATION IN $MgTiO_3$-$CaTiO_3$ CERAMICS

submitted by **MERVE ERGİN ÖREK** in partial fulfillment of the requirements for the degree of **Master of Science in Metallurgical and Materials Engineering Department, Middle East Technical University** by,

Prof. Dr. Halil Kalıpçılar
Dean, Graduate School of **Natural and Applied Sciences** _____

Prof. Dr. Hakan Gür
Head of Department, **Met. and Mat. Eng.** _____

Prof. Dr. Abdullah Öztürk
Supervisor, **Met. and Mat. Eng., METU** _____

Examining Committee Members:

Prof. Dr. Caner Durucan
Metallurgical and Materials Engineering, METU _____

Prof. Dr. Abdullah Öztürk
Met. and Mat. Eng., METU _____

Assist. Prof. Dr. Mert Efe
Metallurgical and Materials Engineering, METU _____

Prof. Dr. Jongee Park
Metallurgical and Materials Engineering, Atılım University _____

Assoc. Prof. Dr. Volkan Kalem
Metallurgical and Materials Engineering, Konya Technical University _____

Date: 09.09.2019

I hereby declare that all information in this document has been obtained and presented in accordance with academic rules and ethical conduct. I also declare that, as required by these rules and conduct, I have fully cited and referenced all material and results that are not original to this work.

Name, Surname: Merve Ergin Örek

Signature:

ABSTRACT

DIELECTRIC PROPERTY-MICROSTRUCTURE RELATION IN $MgTiO_3$-$CaTiO_3$ CERAMICS

Ergin Örek, Merve
Master of Science, Metallurgical and Materials Engineering
Supervisor: Prof. Dr. Abdullah Öztürk

September 2019, 87 pages

A magnesium titanate - calcium titanate ($MgTiO_3$-$CaTiO_3$) dielectric ceramic with the mole percent composition of 95$MgTiO_3$-5$CaTiO_3$ ($M_{0.95}CT$), was prepared from high purity powders of MgO, $CaCO_3$, and TiO_2 by conventional mixed-oxide route at various sintering temperatures ranging from 1200 to 1300 °C for 2, 4, and 6 h. The maximum densification and optimum dielectric properties were obtained for the $M_{0.95}CT$ ceramic sintered at 1250 °C for 4 h. The bulk density was 3.82 g/cm^3 which corresponds to 97.5% of theoretical density. The dielectric constant and dielectric loss values were 20.6 and 0.0003 (1 kHz-40 MHz), respectively. The effects of small amounts (0.25, 0.50, 0.75, and 1.00 wt%) of $Zn_3B_2O_6$, selected as liquid phase sintering aid, additions on the microstructural development, densification, and dielectric properties of $M_{0.95}CT$ ceramics were also investigated. The results revealed that incorporation of $Zn_3B_2O_6$ caused abnormal grain growth. Densification and dielectric constant of 0.75 wt% $Zn_3B_2O_6$ added $M_{0.95}CT$ ceramic decreased to 92% of theoretical density and 13.8, respectively but, dielectric loss increased to 0.0006. The low-temperature sintered microstructures of pure and $Zn_3B_2O_6$ added $M_{0.95}CT$ ceramics were correlated with the dielectric properties.

Keywords: MgTiO3, CaTiO3, Magnesium Calcium Titanate, Dielectric, Ceramics

ÖZ

$MgTiO_3$-$CaTiO_3$ SERAMİKLERDE DİELEKTRİK ÖZELLİK-MİKROYAPI İLİŞKİSİ

Ergin Örek, Merve
Yüksek Lisans, Metalurji ve Malzeme Mühendisliği
Tez Danışmanı: Prof. Dr. Abdullah Öztürk

Eylül 2019, 87 sayfa

$95MgTiO_3$-$5CaTiO_3$ mol yüzde bileşimine sahip magnezyum titanat - kalsiyum titanat dielektrik seramiği ($M_{0.95}CT$) yüksek saflıktaki MgO, $CaCO_3$, ve TiO_2 tozlarından geleneksel oksit-karışımları yöntemi ile 1200-1300 °C arasında farklı sinterleme sıcaklıkları ve 2, 4 ve 6 saat farklı sinterleme sürelerinde hazırlandı. En yüksek yoğunluk ve optimum dielektrik özellikler 1250 °C'de 4 saat sinterlenen $M_{0.95}CT$ seramiklerinde elde edilmiştir. Bu malzemenin yoğunluğu %97,5 teorik yoğunluğa karşılık gelen 3,82 g/cm^3 olarak ölçülmüştür. Dielektrik sabiti ve kayıp tanjant değerleri sırasıyla 20,7 ve 0,0003 (1 kHz-40 MHz) olarak elde edilmiştir. Sıvı faz sinterleme katkısı olarak seçilen $Zn_3B_2O_6$ bileşiğinin az miktarlardaki (0,25, 0,50, 0,75, ve 1,00 ağ%) katkısının mikroyapı gelişimi, yoğunlaşma, ve dielektrik özellikler üzerine etkisi de araştırılmıştır. Sonuçlar $Zn_3B_2O_6$ katkısının mikroyapı içinde anormal tane büyümesine sebep olduğunu açığa çıkarmıştır. Ağırlıkça %0,75 $Zn_3B_2O_6$ eklenmiş $M_{0.95}CT$ seramiğinin teorik yoğunluğu %92'e, dielektrik sabiti ise 13,8'e düşmüş, fakat dielektrik kayıp faktörünün 0,0006'e artmıştır. Düşük sıcaklıkta sinterlenmiş saf ve $Zn_3B_2O_6$ katkılı $M_{0.95}CT$ seramiklerinin mikroyapı özellikleri ve dielektrik özellikleri ilişkilendirilmiştir.

Anahtar Kelimeler: MgTiO3, CaTiO3, Magnezyum Kalsiyum
Titanat, Dielektrik, Seramik

To my dear husband and my parents,

ACKNOWLEDGMENTS

I would like to thank to all following people who contributed in making this thesis project that was not possible without their precious advices and supports.

I would like to my deepest appreciation to my supervisor Prof. Dr. Abdullah ÖZTÜRK for the continuous support of my thesis research for his patience, encouragement, motivation, advice and guidance.

I am deeply grateful to Prof. Dr. Muharrem TİMUÇİN for his valuable contributions, advices and immense knowledge.

I would also like to thank Assoc. Prof. Özgür BİRER from ASELSAN-REHİS for his patience, guidance and valuable advices.

I also appreciate the help and time spent to Dr. İbrahim ÇAM for dielectric measurements.

I owe my deepest gratitude to my colleagues Orçun ERGÜN and Burcu AKSOY for their infinite support, patience and kindness.

Finally, and most importantly, I would like to huge thank to my husband for his full supports and understanding and to my parents supporting me spiritually throughout my life.

This work financially supported by BAP with project no: BAP-07-02-2017-004-270.

TABLE OF CONTENTS

LIST OF TABLES

TABLES

LIST OF FIGURES

FIGURES

LIST OF ABBREVIATIONS

Å	Angstroms
m	Meter
mm	Millimeter
nm	Nanometer
μm	Micrometer
kHz	Kilohertz
Hz	Hertz
MHz	Megahertz
GHz	Gigahertz
au/arb units	Arbitrary units
rpm	Round per minute
	Relative permittivity
	Dielectric constant
$_0$	Relative permittivity of vacuum (8.854×10^{-12} F/m)
tan	Tangent loss
f	Resonant frequency
Q	Reciprocal of dielectric losses
$Q\times f$	Quality factor
	Temperature coefficient of resonant frequency
	Temperature coefficient of dielectric constant/permittivity
mole%	Mole percent
wt%	Weight percent

CHAPTER 1

INTRODUCTION

$MgTiO_3$-based dielectric ceramics, operational at frequencies (wavelengths) ranging from 0.3 GHz (1 m) to 300 GHz (1 mm), are of interest for communication systems and play an important role in design and manufacture of communication and radar equipment. The microwave equipment with reduced size could be possible when $MgTiO_3$-based dielectric ceramics are used [1]. Freer and Azough [2] concluded that three major criteria are taken into consideration for designing and developing these kinds of equipment from ceramics. First, ceramic should have a high dielectric constant (ε_r) in order to get size reduction. Second, quality values (Qxf, f= resonant frequency) of dielectric ceramic should be as high as possible to get a small dielectric loss (tan). Q is reciprocal of tan . Third criterion is related to temperature stability of dielectric materials with changing temperature. The ceramics should have close to zero temperature coefficient of resonant frequency ( ). In general, the dielectric materials with Q value larger than 30,000 at 1 GHz were chosen for microwave dielectric resonators [2].

Magnesium titanate - calcium titanate ($MgTiO_3$-$CaTiO_3$, MCT) ceramics are used as microwave dielectric ceramic for capacitors recompensing the temperature, antennas and dielectric type resonators owing to their high permittivity, quality factor, and good temperature strength [3]. The material is a mixture of $MgTiO_3$ with dielectric constant of 17, $Q \times f$ value of 160,000 (7 GHz), and τ_f value of close to zero [4]. Perovskite crystal structured $CaTiO_3$ has ε_r of 170, $Q \times f$ value of 3600 (7 GHz), and τ_f value of near to 800 ppm/°C [5]. A MCT ceramic is prepared by mixing appropriate amounts of high Q and low τ_f of $MgTiO_3$ and low Q and high τ_f of $CaTiO_3$ to get complementary dielectric properties. The reason for the combination of two or more different ceramics

with different stoichiometry is that getting optimum dielectric properties with benefit from opposite dielectric characteristics of ceramic materials.

Huang et al. [6] combined 0.95 mole $MgTiO_3$ and 0.05 mole $CaTiO_3$ ceramics in order to obtain zero τ_f value. Fang et al. [7] studied different calcination temperatures to see the effects of different particle size on dielectric properties. The optimum calcination temperature was chosen 700 °C with 50-100 nm particle size. MCT ceramics with Mg:Ca molar ratio of 95:5, referred to as $M_{0.95}CT$ ceramics, prepared by the sol-gel method and subsequently fired at 1175 °C provided dielectric properties of ε_r= 21.33 and $Q \times f$ = 36,315 GHz [7]. The sol-gel method is a chemical process. $M_{0.95}CT$ ceramics could be successfully prepared at lower temperatures by this method [7]. However, since fabrication of ceramics by the chemical routes is rather costly and time consuming, they are not preferred for mass production of MCT ceramics. Conventional mixed-oxide route is more suitable for MCT ceramics because of easiness in large scale production and low cost of processing.

In order to get desirable dielectric properties, $M_{0.95}CT$ ceramics should be fabricated at high sintered density. A high density sintered $M_{0.95}CT$ ceramic is prepared at temperatures around 1400 °C [8]. However, such high sintering temperatures results in grain growth hence cause the reduction in dielectric properties. Several approach have been proposed to decrease the sintering temperatures. Utilization of different kinds of sintering additives and changing the fabrication route were among the mostly practiced strategies. The liquid phase sintering by adding low melting point material effectively lower the firing temperature of ceramics. So far, liquid phase sintering additives such as B_2O_3 [9, 10], ZnO [11, 12], CuO [6], CoO [13], Bi_2O_3 [14], CaF_2 [15], and $LaAlO_3$ [16] have been tried to decrease the sintering temperature and to improve dielectric properties of $M_{0.95}CT$ ceramics. The dielectric properties of $M_{0.95}CT$ ceramics are also influenced by the liquid phase sintering temperature due to the development of microstructure at low sintering temperature or the reaction between host material and sintering aid.

Although B_2O_3 and ZnO have been successfully added individually to $M_{0.95}CT$ ceramics, addition of a zinc borate compound as sintering aid has not been the subject of any scientific study till now. A zinc borate compound ($Zn_3B_2O_6$) may act as a better sintering aid than either B_2O_3 or ZnO hence, increases densification at lower sintering temperatures and improves dielectric properties of $M_{0.95}CT$ ceramics.

The purpose of this study was to prepare $M_{0.95}CT$ ceramics with controlled microstructure and better dielectric properties at temperatures lower than 1400 °C by the conventional mixed-oxide route. The effects of small amount of $Zn_3B_2O_6$ additions on the microstructural development and dielectric properties of $M_{0.95}CT$ ceramics were also researched. Additionally, the dielectric properties of sintered $M_{0.95}CT$ ceramics were correlated with the microstructures developed.

CHAPTER 2

LITERATURE REVIEW

2.1. Magnesium Titanate-Calcium Titanate Ceramics

The importance of dielectric materials gradually increases with advancing microwave communication technology. Microwave dielectric materials are widely used in applications such as GPS systems, satellite communication systems, and military radars. These microwave devices operate in a wide range of frequencies between 0.3 GHz and 300 GHz that correspond to wavelength range from 1 m to 1 mm, respectively [1].

Ceramics are the most preferred material group in microwave dielectric applications because of their superior dielectric properties. Especially, usage of dielectric oxide ceramics in microwave devices creates a huge revolution to minimize device sizes and costs for these materials as filter, oscillator, and antenna components [17].

Magnesium titanate-calcium titanate ($MgTiO_3$-$CaTiO_3$, hereafter referred to as MCT) is used as microwave dielectric ceramic due to its high permittivity, quality factor and good temperature stability properties. MCT ceramics are used for temperature compensating type capacitor, dielectric resonator and antennas because of their superior properties.

When MgO-CaO-TiO_2 are mixed together, $MgTiO_3$, $CaTiO_3$ and $MgTi_2O_5$ phases that co-existed within a discrete area are obtained as seen in Figure 2.1.

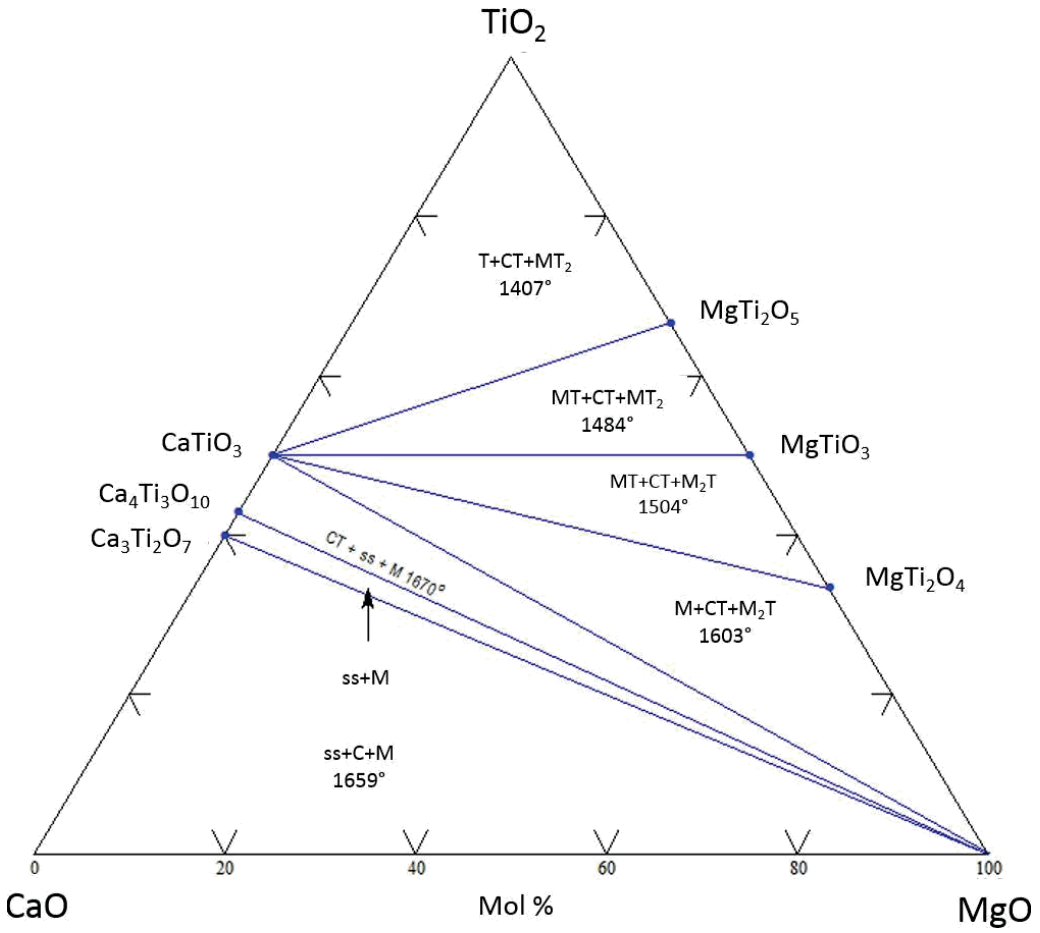

Figure 2.1. Ternary phase diagram of MgO-CaO-TiO_2 (ACERS 04-05380).

The stable phases of $MgTiO_3$ and $CaTiO_3$ disperse to different phases at 1460 °C. Therefore, it is not possible to operate above 1460 °C for both calcination and sintering processes during fabrication of MCT ceramics. In order to determine the exact stoichiometry for the $MgTiO_3$-$CaTiO_3$ mixtures, Figures 2.1 and 2.2 are taken into consideration for the fabrication of MCT ceramics. Usually, $0.95MgTiO_3$-$0.05CaTiO_3$ stoichiometry is chosen as starting point for conventional solid-state method from high-purity oxide powders since it offers better dielectric properties. Requirement of high sintering temperatures in conventional solid-state method is a disadvantage for production. But, other chemical methods inhibit fabrication of these kinds of ceramics

for large scale mass production. In order to decrease sintering temperature, different kind of additions or sintering aids can be added into MCT ceramics.

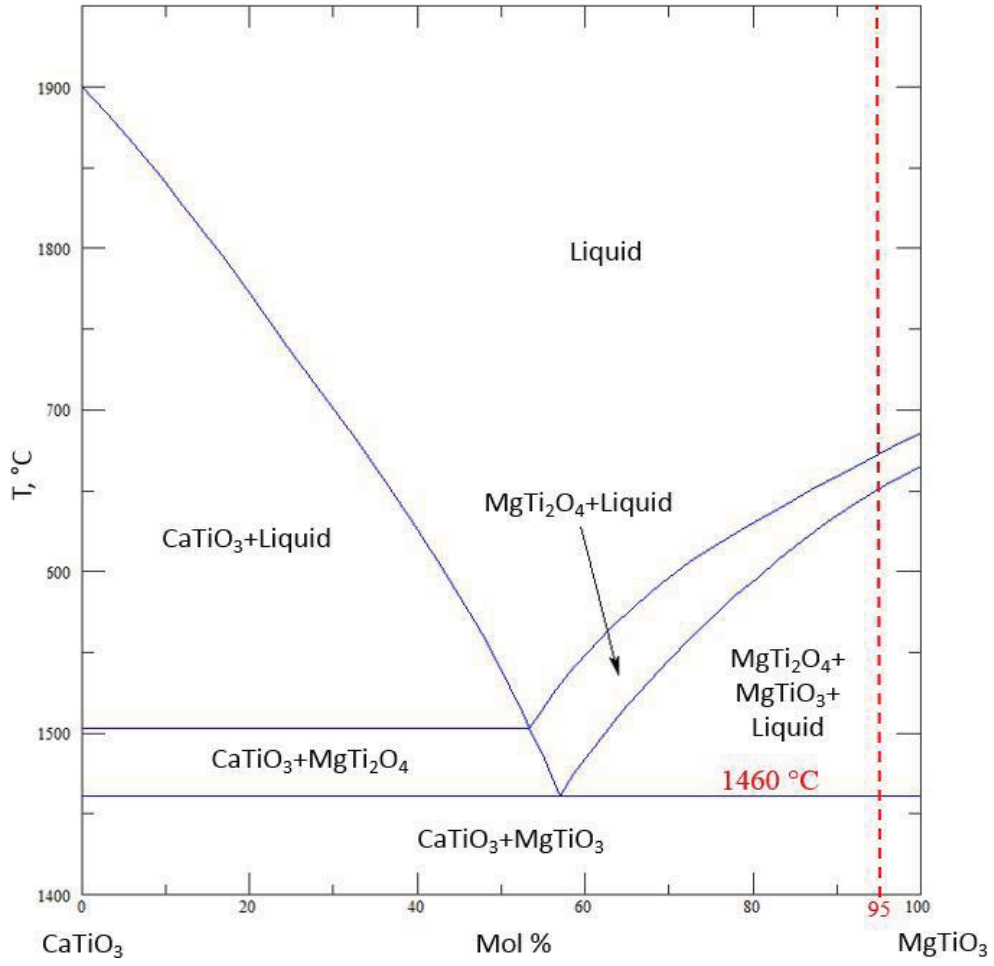

Figure 2.2. The binary phase diagram of $MgTiO_3$-$CaTiO_3$ compounds (ACERS 03-04553-C).

2.2. Dielectric Properties

Dielectric materials do not allow to move any charged particles freely. Thus, these kind of materials can be accepted as insulators [18]. The band theory helps to understand working principle of dielectric material and it's difference from other materials. Basically, the band theory describes the electron actions in a solid material.

The electrical properties of conductors, semiconductors and insulators can be understood in terms of energy bands and gaps. According to this theory, there are three important energy bands in solids which are valance band (VB), conduction band (CB). and forbidden band (FB). Band means a collection of energy levels. In metals which are conductors, the VB and CB overlap. In semiconductors, there is a small gap between VB and CB as shown in Figure 2.3. However, in insulator materials like dielectric ceramics, there is a huge gap between the VB and CB [19].

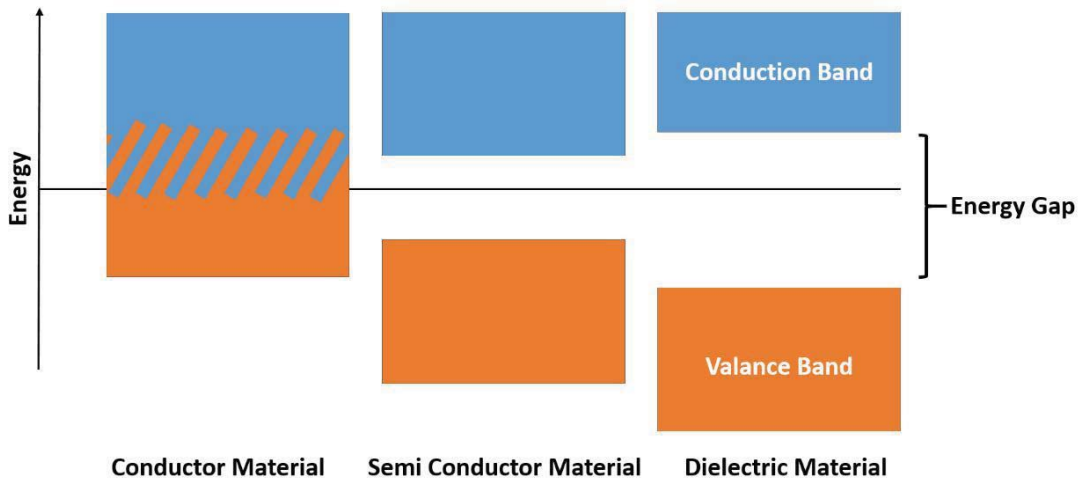

Figure 2.3. Band structure for materials.

Each energy band is separated from the other by an energy gap. The VB has fully or half-filled valance electrons. Valance electrons are located at the outer shell of the atom. The CB is empty. If the electrons have enough energy, they can jump up from the VB to CB. In order for an electron transfer from VB to CB, the energy gap must be overcome by electrons [19, 20].

In dielectric materials, there is a large gap between VB and CB. Thus, they do not keep any electron in CB. As a consequence of this, dielectric materials do not conduct the electricity. The only reason of conductivity is charged ion transfer [20, 21]. Dielectric materials do not conduct electrical energy; but, they are affected by applied electrical field. Under an electrical field, electron density reorganizes. Hence, the

dielectric material responds with a shift of electrical charge centers. Then polarization occurs [22].

As shown in Figure 2.4, the electrical dipoles provide electrical charge concentration on dielectric material surface.

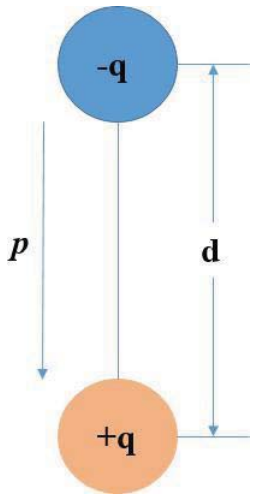

Figure 2.4. Electric dipole.

The polarization magnitude of a material (*P)* is described the total electric dipole moment ($\sum p$) in unit volume (V).

$$= \sum —$$

The polarization magnitude of a material (*P)* is described the total electric dipole moment ($\sum p$) in unit volume (V).

$$= \sum —$$

As mentioned above, under an applied external electrical field, the charged particles are aligned. As a result of this, electrically charged particles are polarized [20].

Polarization occurs with three different types; electronic polarization, ionic polarization and orientation polarization [20, 22].

In Figure 2.5, the correlation between dielectric constant and frequency is given. Different physical mechanisms dominate the dielectric characteristics of a material. These primary mechanisms are ion conduction, polarizations of atoms and electrons, dipolar relaxation phenomena. The dielectric loss factor (″) controls the conductivity of ions at low operating frequencies. Dipolar and related relaxation mechanisms lead to observe alternative dielectric constant values at microwave frequencies. As a result of polarizations of electrons and atoms in material, the peaks are absorbed in infrared frequency range [23].

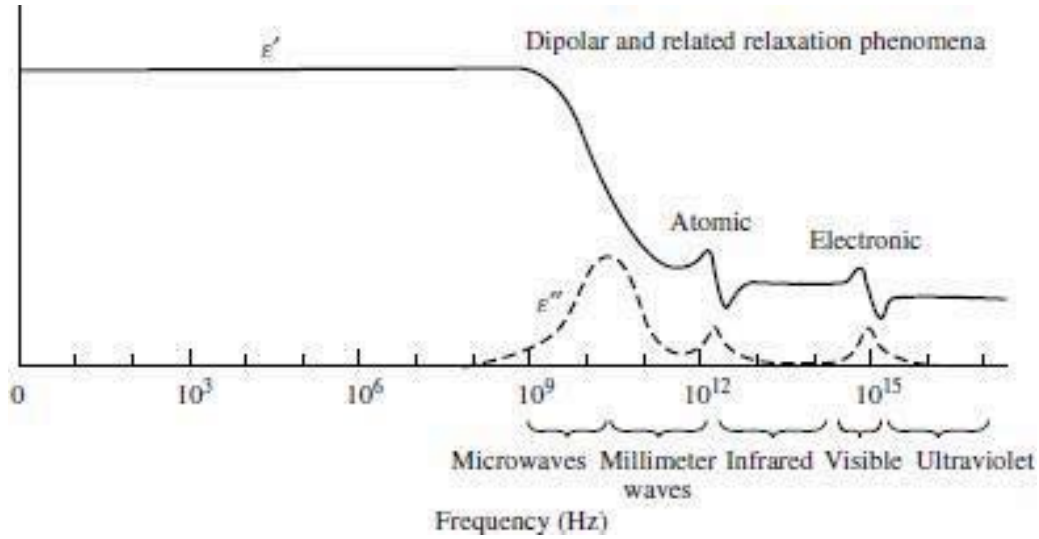

Figure 2.5. The relation of dielectric constant and frequency [23].

2.3. Dielectric Constant

Dielectric constant (ε) can be defined as a degree of charge storage capability of a material [19]. The dielectric constant is the multiplication of relative dielectric constant (relative permittivity) ( ) and permittivity of vacuum (0):

$$= \cdot 0$$

The permittivity of vacuum (0) has a constant value that is 8.854×10^{-12} Fm^{-1}.

The basic method for comprehending the meaning of ε is understanding capacitor structure. In a capacitor, there are two parallel conductive plates that are isolated from each other by an insulator dielectric material. The conductor parallel plates are separated with a '*l*' distance. The plates have 'A' surface area. When an external '*V*' voltage is induced to the system, both plates charged with a quantity of electricity *Q*. Capacity (*C*) is obtained with the ratio of *Q* and *V*. The unit of the capacitance is coloumb/volt or farad.

$$=$$
$$—$$

In the first case, the space between conductor parallel plates is filled with vacuum. Under the vacuum situation, capacitance can be calculated from the following equation:

$$=$$
$$_0 —$$

When the space is filled by an insulating material which called dielectric and a voltage is induced to these plates, the capacitance equation is:

$$=$$
$$—$$

where represents the permittivity of insulating medium. The relative permittivity ( ) can be computed by the permittivity of insulating medium to the permittivity of vacuum ($_0$) ratio:

$$= \quad —_0$$

The relative permittivity is generally called as dielectric constant.

Dielectric materials are investigated in both macroscopic and microscopic scales. In macroscopic scale, relation between electrical field strength (V/m) and the dielectric

displacement (C/m^2) for dielectric materials is mentioned. If dielectric properties are handled from an engineering approach, macroscopic scale is utilized [24].

If alternative current (AC) is applied to capacitors, electrical properties of material are taken into consideration. Electrical properties of a material are comprised of polarization, capacitance, dielectric losses and conductivity. The dielectric constant can be expressed in a complex form which involves real and imaginary parts. These complex expressions contain the electrical properties of the material [24].

$$= ' - \quad ''$$

$'$ is absolute dielectric constant and $''$ is the dielectric loss factor. is defined as the complex relative permittivity [25, 26].

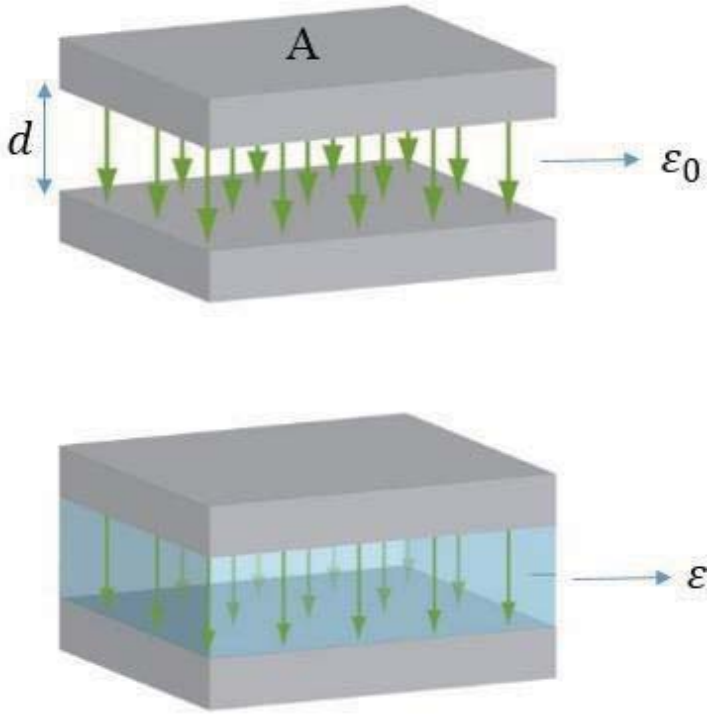

Figure 2.6. Capacitor structure [20].

2.4. Dielectric Loss Factor

Electrical conduction, dielectric relaxation and resonance effects of a material cause dielectric losses in material. In other words, dielectric loss factor signifies the degree of electromagnetic energy conversion to heat energy at a definite frequency [27-29].

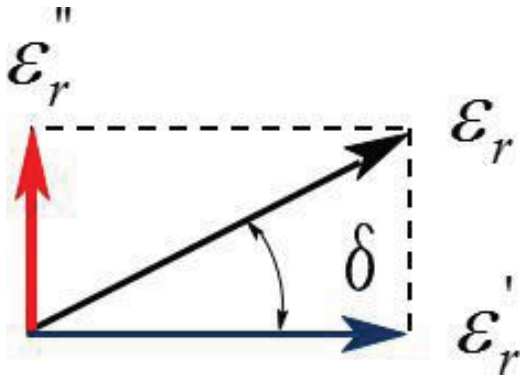

Figure 2.7. Vectorial expression of loss factor [29].

Internal and external dielectric losses compose the total dielectric loss of a dielectric material. The crystal structure such as crystal symmetry, temperature and AC field frequency is related between intrinsic dielectric losses of the material. The extrinsic losses can be minimized with appropriate dielectric material. Hence, the origin of the extrinsic losses is linked with defects in a crystal lattice. These crystal defects stem from porosity, micro cracks, grain boundary imperfections, dislocations etc. [30].

The dielectric loss or loss tangent (tan) is computed from the ratio between imaginary dielectric constant (loss factor, $''$) and real part of dielectric constant ($'$). As it is defined before, $''$ is connected the amount of energy loss of a material; besides, $'$ is a symbol of the amount of stored energy in material [25, 26]. Tangent loss is a dimensionless parameter.

$$\tan = \frac{''}{'}$$

According to loss tangent formula, for dielectric materials these expressions can be said; $'' \geq 0$ and $' \geq ''$ [24].

These dielectric losses can initiate thermal stresses in material for high frequencies or high voltage. It is desired that, once selecting a dielectric material, loss tangent factor of the material is as small as possible [30].

Dielectric materials can be categorized into four main groups according to their dielectric constant and tangent loss values.

Low Dielectric Constant, Low Loss Dielectric Material (≥ 4, tan < 0.001)

High Dielectric Constant, Low Loss Dielectric Material (≥ 10, tan < 0.001)

Very High Dielectric Constant, Ultra-Low Loss Dielectric Material (′ ≥ 100, tan < 0.0002)

Lossy Dielectric Material (tan > 0.1) [31]

The dielectric loss factor of a material can be expressed the quality factor of the material with the following equation:

$$= \frac{1}{\tan}$$

is directly related with the frequency of microwave dielectric materials. Thus, it is used with frequency symbol as $\times f$.

The $\times f$ value of dielectric materials is calculated from width of the resonant peak at 3dB as shown in Figure 2.9.

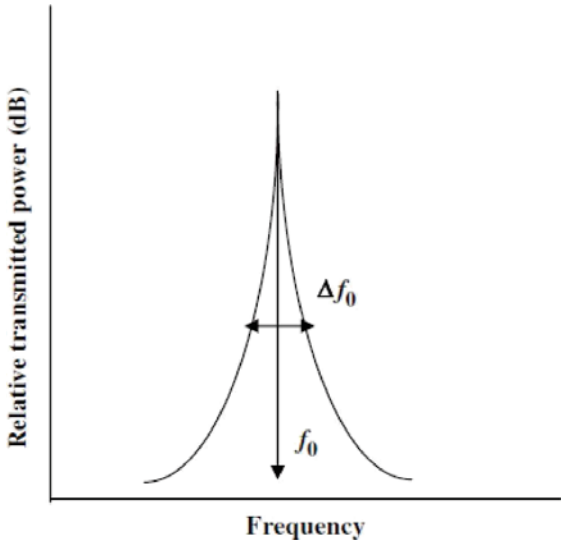

Figure 2.9. Illustration of the width of resonance peak at 3dB frequency [32].

$$= \frac{_0 \Delta}{_0}$$

$$= \frac{0}{} \times \Delta_0$$

Heat loss, dielectric loss, conduction loss and radiation losses causes the total material loss. Radiation loss is not taken into consideration when cavity method is used for dielectric measurements because of the shielding supported by cavity. In this case total loss is shown by equation given below:

$$\frac{1}{_0} = \frac{1}{} + \frac{1}{} + \frac{1}{}$$

Where$_0$= total losses,=dielectric losses,=conduction losses and =radiation losses [33].

2.5. Temperature Coefficient of Resonant Frequency

In order to determine temperature stability of the dielectric material, temperature coefficient of resonant frequency parameter must be checked. As temperature increasing or decreasing, the shift degree of the resonant frequency demonstrates

temperature coefficient of resonant frequency ( ). The more near-zero value is obtained, the more efficient dielectric material is designed for electronic devices in microwave industry.

The equation of temperature coefficient of resonant frequency is given below.

$$= - \quad - \frac{}{2}$$

: Temperature coefficient of the permittivity

: Linear thermal expansion coefficient (generally this value has a positive value for dielectric materials)

The unit of temperature coefficient of resonant frequency ( ) is 'ppm/°C'. Temperature stability is an important factor for dielectric materials because of their critical and technological usage areas. value must be as possible as close to zero. In order to achieve this, linear thermal expansion coefficient ( ) value of the dielectric must have one-half and positive value. Most advanced ceramic materials that are used in electronic technology approximately have +10ppm/°C linear thermal expansion coefficient value [30].

To determine the temperature coefficient of the permittivity ( ), following formula is used:

$$= \frac{_2 - \quad _1}{_1(\ _2 - \ _1)}$$

where $_1$, $_2$ represent the resonant frequencies at $_1$ and $_2$ temperature points, respectively [34].

2.6. Dielectric Characterization

Dielectric characterization (impedance analyzer spectroscopy) is a measurement technique which is used for determination of dielectric properties of a medium as a

function of frequency [31]. The dielectric characterization equipment operates in a wide range of frequencies between 100 Hz and 40 MHz.

In this study, parallel plate (electrode) technique is used basically. In order to obtain a capacitor structure, a simple dielectric material sandwich is composed. This sandwich structure contains a dielectric material between two parallel electrodes. It gives a capacitor structure. An impedance analyzer and a fixture [35] are used for analysis. It is possible to measure dielectric properties at low frequencies (< 1 GHz) with parallel plate (electrode) route. According to dimensions of the dielectric specimen and computing the dielectric specimen's capacitance value, parallel plate test parameters are achieved. While measuring dielectric constant, a dielectric specimen is located in a sample holder and capacitance value is considered to obtain permittivity. This technique has a high precision for calculation of dielectric parameters (approximately ±1% for and ± 0.005 for tan). The measurement frequency can vary between 1 kHz and 40 MHz. In order to prevent the errors in calculations, air gap effects must be considered and calibration must be done before analysis [36].

In some cases electrode polarization effect can give incorrect dielectric results. It is possible to decrease this effect with using large electrode surfaces or measuring at high frequencies. As measurement frequency increases, better and correct results can be taken [37].

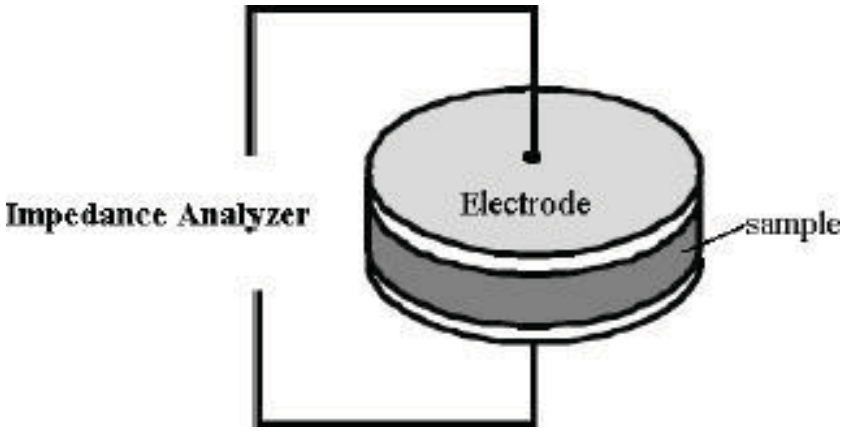

Figure 2.8. Parallel plate technique [36].

2.7. Conventional Mixed-Oxide Method

There are three main steps in conventional mixed-oxide method [38, 39]: (1) powder preparation, (2) green body forming, and (3) sintering. In the first stage, high purity oxides (commercial powders) are weighed with desired stoichiometric ratio and mixed with a binder or an additive. Milling can be applied in order to increase the reaction rate of powders. Then mixed powders are calcined at high temperatures to initiate the chemical reaction between oxide powders. At the second stage, fired powders can be pressed, casted, or extruded to shape ceramic powders. The products of the calcined and shaped ceramics are called 'green body'. The final stage of traditional ceramic fabrication is sintering. At this step, the green body is heated to elevated temperatures to get a dense microstructure. The powders are diffused and bonded each other to decrease the total system energy, increase the density, and strength. Sintering can be performed with or without the presence of a liquid phase. In case of the presence of liquid phase, it is called 'liquid-phase sintering'; in the contrary case, it is called as 'solid-state sintering' [38, 39].

CHAPTER 3

EXPERIMENTAL PROCEDURE

3.1. General

$M_{0.95}CT$ ($95MgTiO_3$-$5CaTiO_3$ mole %) dielectric ceramics were prepared by mixing high purity oxide powders, shaping, and sintering at various temperatures. The microstructure of the disk shaped ceramic samples was characterized. In order to investigate densification of $M_{0.95}CT$ ceramics, Archimedes' technique was used. The dielectric properties were measured with poled and electroded specimens.

The flowchart of the steps applied for the production of $M_{0.95}CT$ ceramics is shown in Figure 3.1.

3.1.1. Sample Preparation

Powders of $M_{0.95}CT$ ceramics were prepared by conventional solid-state method using high-purity MgO, TiO_2, and $CaCO_3$ powders. The powders used in the preparation of $M_{0.95}CT$ ceramics were listed in Table 3.1.

Table 3.1. *List of powders used in the preparation of $M_{0.95}CT$ ceramics.*

Powder Name	Chemical Formula	Supplier	Purity (wt %)
Magnesium Oxide	MgO	Alfa-Aesar	99.9
Calcium Carbonate	$CaCO_3$	Strem Chemicals	99.95
Titanium Dioxide	TiO_2	Merck	99.9

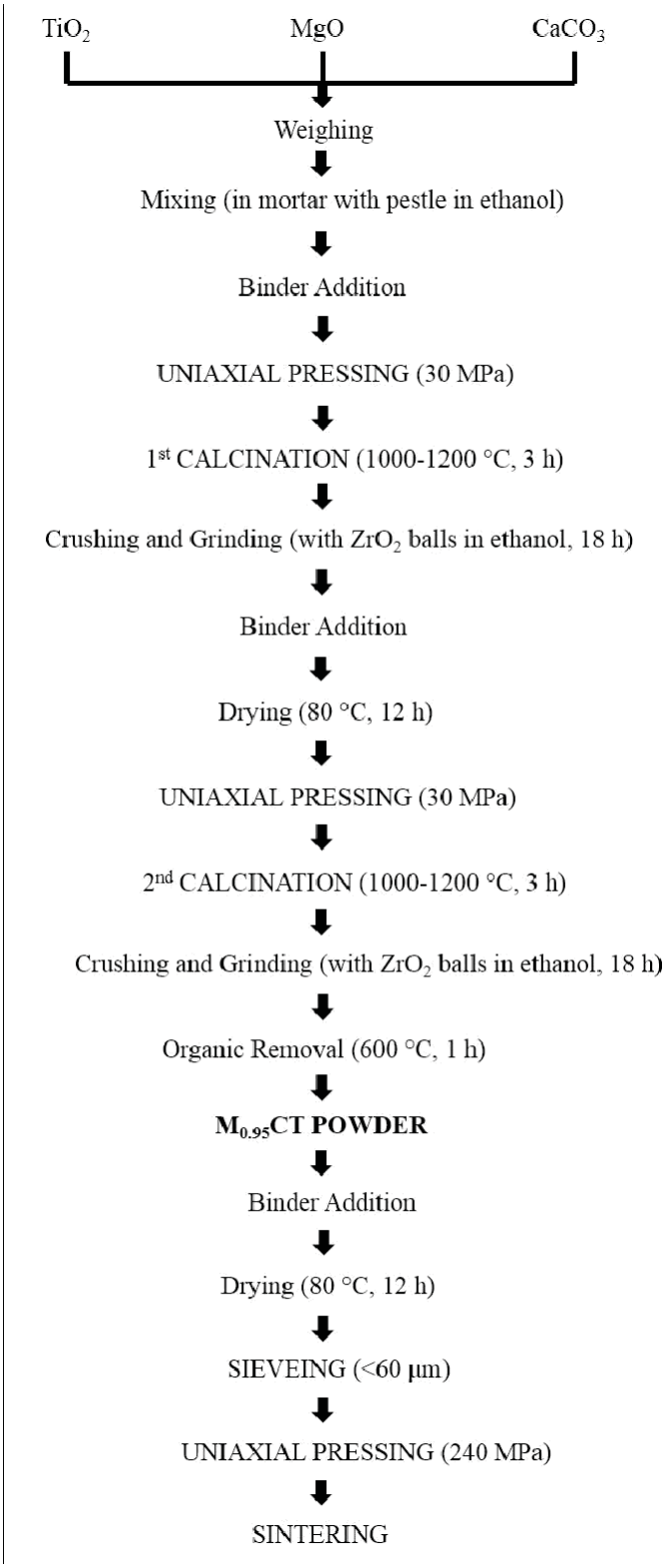

Figure 3.1. The flowchart showing the steps applied for the production of $M_{0.95}CT$ ceramics.

In order to get the mole ratio of Mg:Ca=95:5, necessary amounts of powders were weighed and mixed with ethanol manually. The mixed powders were dried in an oven at 80 °C for 12 h. The powders dried were mixed with 0.5 weight percent (wt%) polyvinyl alcohol (PVA) that was added as binder. In order to get a homogeneous mixture, ethanol was also added with PVA using an agate mortar with pestle until the mixture is completely dried. Dried mixtures were compacted to disc shaped pellets of nominal dimensions of 30 mm in diameter and 8 mm in height in a hardened steel die. After that, the pellets were calcined at temperatures of 1000, 1050, 1100, and 1200 °C for 3 h. The heating and cooling rates applied during calcination were 4 °C/min. The schedule showing the applied temperature, time and heating rate for the second calcination process was illustrated in Figure 3.2.

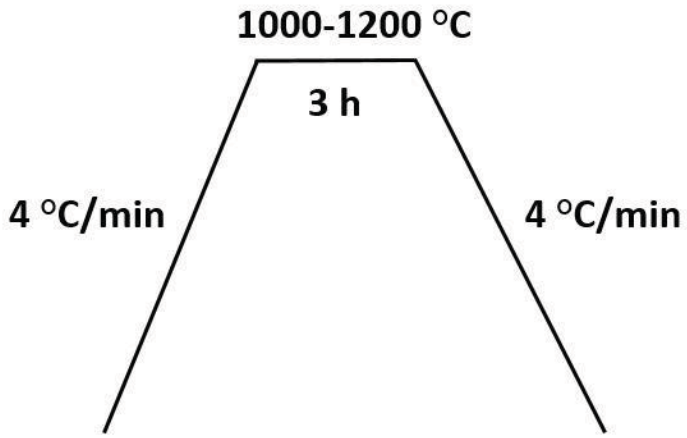

Figure 3.2. The schedule of the first and second of calcination processes.

The calcination product was crushed using an agate mortar with pestle in dry medium. The crushed powders were ground in a plastic jar for 18 h by a ball mill. The ball milling took place in a medium of ethanol using zirconia balls.

In order to eliminate undesired intermediate phases developed during the first calcination, a second calcination was applied at temperatures of 1000, 1050, 1100, and 1200 °C for 4 h. The heating and cooling rates applied during calcination were 4 °C/min.

After the second calcination, calcined powders were crushed and ground in the same manner as explained for the first calcination to obtain $M_{0.95}CT$ powders. The calcined $M_{0.95}CT$ powders were mixed with 0.5 wt% PVA and ethanol and dried in an oven at 80 °C for 12 h. The dried powders were sieved from a screen of 250 mesh (60 μm) to get fine and uniform powder. After that, the $M_{0.95}CT$ powders were compressed into pellets with 13 mm in diameter and 5 mm in thickness in a hardened steel die using a hydraulic uniaxial press at a pressure of 240 MPa. The $Zn_3B_2O_6$ (ZBO) added $M_{0.95}CT$ powders were mixed with 0.5 wt% PVA and ethanol and dried in an oven at 80 °C for 12 h. The dried powders were sieved from a screen of 250 mesh (60 μm) to get fine and uniform powder. After that, the $Zn_3B_2O_6$ added $M_{0.95}CT$ powders were compressed into pellets with 13 mm in diameter and 5 mm in thickness in a hardened steel die using a hydraulic uniaxial press at a pressure of 240 MPa.

In order to prepare $Zn_3B_2O_6$ compound, a solution was prepared using boric acid (H_3BO_3, Eti Maden 99.9 wt% purity) and zinc oxide (ZnO, Alfa Aesar, 99.9 wt% purity). ZnO was mixed with nitric acid (HNO_3). 25 cc HNO_3 and 75 cc distilled water were slowly added into 10 g ZnO. In order to get $3ZnO \cdot B_2O_3$ ($Zn_3B_2O_6$), 5.073 g of H_3BO_3 was added slowly into acquired solution. The solution was stirred and kept overnight at laboratory conditions to complete the reaction.

The additive-free (pure) and $Zn_3B_2O_6$ added $M_{0.95}CT$ ceramic pellets were placed in an electrically heated furnace and sintered to get samples. Sintering took place in two steps as shown in Figure 3.3. First, green bodies were heated up to 600 °C with 4 °C/min heating rate and kept for 30 min at 600 °C in order to remove organic residuals coming from ball milling stage and binder. Then, the temperature was raised to different sintering temperatures for different times (1200 °C for 4 h, 1225 °C for 2 and 4 h, 1250 °C for 2, 4, and 6 h, and 1300 °C for 2, 4, and 6 h) at 3 °C/min heating rate. At the final stage of sintering, specimens were cooled down to room temperature at 3 °C/min cooling rate.

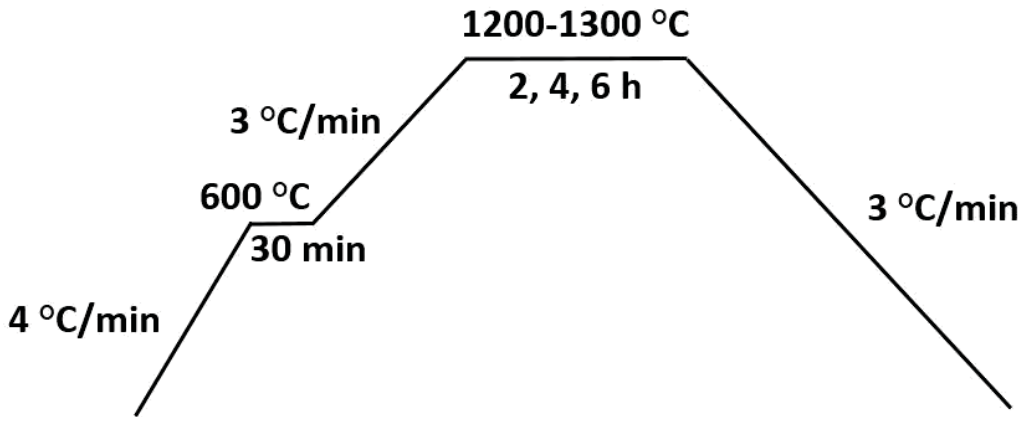

Figure 3.3. Heating schedule applied for the sintering of $M_{0.95}CT$ ceramics.

3.2. Characterization

3.2.1. X-Ray Diffraction (XRD) Analysis

The crystal structure and phase analysis of the pure and $Zn_3B_2O_6$ added $M_{0.95}CT$ powders and sintered bodies were identified by X-Ray diffraction (XRD) analyzer (Bruker) using Cu Kα radiation (λ=1.5418 Å) at operating voltage of 40 kV between 2θ=20 and 60° scan range at a scanning rate of 0.1 °/min. XRD patterns were analyzed using Rigaku 4·2 software. High temperature XRD analysis of samples were performed between 2θ of 20 and 60° at a scanning rate of 4°/min from room temperature up to 1250 °C in a furnace attached to the same diffractometer. The scans were analyzed using the same software.

3.2.2. Scanning Electron Microscopy (SEM) Examination

The microstructure of the starting powders, calcined powders, and sintered bodies were examined using scanning electron microscopy (SEM, Phenom XL). The operation voltage was 15 kV. All samples were coated with a thin layer of gold or carbon by a sputter coating prior to SEM examination.

3.2.3. Energy Dispersive Spectroscopy (EDS) Analysis

The chemical compositions of $M_{0.95}CT$ samples were determined by Energy Dispersive Spectroscopy (EDS) attached to SEM. The elemental analysis were examined at 10 kV voltage.

3.2.4. X-Ray Fluorescence (XRF) Analysis

The elemental and chemical composition of $M_{0.95}CT$ specimens were investigated using X-Ray Fluorescence analyzer (Rigaku ZSX Primus II) equipped with a rhodium x-ray tube, 4 kW generator and ten-position crystal changer.

3.2.5. Particle Size Analysis

The particle size analysis of the starting and calcined powders was analyzed using a Malvern MastersizerTM 2000 (Malvern Instruments, Worcerstershire, UK) laser particle size analyzer.

3.3. Property Measurements

3.3.1. Density

The density of the pure and $Zn_3B_2O_6$ added $M_{0.95}CT$ ceramics were measured according to Archimedes' method using a Mettler Toledo precision digital balance with ±0.0001 accuracy. At the beginning of the density measurements, the dry weight (W_{dry}) of the specimen was measured. Then the specimen was immersed in distilled water for 1 h to provide the penetration of distilled water into possible open pores. The suspended weight (W_{susp}) of the ceramic samples were measured in liquid. The specimens were taken out from the liquid and weighed again. It gives the saturated weight (W_{sat}) of the specimens. The sintered density (ρ_{bulk}) of ceramic samples was calculated by the formula [40].

$$\rho_{bulk} = \frac{\rho_{liq}}{\_}$$

where; ρ_{liq} is the density of saturated/suspended liquid.

3.3.2. Dielectric Properties

3.3.2.1. Dielectric Constant and Dielectric Loss Factor Measurements

The measurements on dielectric properties were performed on the disc shaped sintered bodies. The flat faces of discs were ground, lapped, polished, and fine polished. Silicon carbide abrasive papers were used to grind the parallel faces down to grade 1200. Hard synthetic clothes were used for lapping, polishing, and fine grinding. The thickness of sintered discs was kept uniform by parallel lapping of the flat faces. Then the parallel faces were electroded with fired-on Au paste (5063D Dupont) for electrical contact. Paste applied surfaces were fired at 600 °C for 10 min in a furnace under air atmosphere at 10°C/min heating and cooling rate.

The dielectric constant of samples was calculated at 1 kHz, 10 kHz, 100 kHz, 1 MHz and 10 MHz frequencies. The capacitance of samples was computed using an Agilent 4194A impedance analyzer that operates between 40 Hz and 40 MHz. The dielectric constant of the ceramic samples was determined by the formula [20]:

$$= \frac{\cdot}{{}_0 \cdot}$$

Where is dielectric constant, C is capacitance (F), d is thickness of sample (m), $_0$ is permittivity of vacuum (8.854×10^{-12} F/m) and A is area of sample (m^2). Parallel surfaces of specimens were coated with Au paste and fired at 850 °C for 30 min at the final step. Then, the capacitance values of specimens were measured.

Dielectric constant and dielectric loss factor measurements were performed using a HP4194A Impedance/Gain Phase Analyzer in the 100 Hz-40 MHz frequencies. In order to hold parallel faces of samples Agilent 16047E text fixture was used.

The dielectric constant and dielectric loss values were calculated simultaneously. Dielectric measurements were done at room temperature. Schematic illustration of the setup used for dielectric property measurements is shown in Figure 3.4.

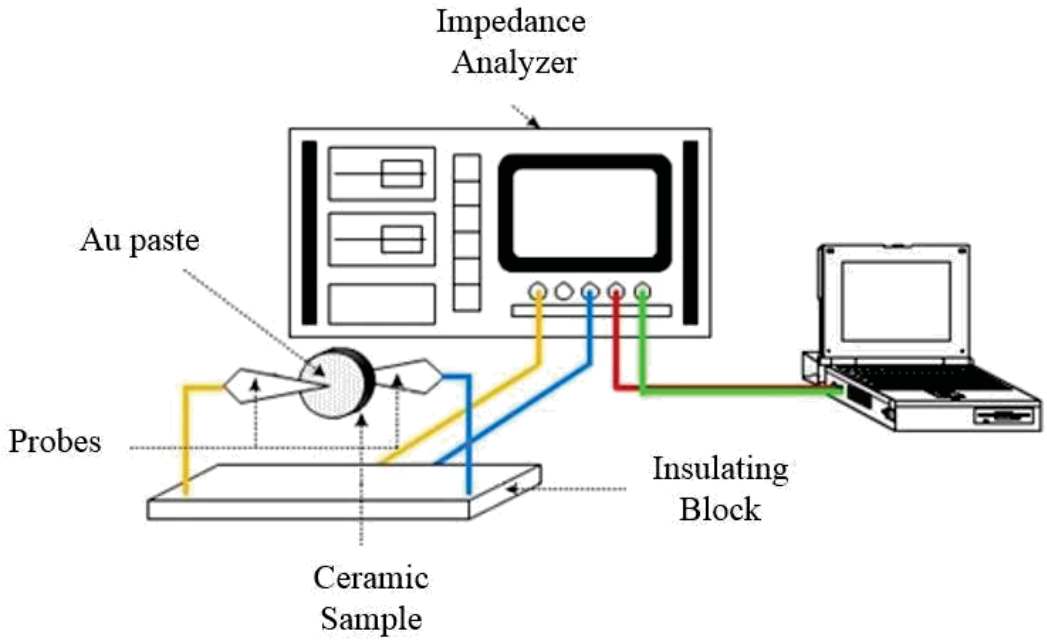

Figure 3.4. Schematic illustration of the setup used for dielectric property measurements [41].

CHAPTER 4

RESULTS AND DISCUSSION

4.1. Production of Magnesium Titanate-Calcium Titanate (MCT) Ceramics

4.1.1. Characterization of Starting Powders

Particle size distribution analysis for MgO powder suggested a unimodal particle size distribution as shown in Figure 4.1. The particle size of MgO powder ranges from d_{10}=0.918 μm to d_{90}=7.185 μm with an average of d_{50}=3.311 μm. The manufacturer of the powder quoted particle size as ~2 μm. The difference may be due to the agglomeration of powder.

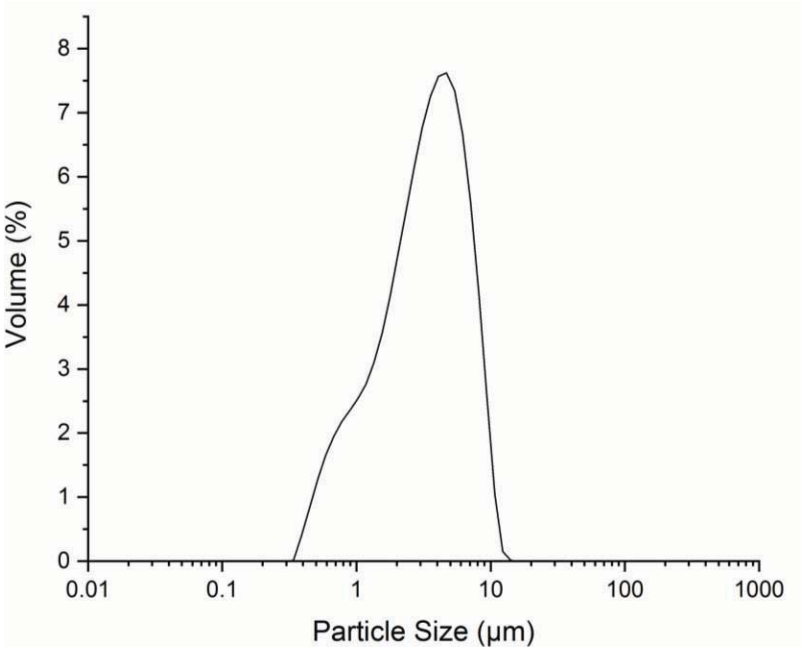

Figure 4.1. Particle size distribution of MgO powder.

The particle size analysis of TiO_2 powder shows bimodal distribution as shown in Figure 4.2. The first mode has 0.17 μm particle size and the second mode has 0.67 μm particle size. The average particle size of the TiO_2 powders is 0.189 μm. The manufacturer of the powder quoted particle size as ~0.25 μm.

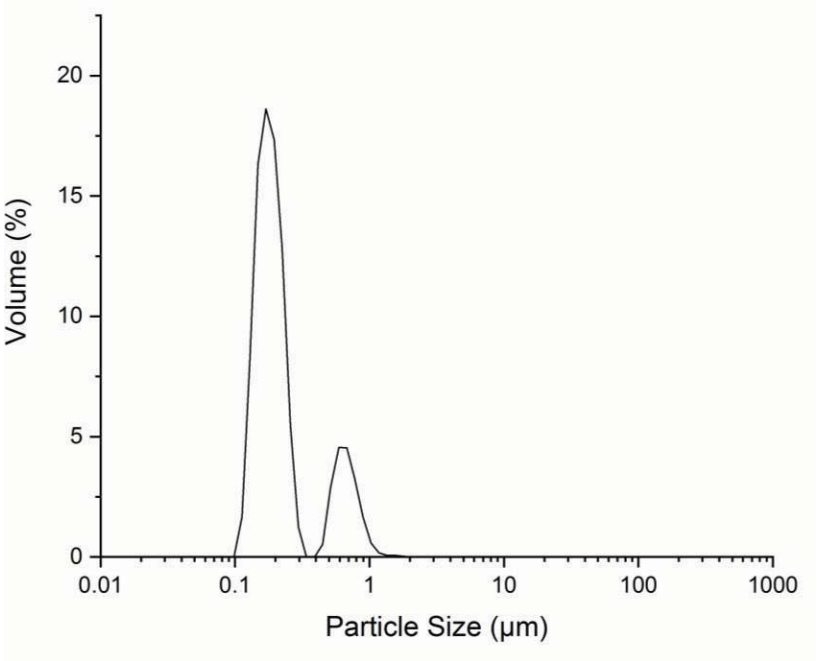

Figure 4.2. Particle size distribution of TiO_2 powders.

In Figure 4.3, particle size analysis of $CaCO_3$ is shown. Particle sizes of $CaCO_3$ powder vary from 0.3 μm to 56 μm. The difference of particle size distribution of $CaCO_3$ powder reveals the agglomeration of the particles. 50% of the particles have 18 μm particle size. 90% of the particles are below 31.2 μm. The manufacturer of the powder quoted particle size as ~50 μm.

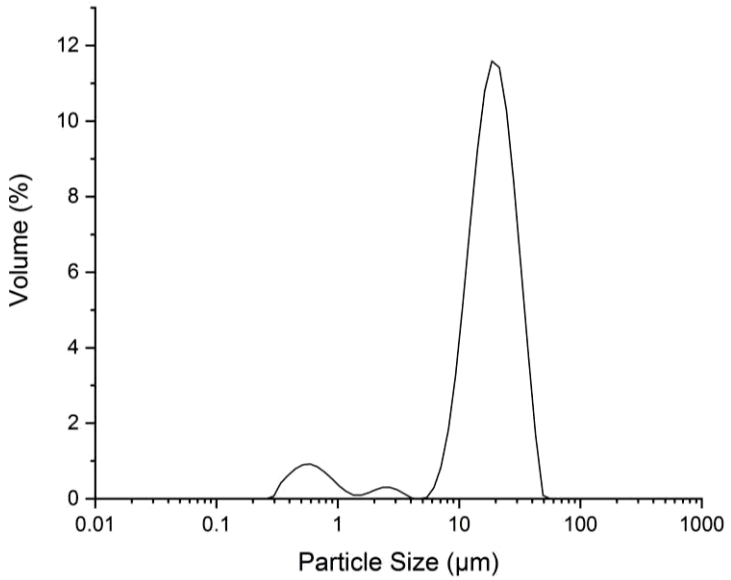

Figure 4.3. Particle size distribution of $CaCO_3$ powder.

X-ray diffraction (XRD) patterns of starting powders were shown in Figures 4.4-4.6. XRD pattern of MgO powder was illustrated in Figure 4.4. All XRD peaks matched with MgO phase (PDF Code: 82-1691).The pattern was indexed with a cubic unit cell with *Fm3m* space group symmetry. Impurity was not detected.

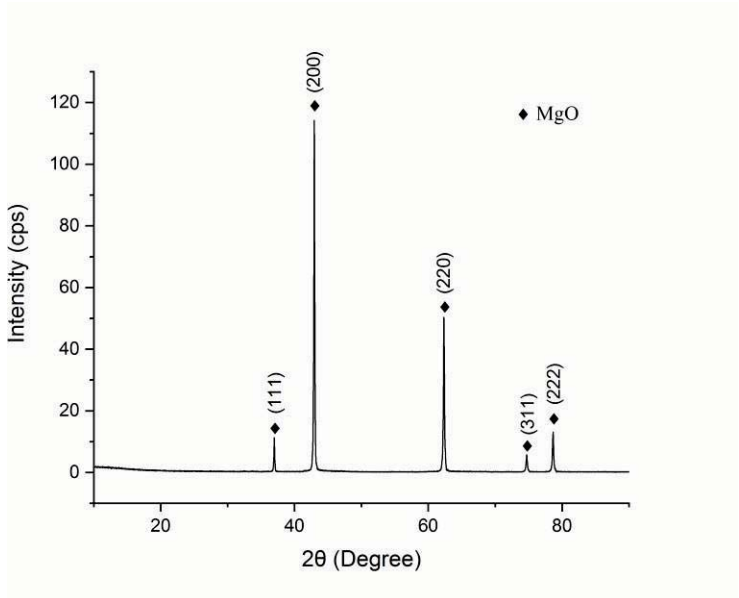

Figure 4.4. XRD pattern of MgO powder.

The XRD pattern of TiO_2 powder was shown in Figure 4.5. XRD analysis suggested that the powder consists of the mixture of rutile (PDF Code: 89-4920) and anatase (PDF Code: 78-2486) phases of TiO_2. Extra peaks belonging to other TiO_2 phase or impurities were not detected.

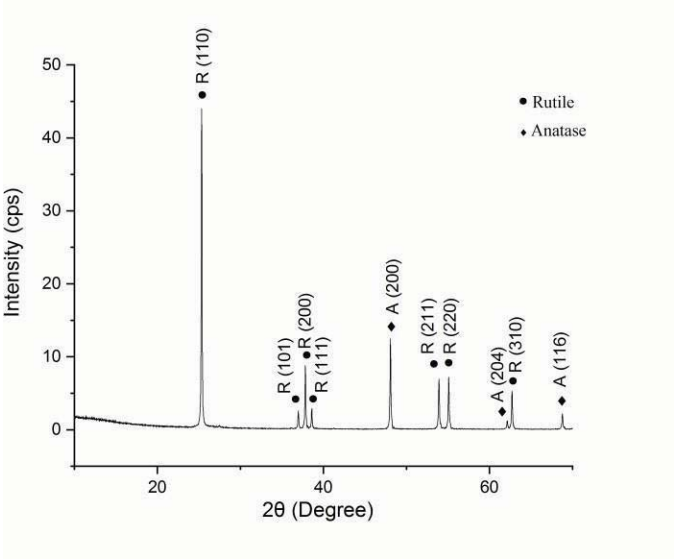

Figure 4.5. XRD pattern of TiO_2 powder.

Figure 4.6 illustrates the XRD pattern of $CaCO_3$ powder. The powder has single phase $CaCO_3$ with R3c space group symmetry with a rhombohedral structure (PDF Code: 47-1743).

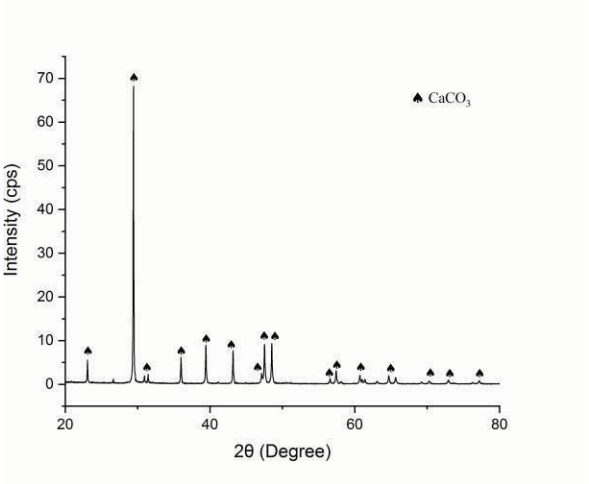

Figure 4.6. XRD pattern of $CaCO_3$ powder.

Scanning Electron Microscopy (SEM) images of the starting powders are shown in Figure 4.7. The SEM image of the MgO powder, shown in Figure 4.7(a), suggests that the particles are in submicron size and agglomerated. Although particle size distribution analysis revealed average particle size of 3.311 μm, SEM examination shows that the particles are smaller than 3 μm. In Figure 4.7(b), SEM image of TiO_2 powder is illustrated. The particle size analysis revealed that particles are approximately 0.189 μm in size. As a result of fine particles, shown in Figure 4.5, particles are severely agglomerated. $CaCO_3$ particles are in cuboid geometry as shown in Figure 4.7(c). According to the SEM image, the particle size of $CaCO_3$ powders ranges from 1 to 10 μm.

It is obvious that there is a conflict between particle size of starting powders as measured by particle size analyzer and by SEM. The difference was attributed to the agglomeration of fine particles. As the starting powders are very fine, agglomeration occurs easily before particle size analysis by the particle size analyzer. Although the starting powders were vibrated in an ultrasonic bath to prevent the agglomeration of fine powders, it was not possible to get complete dispersion of strongly agglomerated powders.

Figure 4.8 shows the Energy Dispersive Spectroscopy (EDS) spectra of the starting powders. C peaks in the spectra were excluded since they come from C coating and C tape. Thus, C amount was not included for the determination of chemical composition. The elemental analysis and their corresponding oxides were listed in Tables 4.1-4.3. The EDS analysis of MgO powder suggested that the powder consists of Mg, Si, and O elements as shown in Table 4.1. Although the manufacturer reported that the powder is in 99.9 % purity, small amount of Si was detected. It is believed that Si is present as SiO_2. In Table 4.2, The EDS analysis data of TiO_2 powder was presented. The powder consists of only Ti and O elements. No impurity was detected. As suggested by XRD analysis TiO_2 powder was pure. Table 4.3 lists the elements present in $CaCO_3$ powder. $CaCO_3$ powder is composed of Ca, C, and O elements giving CaO content of 63.83 wt%. No impurity was detected.

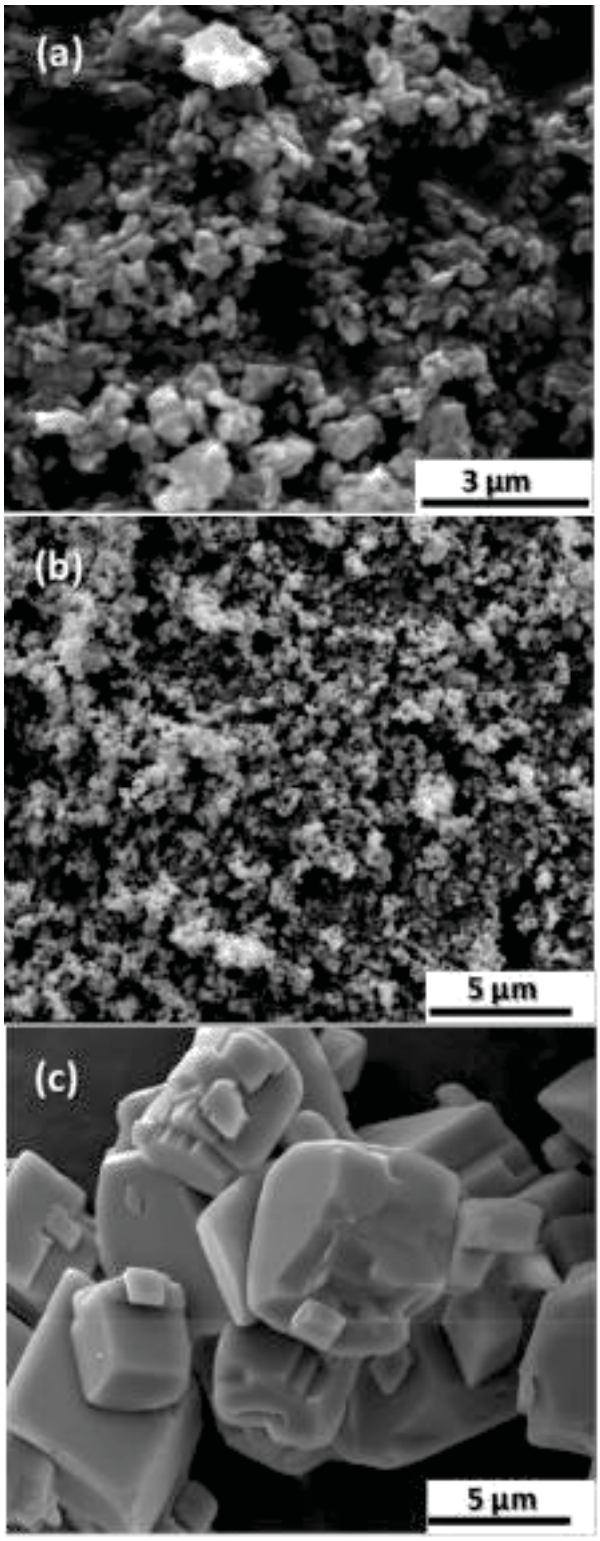

Figure 4.7. SEM micrographs of starting powders (a) MgO, (b) TiO_2 and (c) $CaCO_3$.

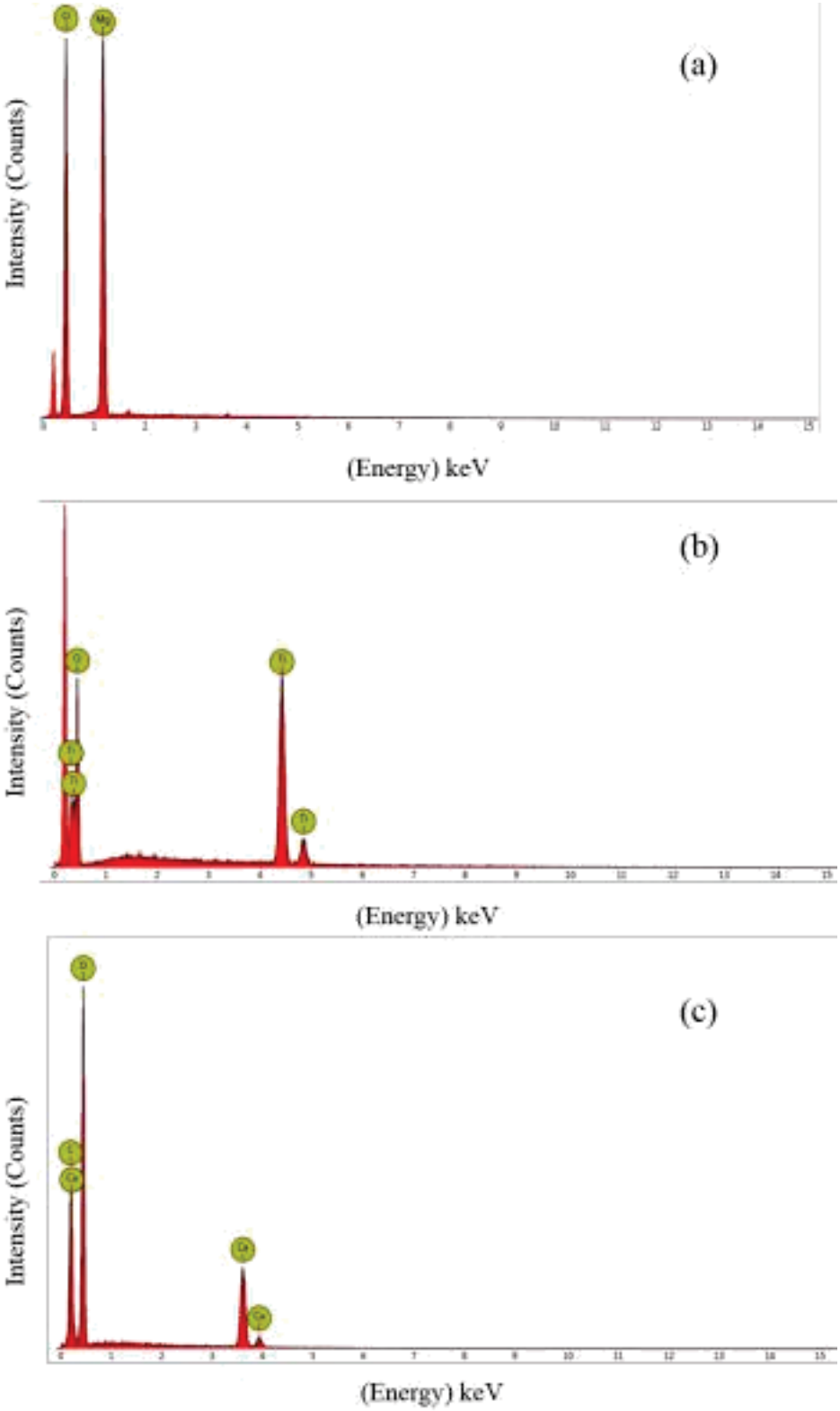

Figure 4.8. EDS spectra of starting powders (a) MgO, (b) TiO_2 and (c) $CaCO_3$.

Table 4.1. *EDS analysis of MgO powder.*

Element Symbol	Atomic Concentration (%)	Weight Concentration (%)	Oxide Symbol	Weight Concentration in oxide form (%)
O	65.93	55.98		
Mg	33.66	43.42	MgO	98.25
Si	0.40	0.60	SiO_2	1.75

Table 4.2. *EDS analysis of TiO_2 powder.*

Element Symbol	Atomic Concentration (%)	Weight Concentration (%)	Oxide Symbol	Weight Concentration in oxide form (%)
O	82.47	61.12		
Ti	17.53	38.88	TiO_2	100.00

Table 4.3. *EDS analysis of $CaCO_3$ powder.*

Element Symbol	Atomic Concentration (%)	Weight Concentration (%)	Oxide Symbol	Weight Concentration in oxide form (%)
O	60.57	55.50		
Ca	10.81	24.82	CaO	63.83
C	28.61	19.68		

4.1.2. Characterization of $M_{0.95}CT$ Ceramic Powder

After the mixing operation using ball mill, powders were calcined and calcined as described in Section 3.1.1 in order to get $M_{0.95}CT$ powder. Figure 4.9 shows the typical particle size distribution graph of calcined and subsequently milled $M_{0.95}CT$ powder. The particle size distribution of the powder was wide and a bimodal distribution with average particle size of 0.9 μm and 2 μm, respectively was noted. Because of calcination, particles are agglomerated.

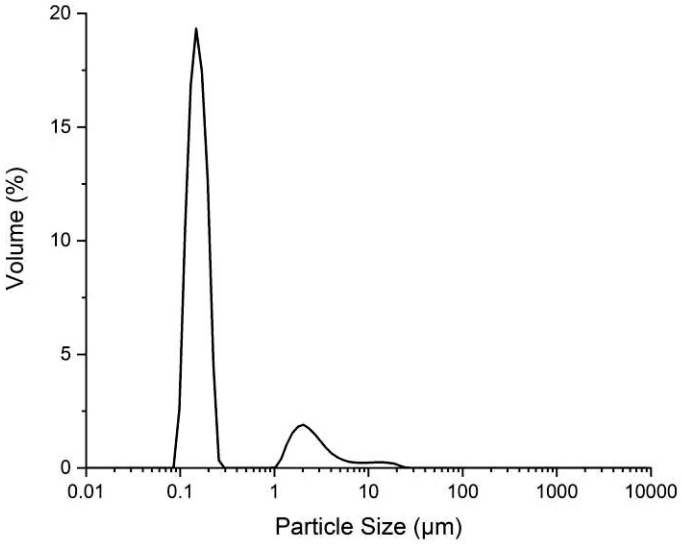

Figure 4.9. Particle size distribution of the $M_{0.95}CT$ powder calcined at 1050 °C and subsequently ball milled.

Particle size-cumulative volume relation of the calcined and subsequently milled $M_{0.95}CT$ powder was illustrated in Figure 4.10. D(10), D(50) and D(90) values were 0.136, 0.189, and 1.744 μm, respectively.

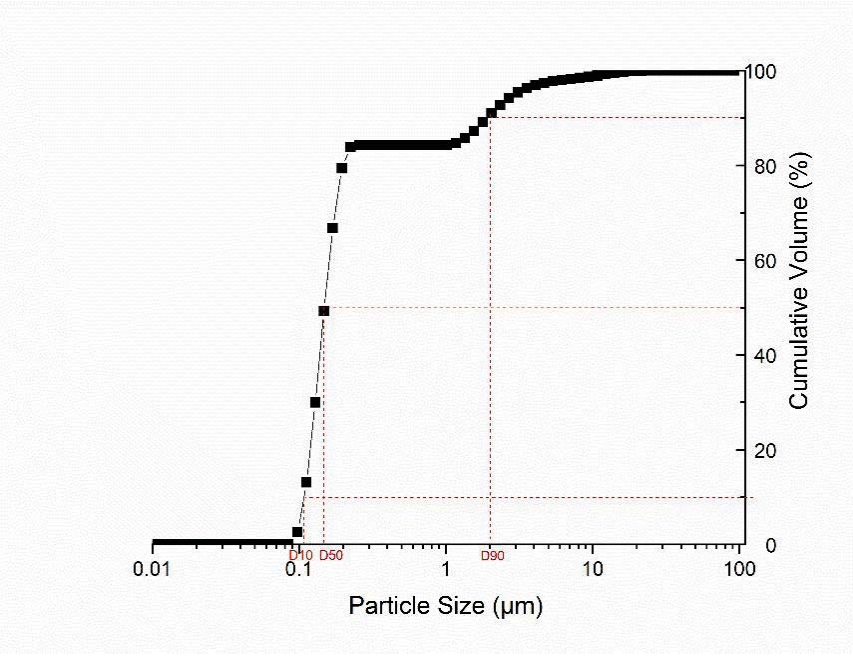

Figure 4.10. Particle size vs. cumulative volume curve for $M_{0.95}CT$ powder.

XRD patterns of the $M_{0.95}CT$ powders calcined at different temperatures and subsequently milled were shown in Figure 4.11. It is clear that the powder contains $MgTiO_3$ (PDF Code: 04-012-1044) as main crystalline phase along with $CaTiO_3$ (PDF Code: 01-080-3803) and $MgTi_2O_5$ (PDF Code: 00-035-0796) minor phases. $MgTiO_3$ and $CaTiO_3$ do not mix due to large ionic size difference of the cations (Mg^{2+}~0.72 Å and Ca^{2+}~1.00 Å) [42]. Therefore, a solid solution or a magnesium calcium titanate compound could not be formed at the calcination temperatures applied. The crystal structure of $MgTiO_3$ is trigonal. $CaTiO_3$ is in orthorhombic structure. $MgTi_2O_5$ formed as intermediate phase which is difficult to eliminate through the mixed-oxide route.

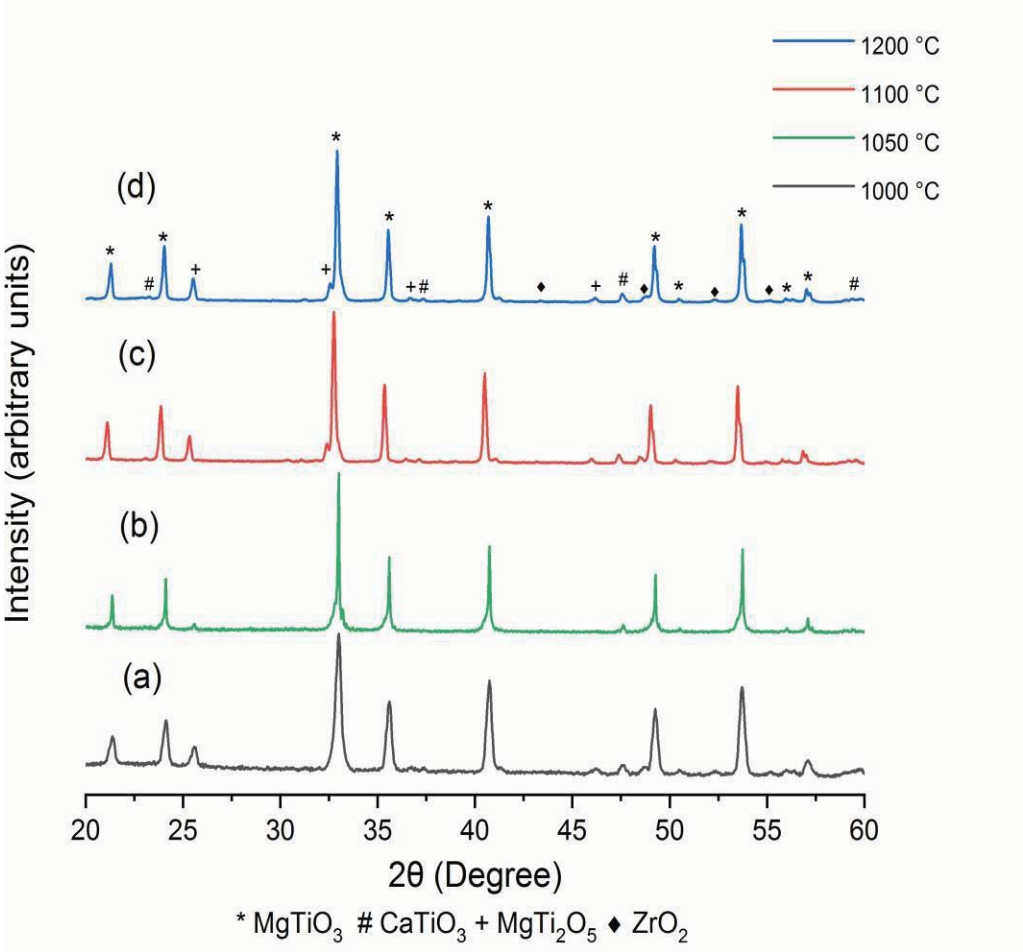

Figure 4.11. The XRD patterns of the $M_{0.95}CT$ powder calcined at (a) 1000 °C, (b) 1050 °C, (c) 1100 °C, and (d) 1200 °C for 3 h.

The XRD analysis of calcined powders produced by mixed–oxide route indicates that 1000 °C calcination temperature is enough to get desired major and minor crystalline phases. As the calcination temperature increases, broadening of the peaks decreases. It means that the particle sizes of calcined powders increases as the calcination temperature increases. Also, as calcination temperature increases, formation of $MgTi_2O_5$ intermediate phase increases. In order to prevent particle growth and minimize the formation of $MgTi_2O_5$ phase, calcination temperature was chosen as low as possible without compromising to get all major and minor phases.

The SEM images of the $M_{0.95}CT$ powders calcined at different temperatures are shown in Figure 4.12. The $M_{0.95}CT$ powders calcined at 1000 °C have very small particles and have a lot of porosity as shown in Figure 4.12(a). The observation is in accord with the XRD results. As the calcination temperature is increased, the particle size of calcined powders increased and porosities among the particles decreased at 1100 °C as illustrated in Figure 4.12(b). At 1200 °C, $M_{0.95}CT$ powders had bigger particle size and necking between the particles started. Although the powders were at calcination step, they showed the signs of sintering as shown in Figure 4.12(c). It was hard to separate calcined powders after the calcination at 1200 °C. In order to separate of the aggregated particles ball milling was applied. Hence, aggregates were broken and particles were dispersed during milling process.

By considering the XRD patterns and SEM micrographs of the calcined $M_{0.95}CT$ powders, the optimum calcination temperature and time was taken as 1050 °C for 3 h. It was determined that the calcination at 1050 °C for 3 h was enough to get major and minor phases to obtain $M_{0.95}CT$ ceramic.

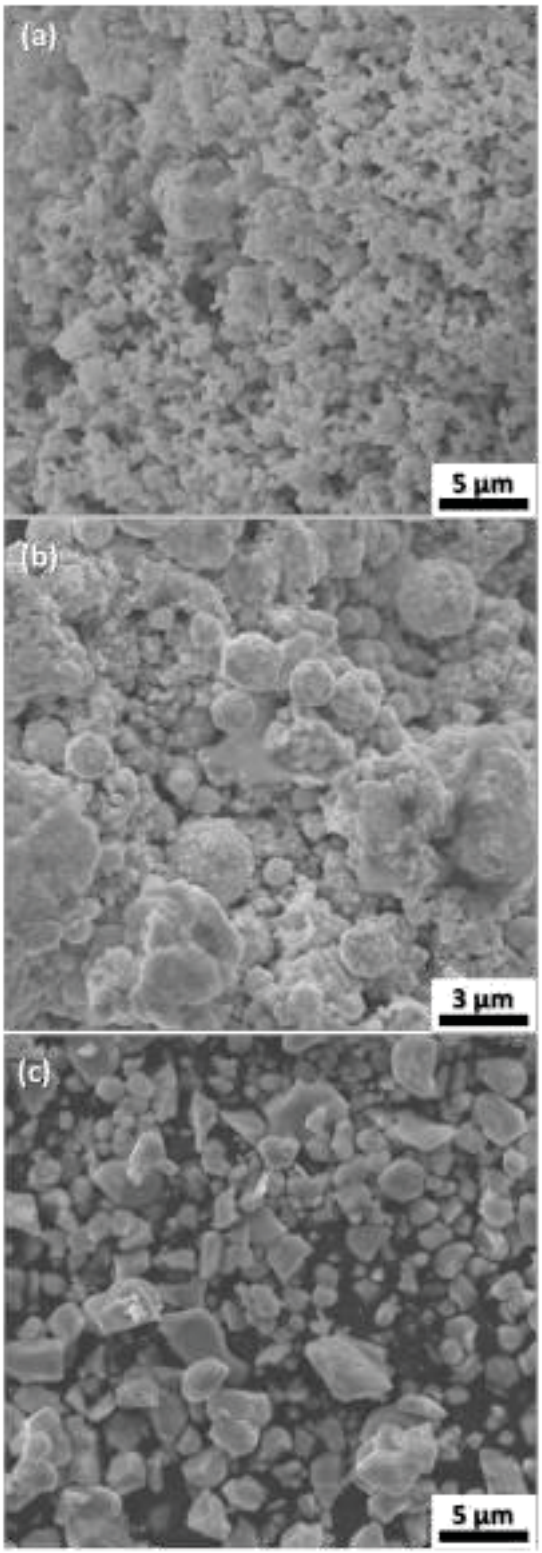

Figure 4.12. SEM images of the $M_{0.95}CT$ powder calcined at (a) 1000 °C, (b) 1100 °C and (c) 1200 °C for 3 h.

Figure 4.13 shows the SEM images of the $M_{0.95}CT$ powder two times calcined at 1050 °C for 3 h in air and subsequently ball milled. The calcined powders are submicron in size. The size is acceptable when compared with the particle size distribution data. The calcined powders have good chemical reactivity on account of fine particle size. It is clear that the calcined $M_{0.95}CT$ particles are in submicron size of various irregular shapes, which started necking and chemically reacted at high temperatures.

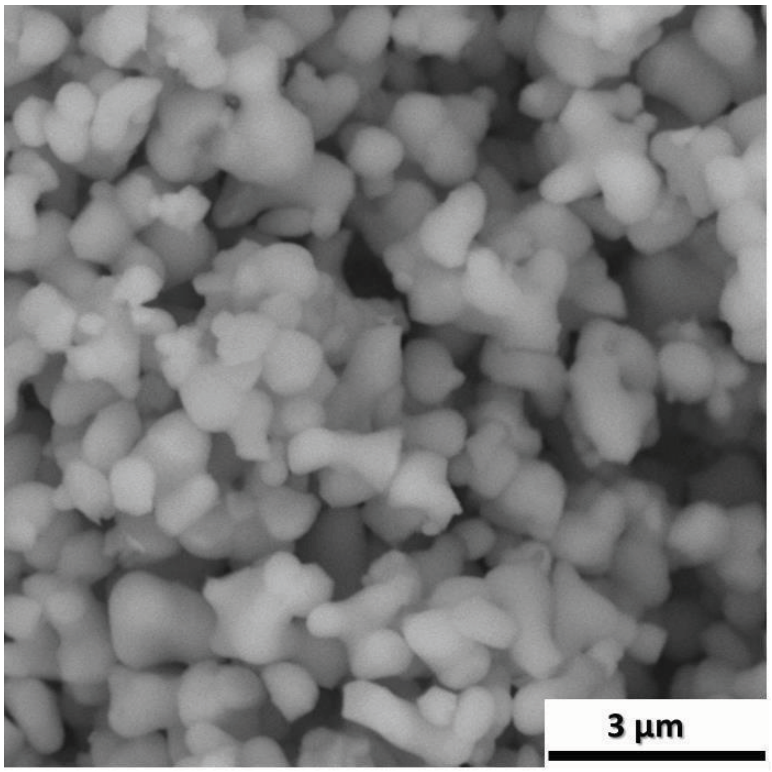

Figure 4.13. SEM micrograph of the $M_{0.95}CT$ powder two times calcined at 1050 °C and subsequently milled.

In Figure 4.14, the EDS spectrum of the $M_{0.95}CT$ powder two times calcined at 1050 °C and subsequently ball milled is shown. Mg, Ca, Ti, and O elements were detected. C element was excluded from the analysis because the powder was coated with C in order to get conductive surface for EDS and SEM analyses. The EDS analysis data of the $M_{0.95}CT$ powder two times calcined at 1050 °C and subsequently ball milled are listed in Table 4.4 in terms of the atomic percent (at%) and weight percent (wt%) concentrations of the elements.

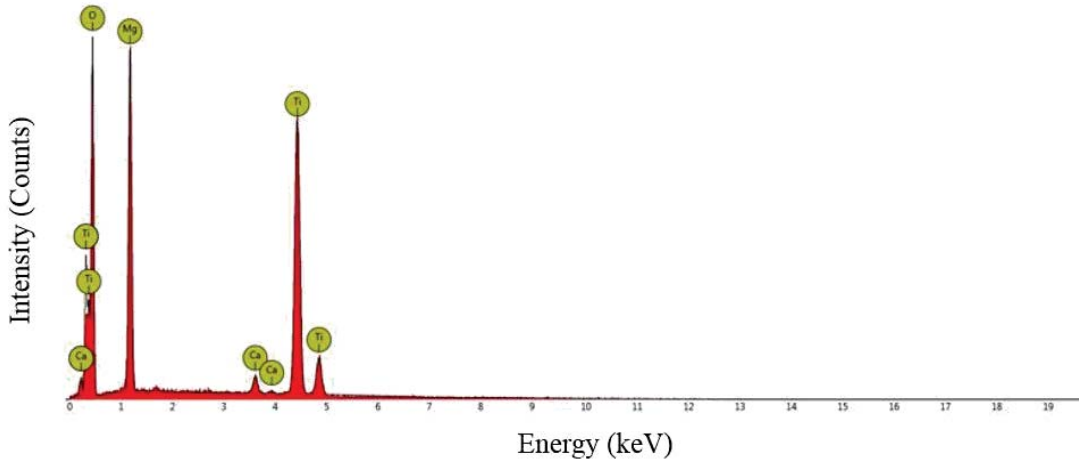

Figure 4.14. EDS spectrum of the $M_{0.95}CT$ powder two times calcined at 1050 °C and subsequently milled.

Table 4.4. *EDS analysis of the $M_{0.95}CT$ powder two times calcined at 1050 °C and subsequently milled.*

Element Symbol	Atomic Concentration (%)	Weight Concentration (%)
O	70.11	50.53
Ti	15.34	33.07
Mg	13.89	15.20
Ca	0.66	1.19

4.1.3. Sintering of $M_{0.95}CT$ Ceramics

The sintering behavior of $M_{0.95}CT$ powder was investigated in situ using high temperature XRD at temperatures from room temperature (RT) to 1250 °C. Real sintering profile cycle was applied to $M_{0.95}CT$ powder. The first XRD pattern (Figure 4.15(a)) is the pattern taken at RT. Then, the sample was heated from RT to the 600 °C at a rate of 4 °C/min. When the sample reached to 600 °C, XRD pattern shown in Figure 4.15(b) was recorded. The sample was held at 600 °C for 30 min in order to remove organics, and XRD analysis was conducted again (Figure 4.15(c)). After that, the sample was heated up to 1250 °C and at the first moment at 1250 °C, the XRD diffraction profile was recorded (Figure 4.15(d)). Finally, the sample was sintered at 1250 °C for 4 h. At the end of 4 h and before the cooling stage, the XRD pattern shown

in Figure 4.15(e) was taken. The last XRD diffraction pattern was obtained at the end of the entire sintering cycle at RT (Figure 4.15(f)). $MgTiO_3$ formed as main crystalline phase whereas, $CaTiO_3$ and $MgTi_2O_5$ phases were observed as minor phases. Since the starting material was the $M_{0.95}CT$ powder two times calcined at 1050 °C and subsequently ball milled, $MgTi_2O_5$ phase was detected even in the pattern taken at RT. Graphite peaks in the patterns came from base plate during XRD analysis.

The XRD sintering profiles revealed that the formation and amount of intermediate $MgTi_2O_5$ phase increases as temperature increases. Because of larger crystallite size, the narrower peaks are observed with increasing temperature from RT to 1250 °C. Peaks shifted slightly to higher angels because of the thermal expansion.

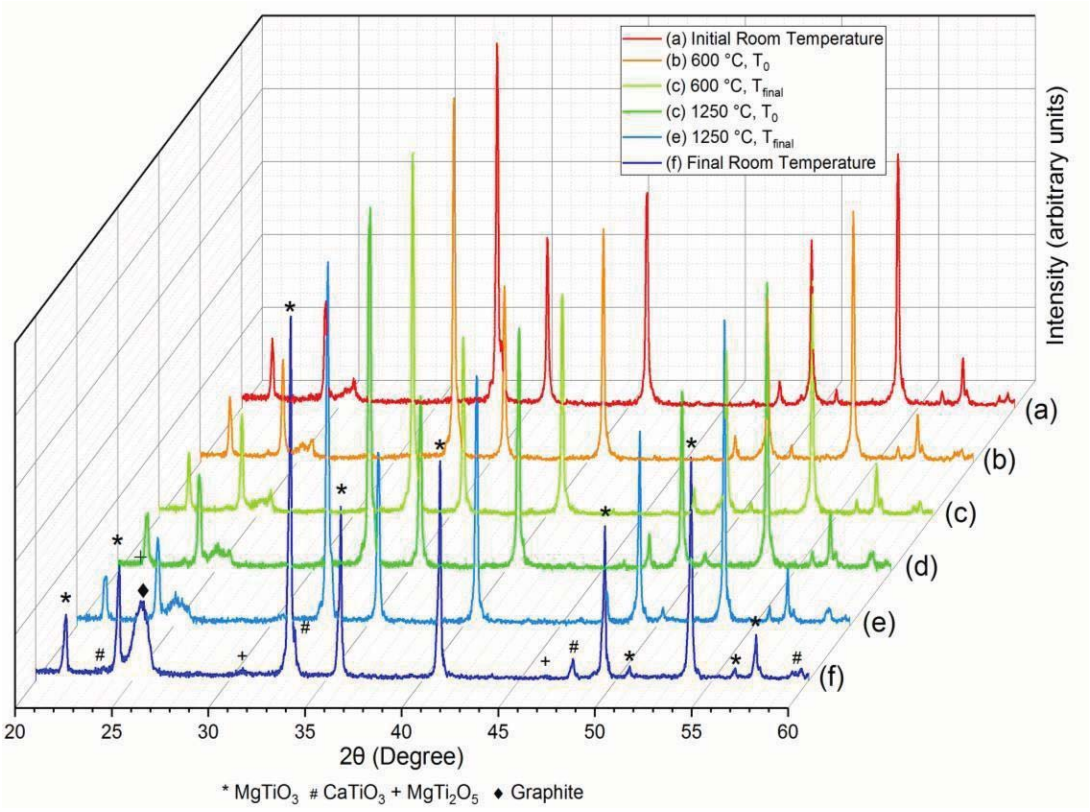

Figure 4.15. High temperature XRD sintering profiles of the $M_{0.95}CT$ ceramic.

The $M_{0.95}CT$ powders twice calcined at 1050 °C and subsequently ball milled were sintered at 1200 °C for 4 h, at 1225 °C for 2 and 4 h, at 1250 °C for 2, 4 and 6 h, and at 1300 °C for 2, 4 and 6 h. XRD patterns of the $M_{0.95}CT$ ceramics sintered at 1200, 1225, 1250, and 1300 °C for 4 h are shown in Figure 4.16. The major phase ($MgTiO_3$) and minor phases ($CaTiO_3$ and $MgTi_2O_5$) were detected in all patterns. Also small XRD peaks belonging to ZrO_2 (PDF number: 01-073-0958), presumably came from milling operation, was detected in all patterns. At the powder preparation step, the calcined powders were ball-milled for 18 h with zirconia balls. ZrO_2 balls abraded during ball-milling process and entered in the composition as contamination.

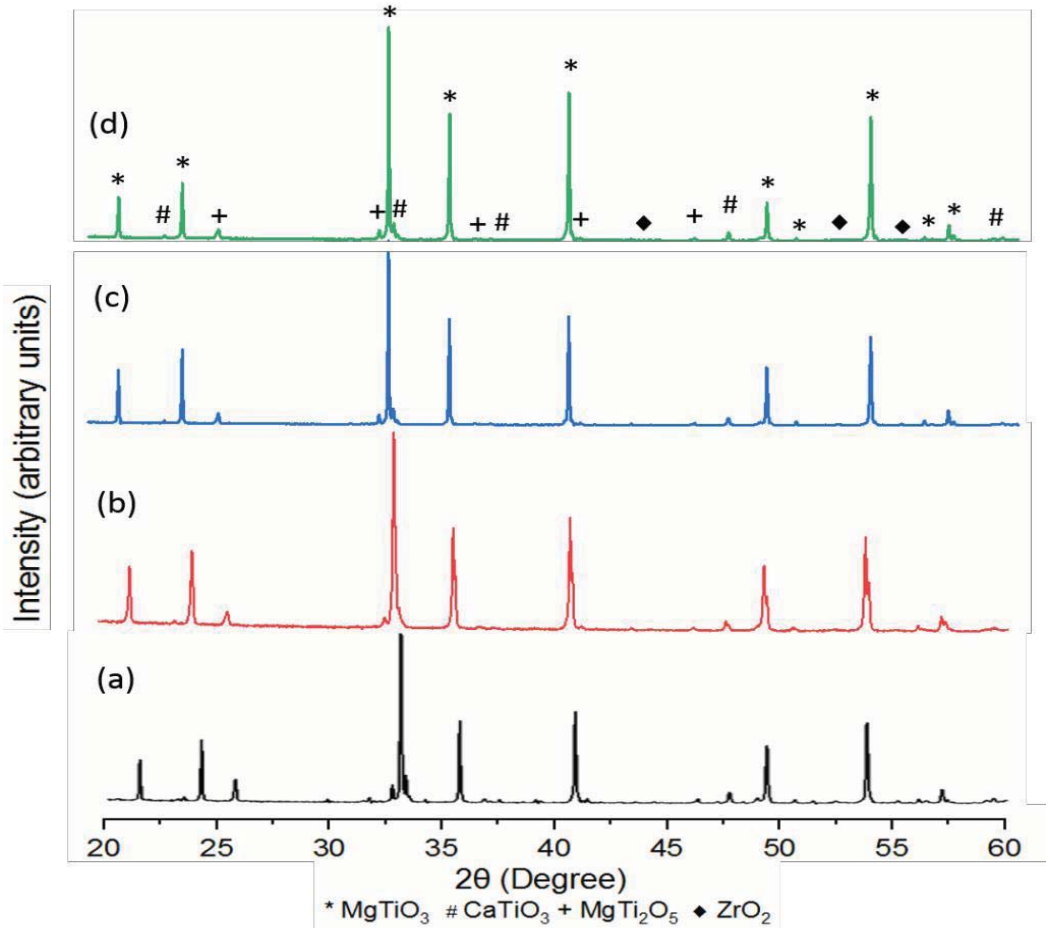

Figure 4.16. XRD patterns of the $M_{0.95}CT$ ceramics sintered at (a) 1200, (b) 1225, (c) 1250, (d) 1300 °C for 4 h.

At high-temperature XRD analysis, ZrO_2 phase was not observed. In order to simulate the real sintering cycle with in-situ XRD technique, the XRD peaks were taken at 4 °/min scanning rate. On the contrary, the bulk XRD analysis was conducted at 0.1°/min scanning rate. As a consequence, very small amount of ZrO_2 phase could not be detected with fast scanning rate at 4 °/min when compared to 0.1 °/min. It is obvious that amount of the unwanted $MgTi_2O_5$ intermediate phase decreases as sintering temperature increases.

The XRD pattern of the $M_{0.95}CT$ ceramic sintered at 1200 °C for 4 h, as separately shown in Figure 4.17, suggested that the number of peaks for the $MgTi_2O_5$ intermediate phase was too much because of large amount of $MgTi_2O_5$ phase formed during sintering. In order to eliminate or minimize unwanted $MgTi_2O_5$ phase, higher sintering temperatures were applied.

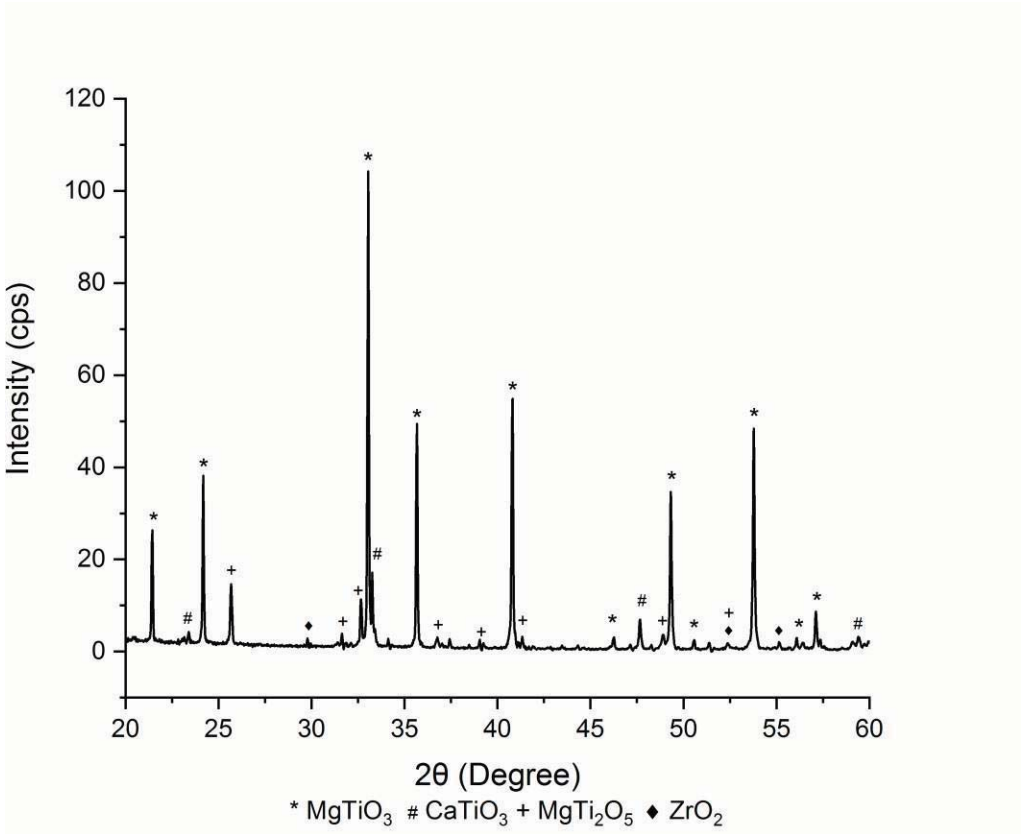

Figure 4.17. XRD pattern of the $M_{0.95}CT$ ceramic sintered at 1200 °C for 4 h.

SEM images taken from the flat and fracture surfaces of the $M_{0.95}CT$ ceramic sintered at 1200 °C for 4 h were shown in Figure 4.18. A porous microstructure developed after sintering at 1200 °C. Pores as big as 2 μm along with large and small grains were observed in the microstructure. The grain sizes ranged between 1 and 5 μm. As seen in Figure 4.18(b), bonding and necking started between the particles. It is obvious that higher sintering temperatures are needed to eliminate or minimize the pores.

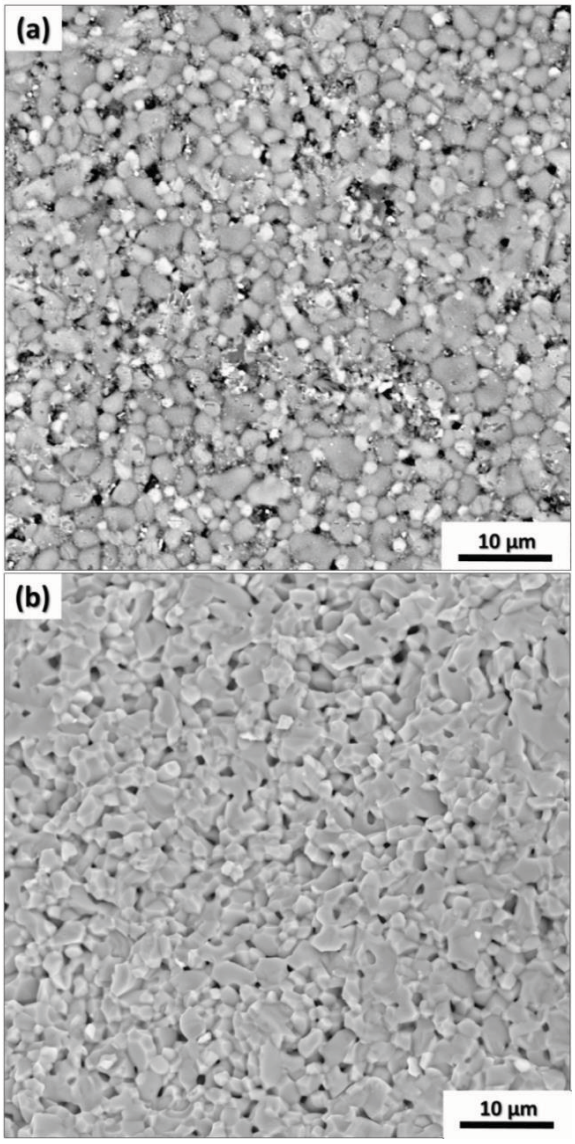

Figure 4.18. SEM micrographs of *the* $M_{0.95}CT$ ceramic sintered at 1200 °C for 4 h. Images are taken from (a) flat surface (b) fresh fractured surface.

XRD patterns of the $M_{0.95}CT$ ceramic sintered at 1225 °C for 2 and 4 h were illustrated in Figure 4.19. Major and minor phases were identified in both patterns. No significant difference was noted between the XRD patterns in terms of the phases developed, their peak intensities and widths. This finding implies that 2 h increase in sintering at 1225 °C has insignificant effect on the phases developed but influences the amount of the phases developed during sintering.

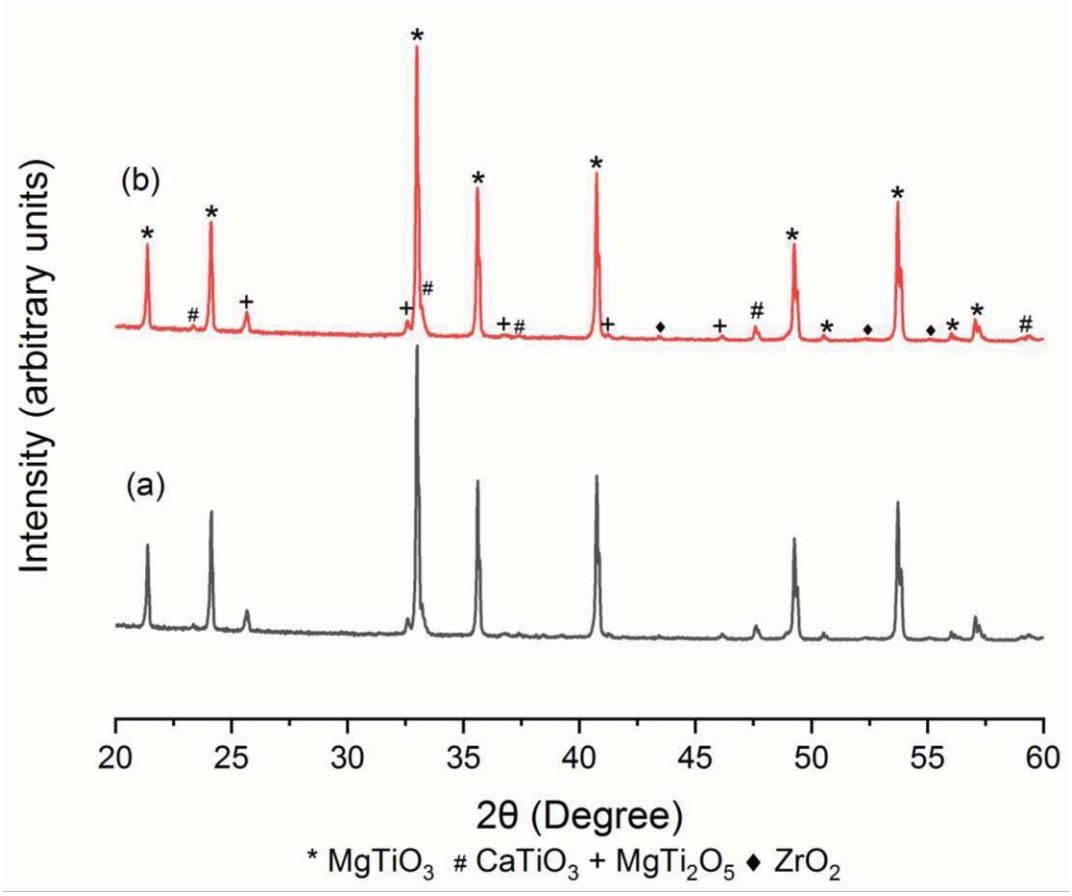

Figure 4.19. XRD patterns of the $M_{0.95}CT$ ceramic sintered at 1225 °C for (a) 2 h and (b) 4 h.

When a comparison is made between the XRD patterns of the $M_{0.95}CT$ ceramic sintered at 1200 and 1225 °C, Figures 4.17 and 18(b), it is recognized that amount of the unwanted $MgTi_2O_5$ intermediate phase decreases as sintering temperature increases. See also Figure 4.16. The $MgTi_2O_5$ intermediate phase can easily form in MgO-CaO-TiO_2 system at lower sintering temperatures when prepared via

conventional mixed-oxide method. Baek et al. [43] reported that this intermediate phase comes from the segregation of unreacted MgO and TiO_2 after the initial mixing of powders. The formation of $MgTi_2O_5$ may be due to the decomposition of $MgTiO_3$ according to the reaction $2MgTiO_3 \rightarrow MgO+MgTi_2O_5$. As a consequence, sintering reaction between $MgTi_2O_5$ and MgO at higher sintering temperatures allow to formation of high amount of $MgTiO_3$ phase. Liou et al. [44] investigated the amount of $MgTi_2O_5$ phase formation in the MgO-CaO-TiO_2 system and reported that 45.6% and 37.2% of $MgTi_2O_5$ phase formed after 2 h sintering at temperatures of 1150 and 1300 °C, respectively. It is obvious that higher sintering temperatures are needed to convert $MgTi_2O_5$ intermediate phase to $MgTiO_3$.

In Figure 4.20, SEM images of fresh fracture surfaces of the $M_{0.95}CT$ ceramics sintered at 1225 °C for 2 and 4 h were shown. As compared to 1200 °C, the number of pores slightly decreased with increasing sintering temperature although the pores as big as 2 μm were present. As sintering temperature was increased, size of the grains increased too. The increase in grain size with increasing sintering temperature can be explained with the relation between diffusion and sintering temperature. With increasing sintering temperature, the number of grain boundary decreases as a result of increasing diffusion between grains in microstructure [45].

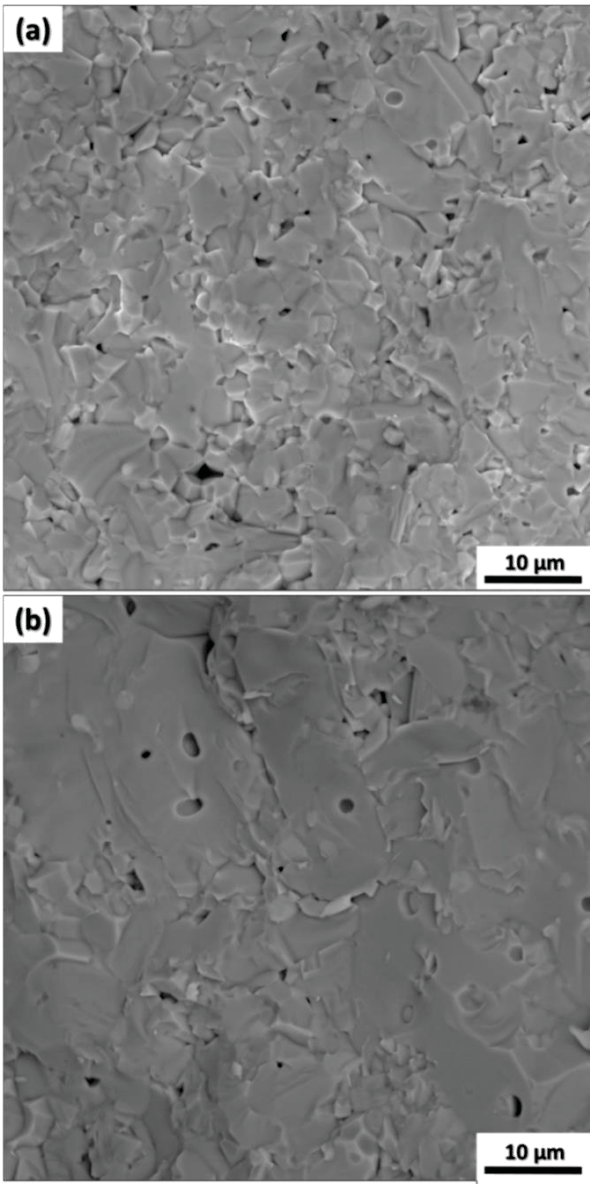

Figure 4.20. SEM micrographs of *the* $M_{0.95}CT$ ceramic sintered at 1225 °C for (a) 2 h and (b) 4 h.

In order to eliminate or minimize the porosity in the microstructure, sintering temperature was raised to 1250 °C. The XRD patterns of the $M_{0.95}CT$ ceramics sintered at 1250 °C for for 2, 4, and 6 h are shown in Figure 4.21. With increasing sintering temperature and sintering time, XRD peaks became sharper which was related to increasing grain size. $CaTiO_3$ peaks were detected in the patterns more clearly as sintering time and temperature increased. Also, some of the peaks for the $MgTi_2O_5$ intermediate phase disappeared as sintering time inceased.

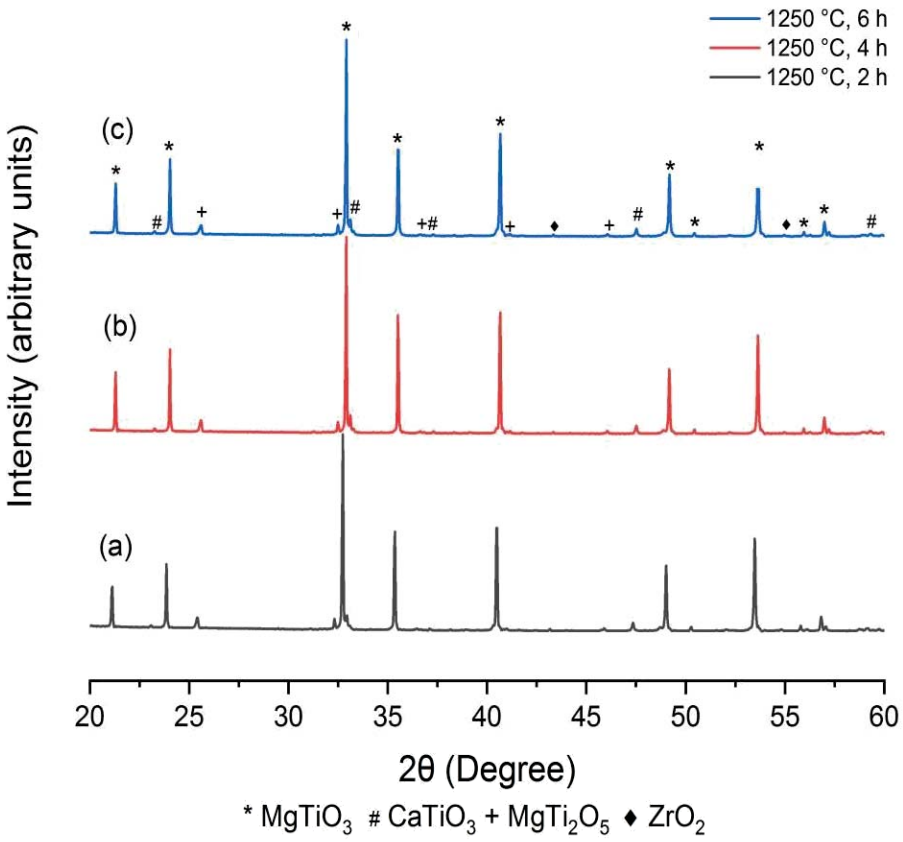

Figure 4.21. XRD patterns of the $M_{0.95}CT$ ceramics sintered at 1250 °C for (a) 2 h, (b) 4 h, and (c) 6 h.

The SEM images representing the microstructure of the $M_{0.95}CT$ ceramic sintered at 1250 °C for 2, 4, and 6 h are given in Figure 4.22. The SEM images prove that the $M_{0.95}CT$ ceramic sintered at 1250 °C has denser microstructure. Less number of small pores at the grain boundaries were observed. Two types of grains (large grains and small cubic-shaped grains) were noticed. The shoulder seen in the particle size distribution curve of the calcined $M_{0.95}CT$ powder may cause the formation of a microstructure with heterogeneous grains. It was not possible to measure the exact grain sizes from the images. For all sintering times at 1250 °C, dense microstructure was achieved.

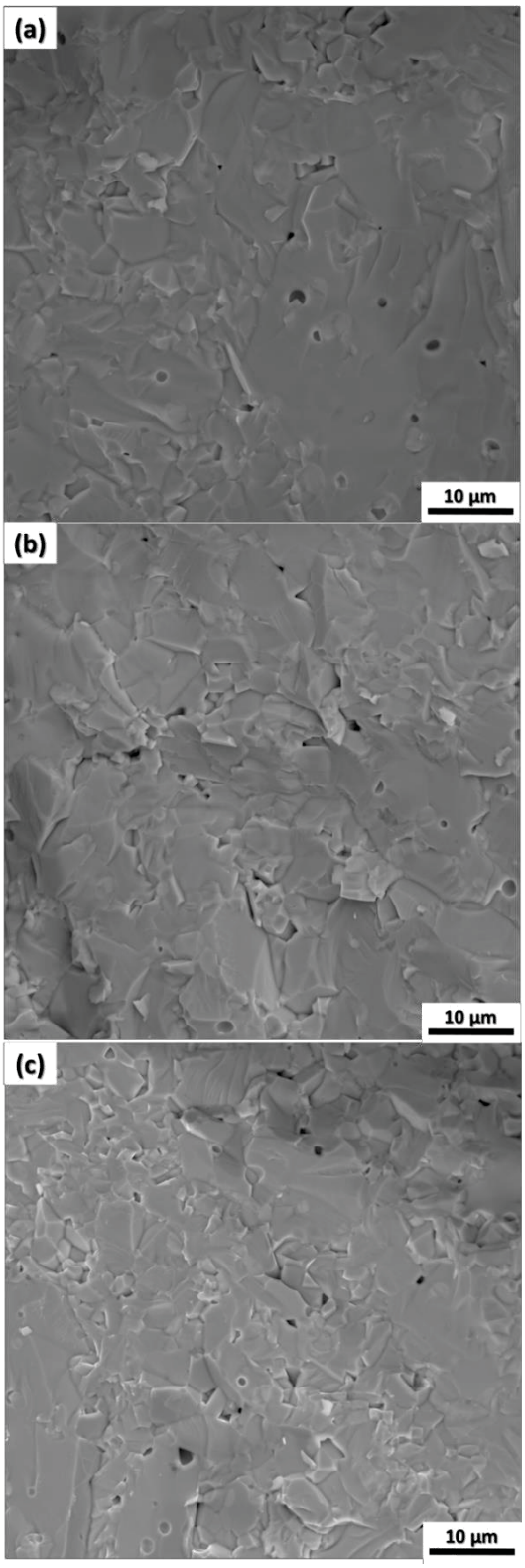

Figure 4.22. SEM images of the $M_{0.95}CT$ ceramic sintered at 1250 °C for (a) 2 h, (b) 4 h, and (c) 6 h.

The SEM images taken from the flat surface and fresh fractured surface of the $M_{0.95}CT$ ceramic sintered at 1250 °C for 4 h are shown in Figures 4.23(a) and (b), respectively. Surface and fractured surface images of specimens were alike. Very small amount of fine pores were detected in the microstructure, implying high densification.

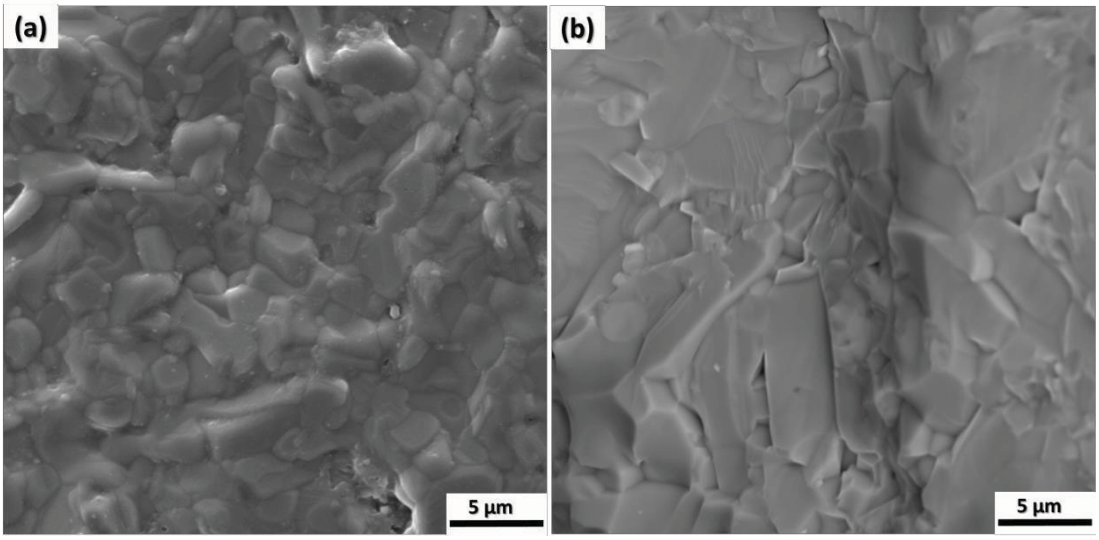

Figure 4.23. SEM images taken from (a) flat surface and (b) fresh fractured surface of the $M_{0.95}CT$ ceramic sintered at 1250 °C for 4 h.

The EDS analysis revealed that Mg, Ti, Ca, Si, Zr, and O elements were present in the sample. The concentrations of the elements present in the sample were listed in Table 4.5. A small amount of Si that came from starting MgO powder and of ZrO_2 that came from the ball milling process were detected. The intended concentrations of Ti, Mg, and Ca in the starting powders to prepare the $M_{0.95}CT$ ceramic were 38, 18.2, and 1.6 wt%, respectively. The EDS analysis suggested that the $M_{0.95}CT$ ceramic has slightly different composition than the intended composition. The difference may be due the nature of mixed-oxide production method. During fabrication of ceramic pieces, the powders are mixed, ball milled, crushed, and sieved. The material loss could occur during processing. Therefore, ceramics of different compositions could be produced.

Table 4.5. *EDS analysis for the $M_{0.95}CT$ ceramic sintered at 1250 °C for 4 h.*

Element Symbol	Atomic Concentration (%)	Weight Concentration (%)
O	67.88	47.97
Ti	15.95	33.72
Mg	15.11	16.23
Ca	0.82	1.44
Si	0.13	0.16
Zr	0.12	0.48

In order to get a more precise and dependable data for the chemical composition, X-ray Fluoresans (XRF) analysis were performed on the $M_{0.95}CT$ ceramic sintered at 1250 °C for 4 h. XRF can achieve higher precision and has better sensitivity than EDS, because XRF analysis provide lower background when compared with EDS [46, 47]. Thanks to lower background, the element detection limit and the sensitivity are enhanced to a degree that trace elements can be easily and accurately detected with XRF. The wt% concentration of the elements present in the sample was presented in Table 4.6. The weigh concentrations of the Ti, Mg, and Ca elements were more or less the same as the intended concentrations. Different elements (P, Al, and Fe) were also identified as impurities that could not be detected with EDS and XRD analyses since the quantities of these impurity elements are less than the detection limits for the EDS and XRD analyses techniques. According to XRF analysis the sintered $M_{0.95}CT$ ceramic has approximately 2 wt% impurity elements. This result is reasonable when compared with the total impurity amount present in the starting powders that have roughly 2.5 wt%.

Table 4.6. *XRF analysis for the $M_{0.95}CT$ ceramic sintered at 1250 °C for 4 h.*

Element Symbol	Weight Concentration (%)
Ti	37.1
O	36.9
Mg	12.5
C	10.5
Ca	1.59
Si	0.496
P	0.455
Al	0.176
Zr	0.145
Fe	0.0361

Large and cubic-shaped small grains were observed in the microstructures of the $M_{0.95}CT$ ceramics sintered at 1250 °C for all sintering times. The chemical compositions of the large and small grains, shown in Figure 4.24, were identified via EDS analysis for all of the samples sintered at this temperature and shown in Table 4.7. Spot A represents the large grains, which is rich in Mg and Ti elements. Spot B represents the cubic-shaped small grains, which includes Ca and Ti elements. In spot A, atomic concentrations of Mg to Ti are approximately equal to 1. Therefore it can be said that spot A is the $MgTiO_3$ crystal. For Spot B, EDS analysis revealed that the atomic concentrations of Ca:Ti are nearly 1:1. Thus, spot B illustrates the $CaTiO_3$ crystal. It was unlikely to distinguish the small amount of $MgTi_2O_5$ intermediate phase in the microstructure because it was not possible to observe a spot with different contrast. As the elements in the $MgTiO_3$ and $MgTi_2O_5$ phases have the same atomic numbers, the differentiation of $MgTiO_3$ and $MgTi_2O_5$ crystals was not possible even with the back scatterred electrons.

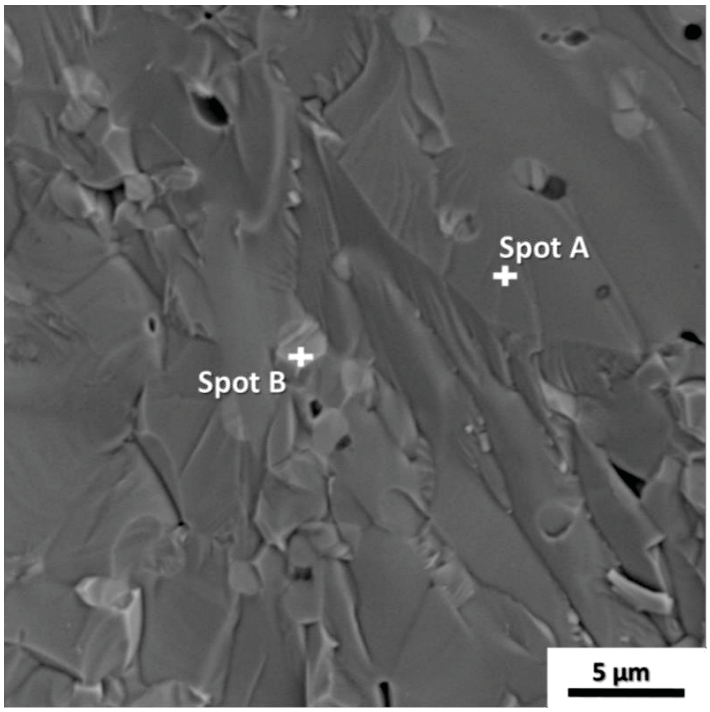

Figure 4.24. The SEM image of the $M_{0.95}CT$ ceramics sintered at 1250 °C for 4 h.

Table 4.7. *EDS analysis of Spot A and Spot B shown in Figure 4.24.*

Element Symbol	Spot A		Spot B	
	Atomic Concentration (%)	Weight Concentration (%)	Atomic Concentration (%)	Weight Concentration (%)
O	66.83	48.15	82.67	64.54
Mg	18.47	20.22	2.00	2.37
Ti	14.52	31.30	8.20	19.15
Ca	0.18	0.33	7.13	13.94

The XRD patterns for the $M_{0.95}CT$ ceramics sintered at 1300 °C for 2, 4, and 6 h are illustrated in Figure 4.25. No significant difference was recognized in the patters taken at various sintering durations. Major crystalline phase was $MgTiO_3$ in all patterns. $CaTiO_3$ was detected as minor phase and $MgTi_2O_5$ phase was observed as intermediate phase.

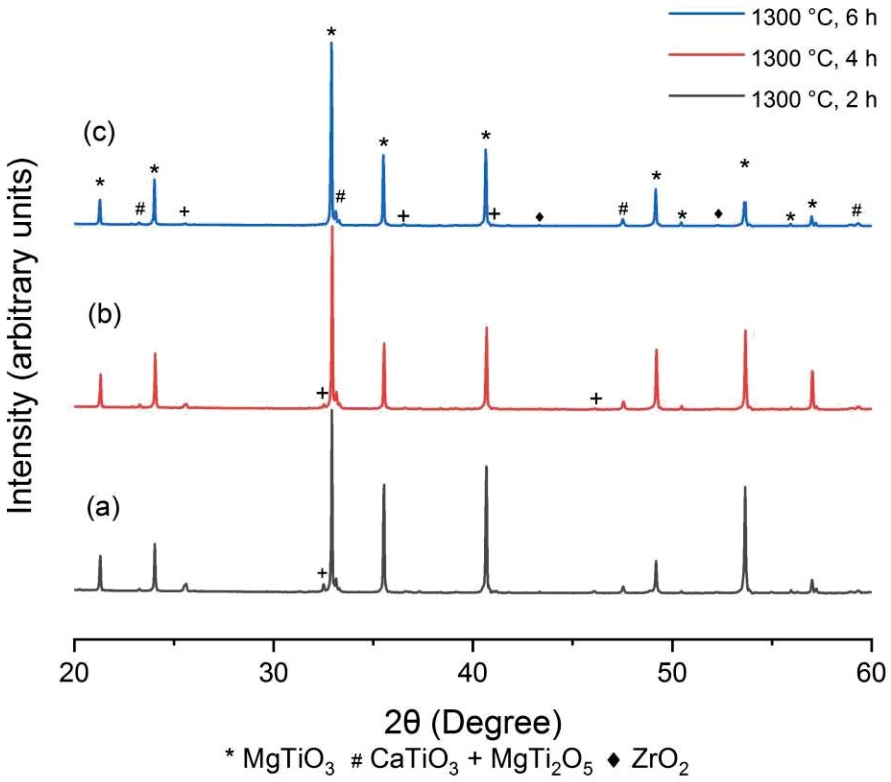

Figure 4.25. XRD patterns of the $M_{0.95}CT$ ceramics sintered at 1300 °C for (a) 2 h, (b) 4 h, and (c) 6 h.

It was noted that as sintering temperature was increased from 1250 °C to 1300 °C, the amount of $CaTiO_3$ decreased. The development of $MgTi_2O_5$ intermediate phase decreased at 1300 °C for 6 h sintering as compared to the sintering for 2 and 4 h. Moreover, major XRD peaks became sharper with increasing sintering time implying that larger grains were obtained for longer sintering durations.

The SEM images of $M_{0.95}CT$ ceramics sintered at 1300 °C for 2, 4, and 6 h was illustrated in Figure 4.26. At 1300 °C, the sizes of grains abnormally grew and reached up to approximately 100 µm. For 6 h sintering at 1300 °C, grain boundaries were easily recognized. Very large $MgTiO_3$ grains and pores as big as 100 µm were observed in the microstructure. $CaTiO_3$ grains located both in the grains and at the grain boundaries. Observations are in accord with those reported by Pigai et al. [48]

who stated that with increasing sintering temperature and abnormal grain growth of $MgTiO_3$ grains, $CaTiO_3$ can occur both at grain boundaries and within grains of $MgTiO_3$.

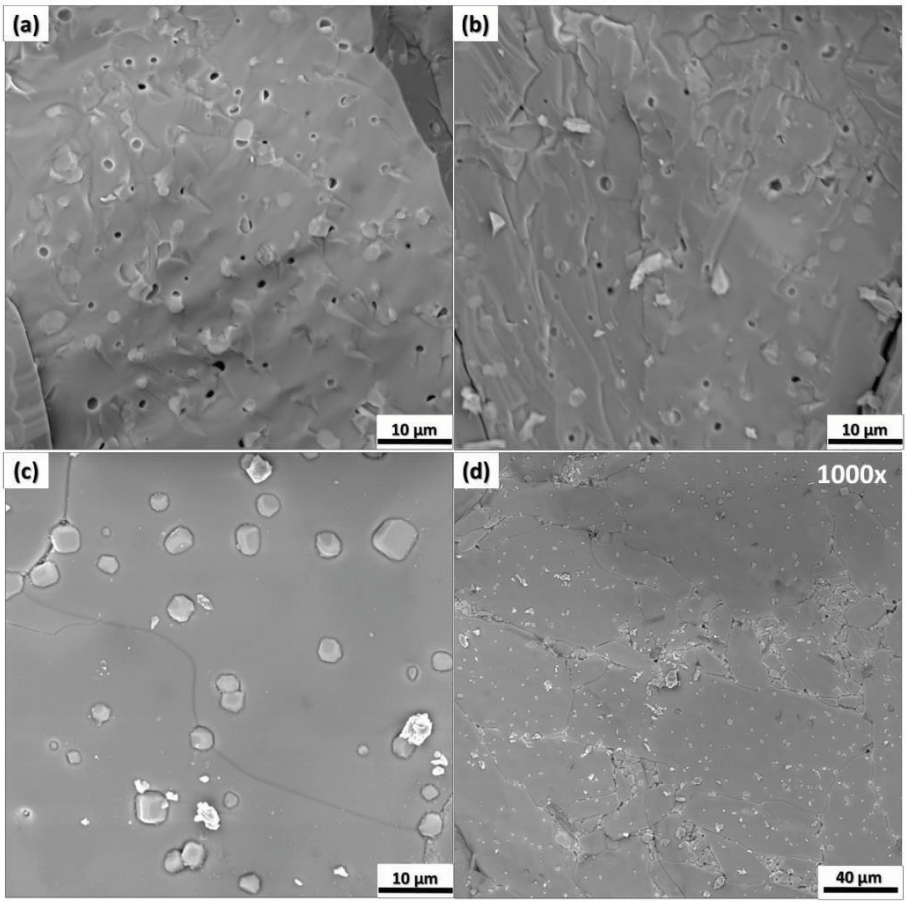

Figure 4.26. SEM micrographs of the $M_{0.95}CT$ ceramic sintered at 1300 °C for (a) 2 h, (b) 4 h, and (c,d) 6 h.

4.1.4. Properties of $M_{0.95}CT$ Ceramics

4.1.4.1. Density

The sintered density of the $M_{0.95}CT$ ceramics prepared were measured by the Archimedes method as described in Section 3.3.1. Densities of the $M_{0.95}CT$ ceramics sintered at different sintering conditions are listed in Table 4.8. The plus minus signs in the table indicate ± 1 standard deviation from the determinations. The density

results suggest that the reproducibility of the data is very good since the deviations from the determinations are very small. The good reproducibility of the values is attributed to chemical and microstructural homogeneity of the test samples. The variations in sintered density of the $M_{0.95}CT$ ceramics prepared with sintering temperature and sintering time are shown in Figures 4.27 and 4.28, respectively. The maximum density was achieved for the $M_{0.95}CT$ ceramic sintered at 1250 °C for 4 h. The density of the $M_{0.95}CT$ ceramic sintered at 1300 °C for 2 h was close to that sintered at 1250 °C for 4 h. It is obvious that with increasing sintering time at 1300 °C, sintered density of the $M_{0.95}CT$ ceramics decreased because of the abnormal grain growth that caused the coalescence of the pores present in the microstructure. Silverman [49] publicized that at elevated temperatures it is possible to observe abnormal grain growth because lattice imprefections are increased with increasing sintering temperatures. For lower sintering temperatures, lower densities were realized because of the insufficient diffusion rates.

Table 4.8. *Density of the $M_{0.95}CT$ ceramics sintered at different sintering conditions.*

Sintering Temperature (°C)	**Sintering Time (h)**	**Sintered Density (g/cm^3)**
1200	4	3.451±0.006
1225	2	3.715±0.007
1225	4	3.763±0.007
1250	2	3.799±0.006
1250	4	3.824±0.006
1250	6	3.789±0.002
1300	2	3.801±0.004
1300	4	3.775±0.009
1300	6	3.768±0.01

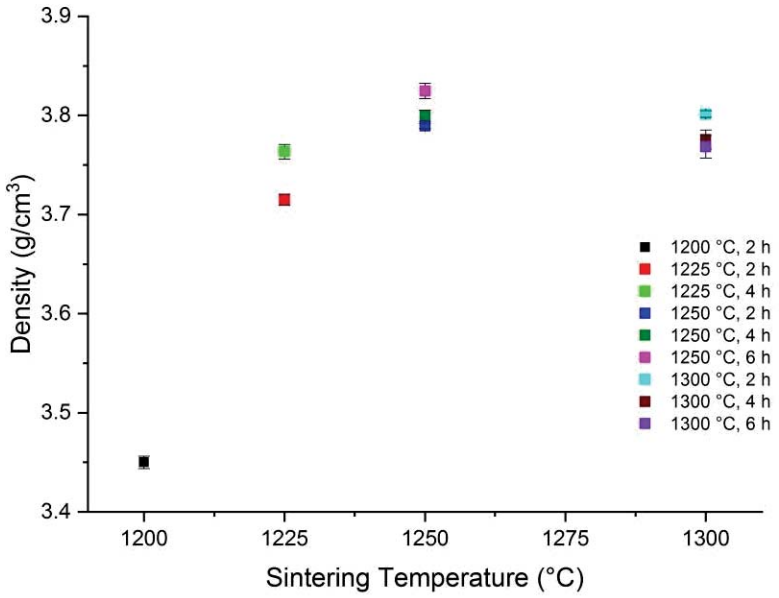

Figure 4.27. Sintered density vs sintering time graph of the $M_{0.95}CT$ ceramics for different sintering temperatures.

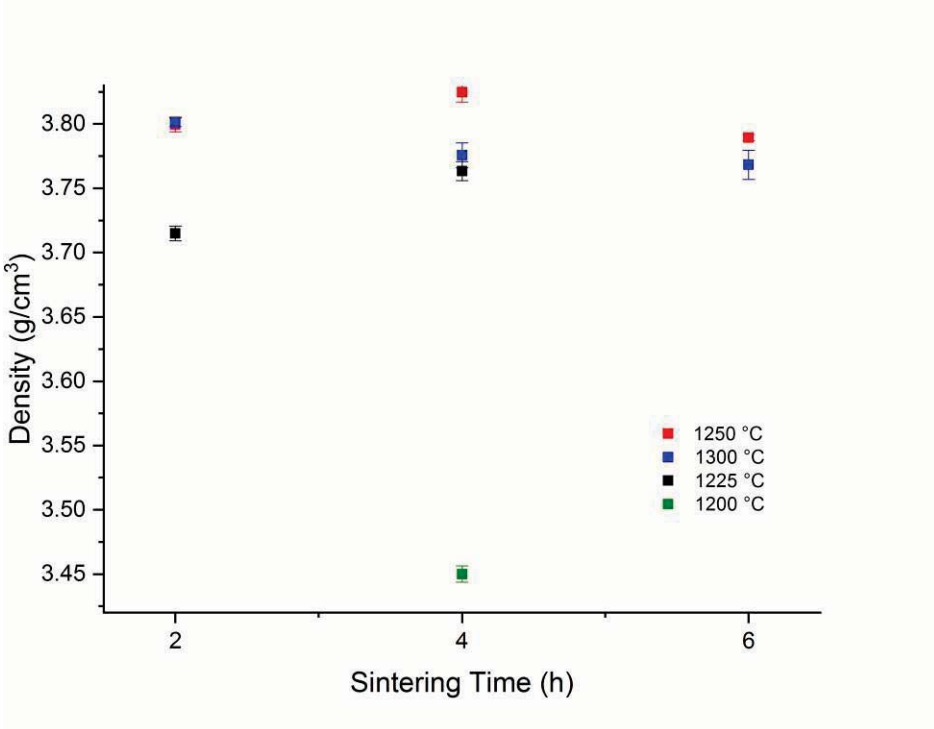

Figure 4.28. Sintered density vs sintering temperature graph of the $M_{0.95}CT$ ceramics for different sintering durations.

In order to verify the density values as determined by the Archimedes' method, an image analysis was performed on the $M_{0.95}CT$ ceramic sintered at 1250 °C for 4 h. The SEM images taken from the polished surface, shown in Figure 4.29, were considered for the analysis. ImageJ software® was used to get numerical porosity content of the sample. The numerical determination was calculated by the ratio of average total porosity area to average total image area. The average porosity of the sample was measured as 2.7%. As a result of this value, a relative density (sintered density/theoretical density) of 97.3% was calculated from the ImageJ analysis. The theoretical density of $M_{0.95}CT$ ceramic was calculated 3.92 g/cm^3 as described in Appendix 1. The relative density value of 97.3% calculated by using the ImageJ analysis coincides with the relative density value of 97.5% as calculated by the Archimedes method. In calculation of the theoretical density the lattice crystallographic parameters given in the PDF card of $MgTiO_3$ (a=5.054 Å, c=13.898 Å), of $CaTiO_3$ (a=5.380 Å, b=5.4337 Å, c=7.6269 Å), and of $MgTi_2O_5$ (a=9.7274, b=10.0040 and c=3.7428) were taken into consideration.

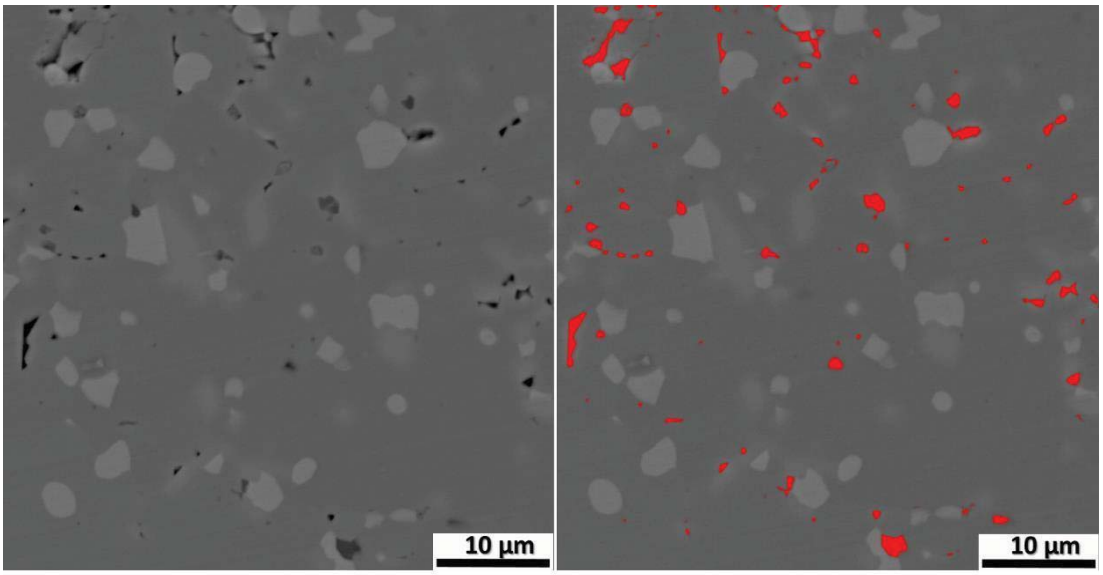

Figure 4.29. ImageJ analysis of polished surface of the $M_{0.95}CT$ ceramic sintered at 1250 °C for 4 h.

The relative density for the $M_{0.95}CT$ ceramics sintered at 1200, 1225, 1250, and 1300 °C for 4 h were 88%, 96%, 97.5%, and 96%, respectively. The variation in relative density with sintering temperature is shown in Figure 4.30. The relative density of the $M_{0.95}CT$ ceramics increased with increasing temperature up to 1250 °C. Further increase in sintering temperature to 1300 °C for 4 h, resulted in a slight decrease in the relative density because lattice imprefections increased with increasing sintering temperatures. When sintering is fast with increasing sintering temperature and time, the pores inside the microstructure do not have enough time for diffusion to the grain boundaries, can not move between grains and are stucked wtihin the grains. [38, 50]. German [45] also reported that the initiation of abnormal grain growth cause from the small amount of agglomarated particles in initial powder compact. The clusters prefer coarsening; subsequently, grain size of specimens rapidly increases. Because of the rapid grain growth, the pores can not be eliminated in a short time.

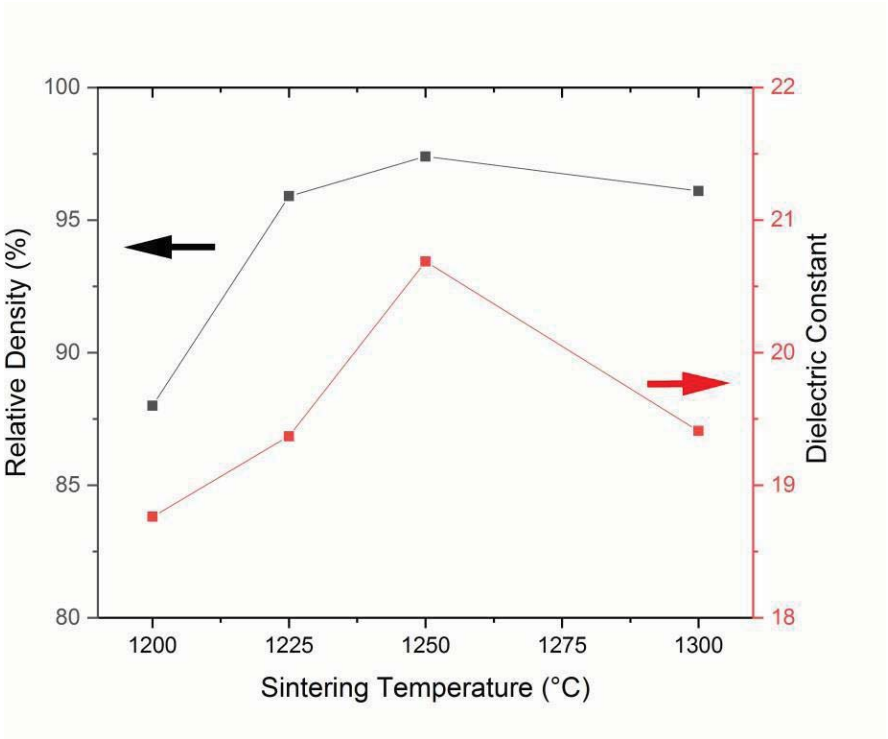

Figure 4.30. Variation in relative density and dielectric constant of the $M_{0.95}CT$ ceramics with sintering temperature.

Piagai et al. [48] synthesized MCT ceramics by semi-alkoxide method with acetate powders. They reached 97.9% relative density with nitrate powders at 1450 °C. It is commonly known that the chemical methods are more suitable to obtain pure and dense microstructure without the formation of intermediate phases. Huang et al. [11] obtained 95.8% relative density with 1.00 wt% CuO addition at 1300 °C for 4 h. In this thesis study, a 97.5% relative density was obtained by conventional mixed-oxide method without a sintering aid addition thanks to the utilization of fine particles and integration of the calcination step twice at 1050 °C for 3 h in the processing. The formation of main phase was enhanced and unwanted intermediate phases were hindered before sintering. Therefore, it was possible to obtain better densification at lower temperatures.

4.1.4.2. Dielectric Constant and Dielectric Loss

Figure 4.31 displays also the variations in dielectric constant ( ) of the $M_{0.95}CT$ ceramics sintered at 1200, 1225, 1250, and 1300 °C for 4 h with sintering temperature. The results are compatible with the density results. Similar to the density, the of the $M_{0.95}CT$ ceramics increased with increasing sintering temperature, reached the maximum at 1250 °C and than decreased at 1300 °C.

The variations in with frequency for the $M_{0.95}CT$ ceramics sintered at different sintering conditions are shown in Figure 4.32. At very low frequencies like 1 kHz and 10 kHz, parallel plate method is not suitable to measure dielectric constant or dielectric loss value. The values slightly increased at 10 MHz. From 10 kHz to 40 MHz, of the $M_{0.95}CT$ ceramics sintered at different sintering conditions remained more or less constant with increasing frequencies. Up to 10 MHz frequency, different polarization modes such as dipole, ionic or atomic can be active In association with the polarization types in domain structure, dielectric constant of material may change
[51]. For the $M_{0.95}CT$ ceramic sintered at 1250 °C for 4 h, was measured as 20 at 1 kHz. Up to 10 kHz, reached to 20.7. At 40 MHz, became 21.2. At higher frequencies (>10 MHz) parallel plate capacitor method cannot be suitable. AC with

network analyzers can be used for these kind of high frequency measurements [52]. It is known that dielectric properties of ceramics are directly related to the microstructure as grain size and defects (dislocations, grain structure and size, vacancies etc.) influence the dielectric properties [53, 54]. The microstructures with high sintered density provide the best dielectric properties since pores in the microstructure acts as a second and unwanted phase which cause poor dielectric properties. Air filled pores have of 1. Considering the Lichteneker mixing method (= · $_1$ + (1 −) ·

$_2$), pores have ln 1=0. Therefore, they do not have any contribution to the permittivity of the material. As a result, eliminating of porosity and incrasing density is important to get optimum dielectrical propeties in case of both deielectric constant and dielectric loss. [50, 51]. The highest was obtained for the M$_{0.95}$CT ceramic sintered at 1250 °C for 4 h that had the highest sintered density as shown in Table 4.8. As a result of lattice imperfections caused by high temperatures, the dielectric properties of the M$_{0.95}$CT ceramics decreased. The dielectric losses of materials are originated from mostly pores, second and unwanted phases, impurities and defects [53, 54]. More porosity and defects were detected in the microstructure of the M$_{0.95}$CT ceramic sintered at 1300 °C. Therefore, a lower dielectric constant value of 19.5 was measured when compared with 20.6 obtained for the M$_{0.95}$CT ceramic sintered at 1250 °C. Too much secondary phases and porosity present in the microstructure of the M$_{0.95}$CT ceramic resulted in lower of 18.5.

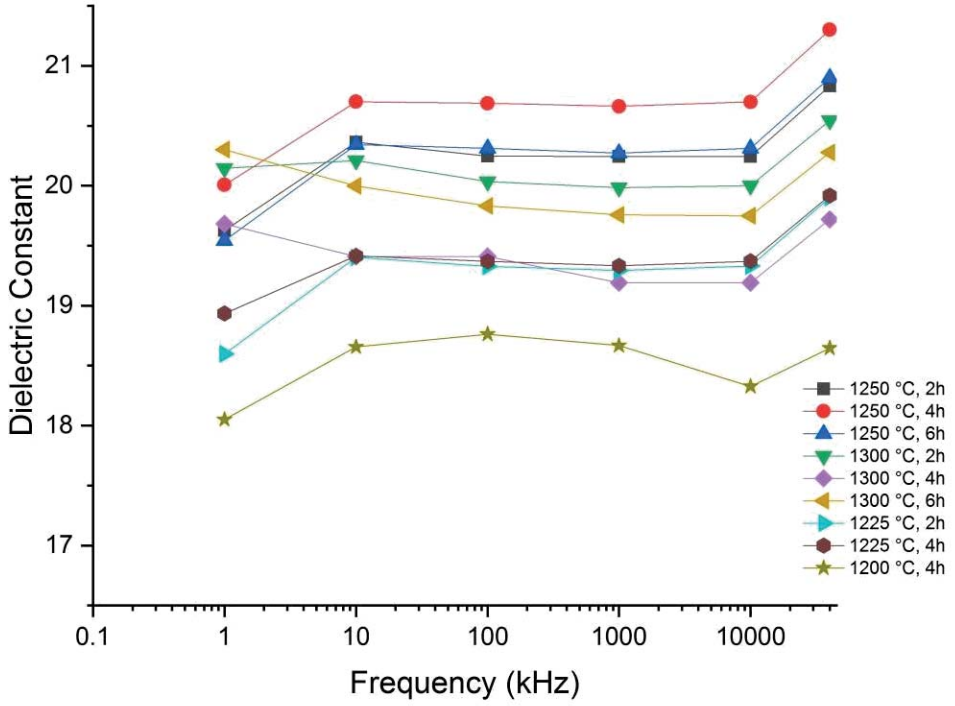

Figure 4.31. The variation of dielectric constants with frequency for the $M_{0.95}CT$ ceramics sintered at different sintering conditions.

Huang et al. [11] reported of 20 at 7 GHz with 0.25 wt% CuO addition to MgO-CaO-TiO_2 system. Sintering aid lowers the sintering temperature but decreases the dielectric properties. Piagai et al. [48] found of 20.4 at 10.3 GHz with chemical production route. Wang et al. [16] achieved of 19.4 after sintering at 1300 °C for 4 h via conventional mixed-oxide method. In this thesis work, of 20.6 was obtained at 10 MHz due to the better densification provided by the application of improved processing steps.

The losses of a dielectric ceramic depend on both intrinsic and extrinsic losses [30]. In the low field dielectric property calculations, extrinsic losses play an important role in terms of porosity, second phase formation, grain size and defects in microstructure. In Figure 4.32, the dielectric losses of the $M_{0.95}CT$ ceramics prepared was shown as a function of frequency. At 1 kHz frequency, the precise measurement was not possible.

With increasing frequency, the dielectric loss values decreased up to 1000 kHz frequency then increased again. As mentioned above, in order to obtain more precise dielectric measuremnts with increasing frequency, the dielectric measurement method must be changed. Parallel plate method cannot give the reliable results up to 10^6 kHz frequency [52]. However, at the frequencies ranging from 10 kHz to 10^6 kHz, dielectric loss values of the $M_{0.95}CT$ ceramics were similar. The dielectric losses varied in parallel to the sintering time. The minimum dielectric loss was obtained from the $M_{0.95}CT$ ceramic sintered at 1250 °C for 4 h.

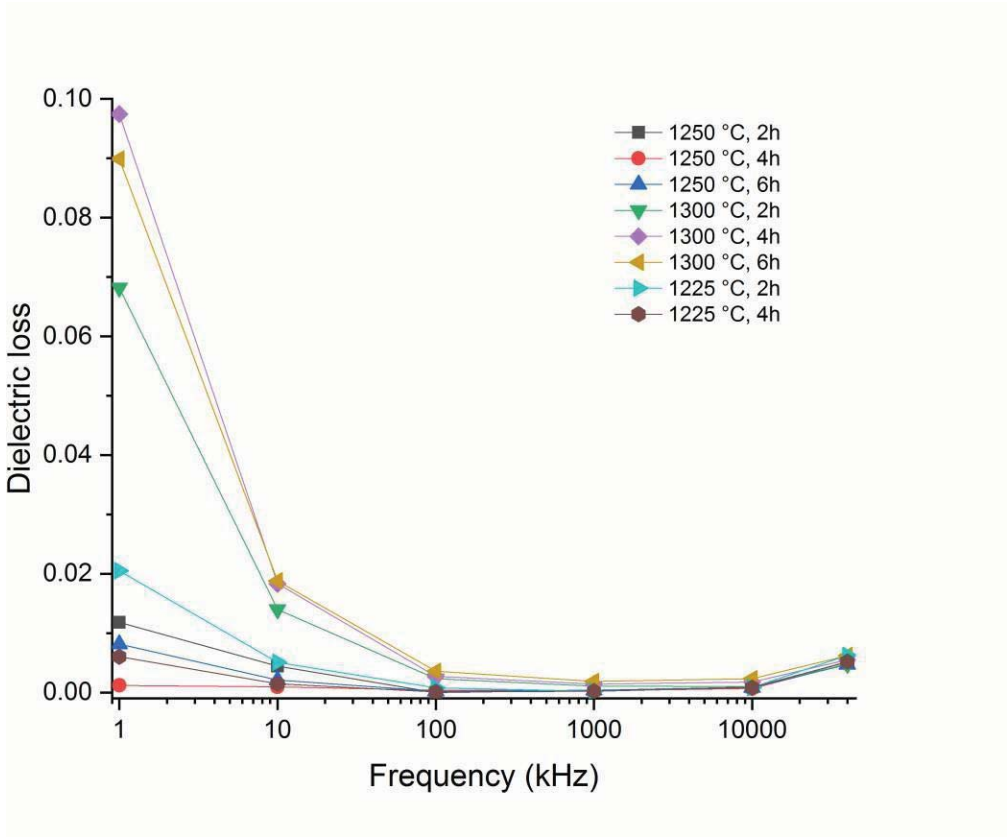

Figure 4.32. The variation dielectric loss with frequency for the $M_{0.95}CT$ ceramics sintered at different sintering conditions.

Huang et al. [8] investigated the effect of the CoO doping in MCT ceramics and obtained dielectric loss of ~7×10^{-5}. Huang et al. [10] studied also ZnO addition and obtained dielectric loss of ~8×10^{-5}. In this study, a lower dielectric loss value of ~3×10^{-4} was obtained. It should be mentioned that the dielectric loss measurements cannot

be done precisely at lower frequencies. In other studies [14, 15], all dielectric loss measurements were done at high frequencies in the range 7-9 GHz.

Conclusively, it was possible to fabricate $M_{0.95}CT$ ceramics with high density and improved dielectric properties without a sintering aid addition at low temperatures by the mixed oxide method.

4.2. Production of Zinc Borate added $M_{0.95}CT$ Ceramics

4.2.1. Powder Characterization

The $Zn_3B_2O_6$ powder used as sintering aid for $M_{0.95}CT$ ceramics was prepared in accord with the procedure described in Section 3.1.1. The XRD pattern of the $Zn_3B_2O_6$ powder is illustrated in Figure 4.33. All peaks in the pattern matched well with the JCPDS card number 37-1486, suggesting that the material is single phase $Zn_3B_2O_6$.

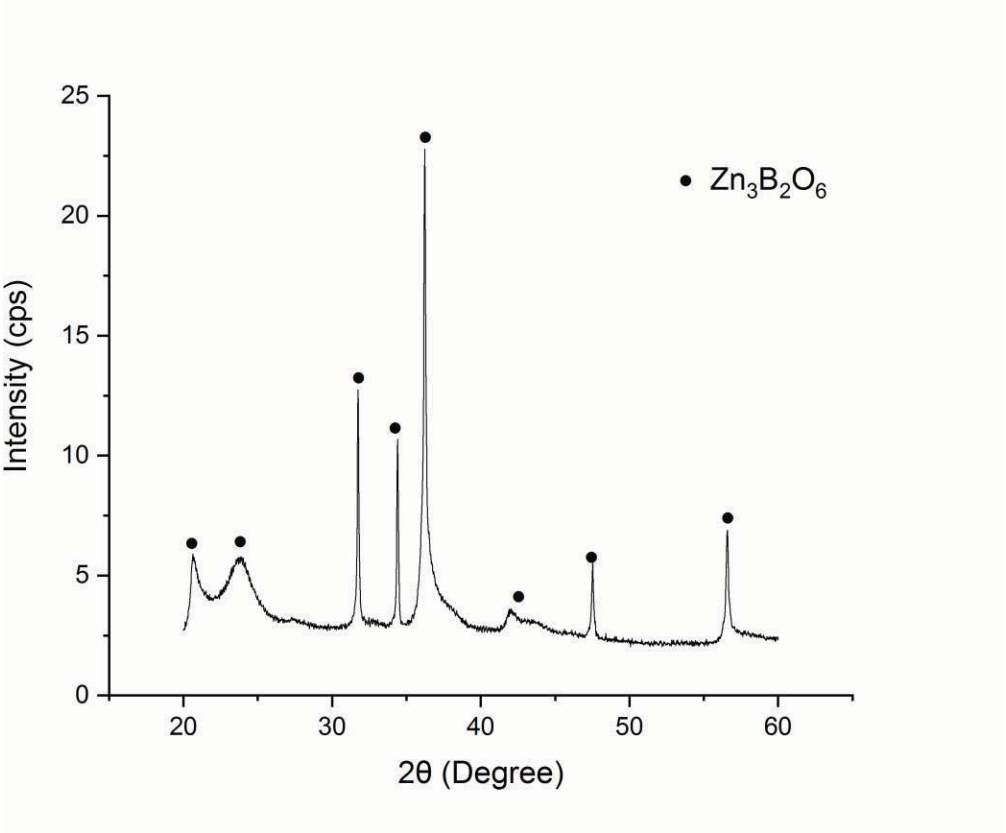

Figure 4.33. XRD pattern of prepared $Zn_3B_2O_6$ powder.

Figure 4.34 shows the SEM image of $Zn_3B_2O_6$ powder that was fired at 300 °C and removed from acid. $Zn_3B_2O_6$ powders have very fine particle size ranging from 0.5 to 1 μm. Nearly spherical shaped of particles were rather agglomerated.

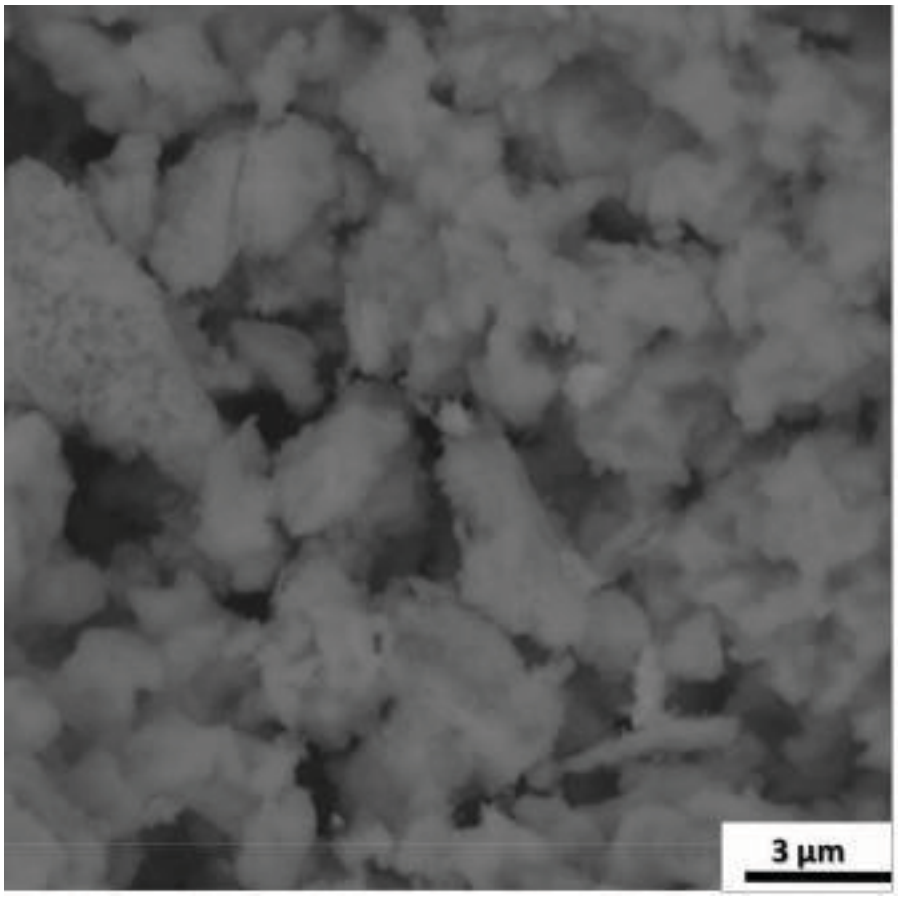

Figure 4.34. SEM image of $Zn_3B_2O_6$ powder.

Figure 4.35 illustrates the EDS spectrum of $Zn_3B_2O_6$ powder. Boron element was not detected because of its low photon energy and low x-ray yield. The low energy peaks of boron are close to the electronic noise of the detection system of EDS [55]. Since boron could not been detected in EDS, it was not possible to determine the exact chemical composition of $Zn_3B_2O_6$. The EDS spectrum of $Zn_3B_2O_6$ powder includes carbon that comes from coating applied prior to the analysis.

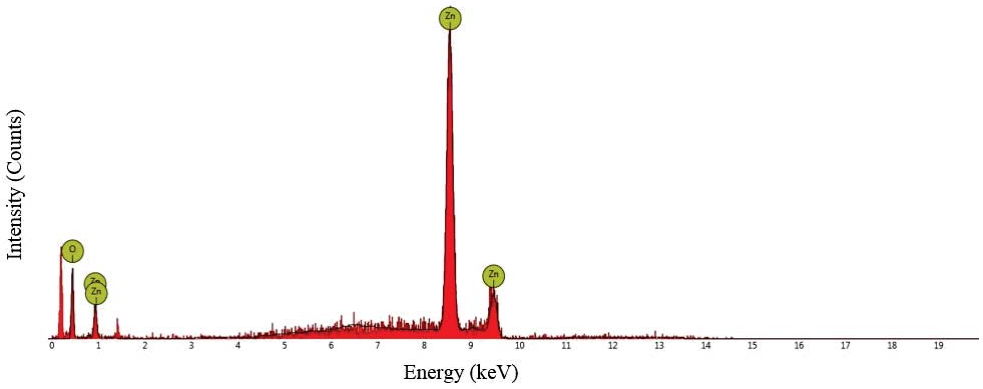

Figure 4.35. EDS spectrum of $Zn_3B_2O_6$ powder.

4.2.2. Sintering of $Zn_3B_2O_6$ added $M_{0.95}CT$ Ceramics

A 0.75 wt% $Zn_3B_2O_6$, hereafter will be called ZBO, added $M_{0.95}CT$ ceramic were simultaneously sintered and analyzed by high temperature XRD. High temperature XRD sintering profiles of the 0.75 wt% ZBO added $M_{0.95}CT$ ceramic is shown in Figure 4.36, Again, $MgTiO_3$ was identified as main crystalline phase while $CaTiO_3$ and $MgTi_2O_5$ phases were minor phases. $MgTi_2O_5$ was also detected as secondary phase. Graphite peaks in the patterns came from base plate. ZBO phase was not detected in the sintering profiles because i) its proportion is very less so that the instrument may not detect it, ii) doping into $MgTiO_3$ phase, iii) fast scanning speed.

Huang et al. [10] recognized the similarity of ionic radius of Zn^{2+} (0.083 nm) and Mg^{2+} (0.078 nm) cations. Mg^{2+} cations could easily interchange with Zn^{2+} cations. Therefore, the formation of $(Mg_{1-x}Zn_x)TiO_3$ compound is very likely for the MCT ceramics sintered in the presence of Zn^{2+} ions. Nonetheless, the occupying of Mg^{2+} ion positions by Zn^{2+} ions does not affect the lattice distortion because of the similarity in ionic size.

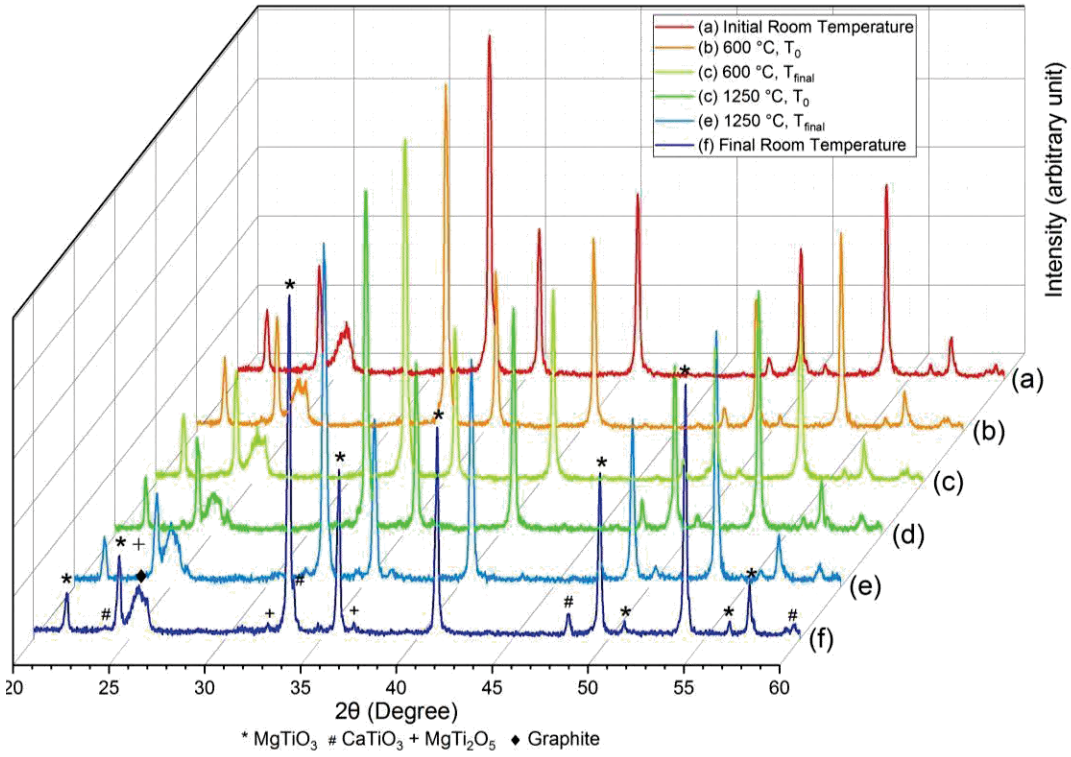

Figure 4.36. High temperature XRD sintering profile of the 0.75 wt% zinc borate added $M_{0.95}CT$ ceramic.

Figure 4.37 shows the XRD patterns of the $M_{0.95}CT$ ceramics sintered with various (0.00, 0.25, 0.50, 0.75, and 1.00 wt%) ZBO additions. All ZBO added $M_{0.95}CT$ ceramics were sintered at 1250 °C for 4 h in air. All XRD patterns suggest that $MgTiO_3$ formed as main crystalline phase; whereas, $CaTiO_3$ and $MgTi_2O_5$ phases formed as minor phases. $MgTi_2O_5$ formed as a intermediate phase during sintering. ZrO_2 was not detected due to the fast scanning rate of 4 °/min. It is clear that the intensity of the XRD peaks for the intermediate phase increased with increasing ZBO additions. However, no major shift in the XRD peaks of the $MgTiO_3$ phase was distinguished with increasing ZBO additions. Since a shift in the there XRD peaks of the $MgTiO_3$ phase was not noticed, and XRD did not detect any $(Mg_{1-x}Zn_x)TiO_3$, it is difficult to say anything about the formation of $(Mg_{1-x}Zn_x)TiO_3$ phase during sintering. Further analyses are needed to find out whether $(Mg_{1-x}Zn_x)TiO_3$ forms or not during sintering.

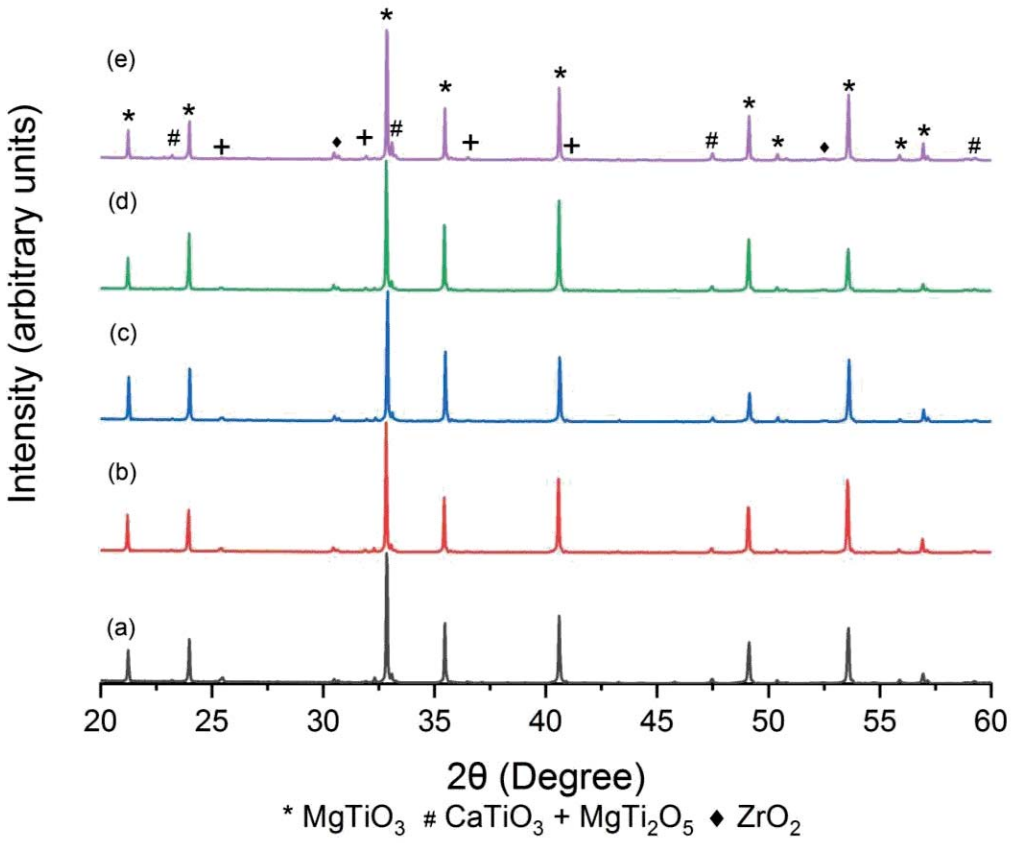

Figure 4.37. XRD patterns of the $M_{0.95}CT$ ceramics sintered at 1250 °C for 4 h with different ZBO additions. (a) 0.00 wt%, (b) 0.25 wt% (c) 0.50 wt%, (d) 0.75 wt%, and (e) 1.00 wt%.

The SEM images of $M_{0.95}CT$ ceramics sintered with different ZBO additions are illustrated in Figure 4.38. As the ZBO addition was increased, the grains become larger. The additive-free $M_{0.95}CT$ ceramic has grains of approximately 2-10 µm as shown in Figure 4.22. As stated earlier the shoulder at particle size distribution line of calcined $M_{0.95}CT$ powder caused the development of grains with various size. Fisher et al. [56] studied about abnormal grain growth for perovskite structure ceramics. They noticed that if facetted grain boundaries occur in structure with bimodal grain distribution, it causes the abnormal grain growth in perovskites.

Most of the grains in the microstructure of the $M_{0.95}CT$ ceramic sintered with 0.25 wt% ZBO additions were bigger than 10 µm. In 0.50 wt% ZBO added $M_{0.95}CT$ ceramic, grains were 15-20 µm. For 0.75 and 1.00 wt% ZBO additions, grain sizes of

$M_{0.95}CT$ ceramics exceed 30 µm. The grain boundaries begin to melt. The microstructure consisted of irregular shaped abnormally growth grains.

The SEM images taken from the fracture surface the $M_{0.95}CT$ ceramics sintered with different ZBO additions suggested that the ceramics had nonuniform grains in structure. The large and small grains marked in Figure 4.38(d) were analyzed using EDS analysis. The analysis data, presented in Table 4.9, recommended that the larger and irregular shaped grains were $MgTiO_3$ whereas, small and cuboid shaped grains located at the grain boundaries and within the $MgTiO_3$ grains were $CaTiO_3$.

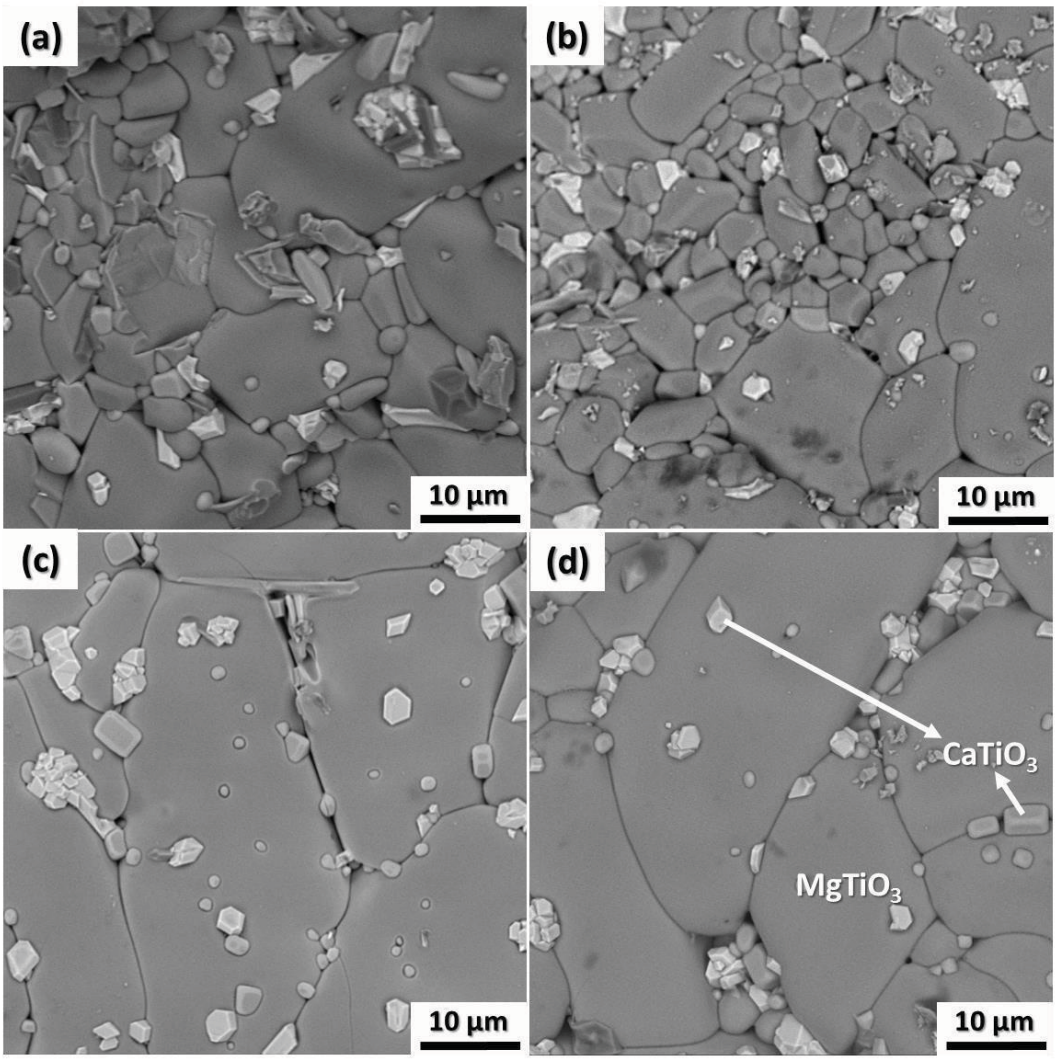

Figure 4.38. SEM images of the ZBO added $M_{0.95}CT$ ceramics sintered at 1250 °C for 4 h with different ZBO additions. (a) 0.25 wt%, (b) 0.50 wt%, (c) 0.75 wt%, and (d) 1.00 wt%.

Table 4.9. EDS analysis of the grains shown in Figure 4.38(d).

Element Symbol	$MgTiO_3$ Grain		$CaTiO_3$ Grain	
	Atomic Concentration (%)	Weight Concentration (%)	Atomic Concentration (%)	Weight Concentration (%)
O	65.58	45.77	66.44	42.20
Mg	17.37	18.42	0.92	0.89
Ti	15.88	33.16	16.58	31.50
Ca	0.61	1.07	15.74	25.05
Zn	0.55	1.58	---	---
Si	65.58	45.77	0.32	0.36

The EDS analysis data taken from the general view of the 1.00 wt% ZBO added-$M_{0.95}$CT ceramic is given in Table 4.10. A 1.06 wt% Zn was detected implying that ZBO additions were successfully made to $M_{0.95}$CT ceramic. Also small amount of Si and Zr were detected. The chemical composition determined by the EDS analysis is quite similar to the intended composition.

Table 4.10. *EDS analysis of 1 wt% ZBO-added $M_{0.95}$CT ceramic sintered at 1250 °C for 4 h.*

Element Symbol	Atomic Concentration (%)	Weight Concentration (%)
O	71.49	54.63
Mg	17.48	16.27
Ti	10.14	26.17
Ca	0.32	1.28
Zn	0.29	1.06
Si	0.17	0.38
Zr	0.11	0.21

In Table 4.11, XRF results of the 1.00 wt% ZBO-added $M_{0.95}$CT ceramic are given. The analyzed compositions was close to the intended composition in terms of the Ti, Mg, and Ca elements.

Table 4.11. *The XRF analysis of the 1.00 wt% ZBO-added $M_{0.95}CT$ ceramic.*

Element Symbol	Weight Concentration (%)
Ti	37.4
O	40.1
Mg	13.4
Ca	3.04
C	2.94
P	1.24
Si	0.901
Zn	0.729
Zr	0.152
Al	0.0889
Fe	0.0313

The microstructures of the ZBO added $M_{0.95}CT$ ceramics were compared with those of the ZnO and B_2O_3 added $M_{0.95}CT$ ceramics provided in the literature in Figure 4.39. It is obvious that ZnO addition alone resulted in the development of uniform size grains but, 2 wt% B_2O_3 additions resulted in abnormal grain growth. The microstructures of the $M_{0.95}CT$ ceramics prepared by B_2O_3 and ZBO additions were alike. It is obvious that additions of B_2O_3 alone or together with ZnO or ZBO compound trigger the grain growth in the $M_{0.95}CT$ ceramics.

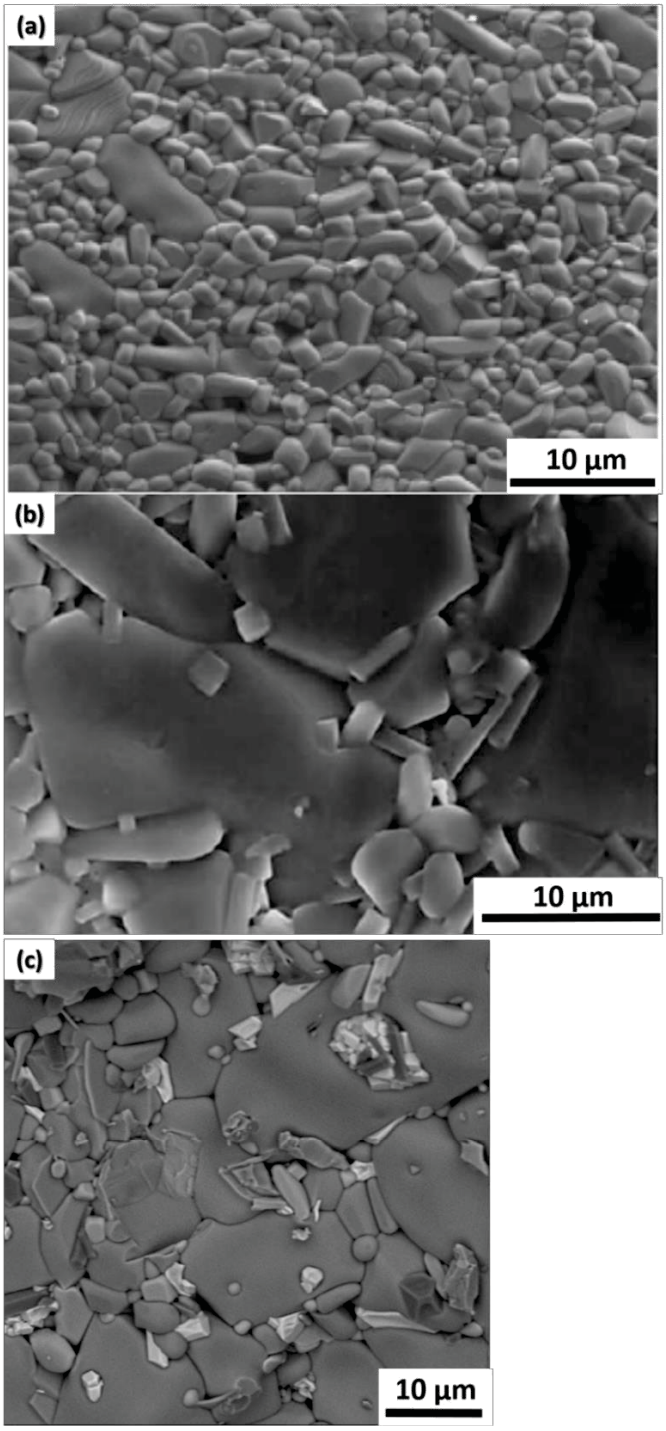

Figure 4.39. SEM images of the (a) 0.25 wt% ZnO added $M_{0.95}CT$ ceramic sintered at 1250 °C [9], (b) 2 wt% B_2O_3 added $M_{0.95}CT$ ceramic sintered at 1200 °C [2] and (c) 0.25 wt% ZBO added $M_{0.95}CT$ ceramic sintered at 1250 °C.

4.2.3. Properties of ZBO added $M_{0.95}CT$ Ceramics

4.2.3.1. Density

Figure 4.40 shows the sintered density of the additive-free $M_{0.95}CT$ ceramic and varios amount of ZBO added $M_{0.95}CT$ ceramics. The error bars in the figure represent the standard deviation from the averages. With increasing ZBO additions, the density of $M_{0.95}CT$ ceramics descreased from 3.82 g/cm^3 to 3.64 g/cm^3. The relative density of the additive-free, 0.25, 0.50, 0.75, and 1.00 wt% ZBO added $M_{0.95}CT$ ceramics were 97.5%, 95.2%, 95.1%, 92.8%, and 95.6%, respectively. The highest relative density was obtained for the additive-free $M_{0.95}CT$ ceramic. The inhomogeneous microstructure and abnormal grain growth with increasing ZBO addition caused a decrease in the densification. Therefore, when compared with the additive-free $M_{0.95}CT$ ceramic, lower densification occurred in the ZBO added $M_{0.95}CT$ ceramics. It is obvious that ZBO additions to MgO-CaO-TiO_2 system did not provide densification in $M_{0.95}CT$ ceramics, implying that it did not play the role of sintering aid. The sintered density values of ZBO added $M_{0.95}CT$ ceramics were listed in Table 4.12.

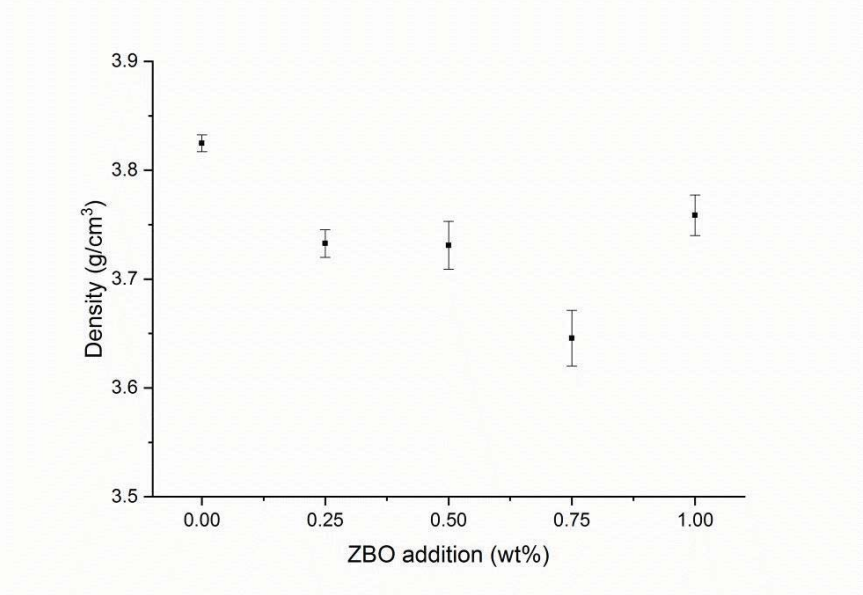

Figure 4.40. The sintered density of the $M_{0.95}CT$ ceramics sintered at 1250 °C for 4 h with different zinc borate additions: (a) 0.00 wt%, (b) 0.25 wt% (c) 0.50 wt%, (c) 0.75 wt%, (d) 1.00 wt%.

Table 4.12. *Bulk density of the ZBO added $M_{0.95}CT$ ceramics.*

ZBO Addition (wt%)	**Sintered Density (g/cm^3)**
0.00	3.82±0.006
0.25	3.73±0.008
0.50	3.73±0.01
0.75	3.64±0.02
1.00	3.75±0.009

The relative density and ε_r of the ZBO added $M_{0.95}CT$ ceramics as a function of ZBO additions were depicted in Figure 4.41. It is obvious that varied parallel to the density. As explained previously the microstructures with high sintered density provide the best dielectric properties since pores act as unwanted phase and do not have any contribution to the permittivity of the material.

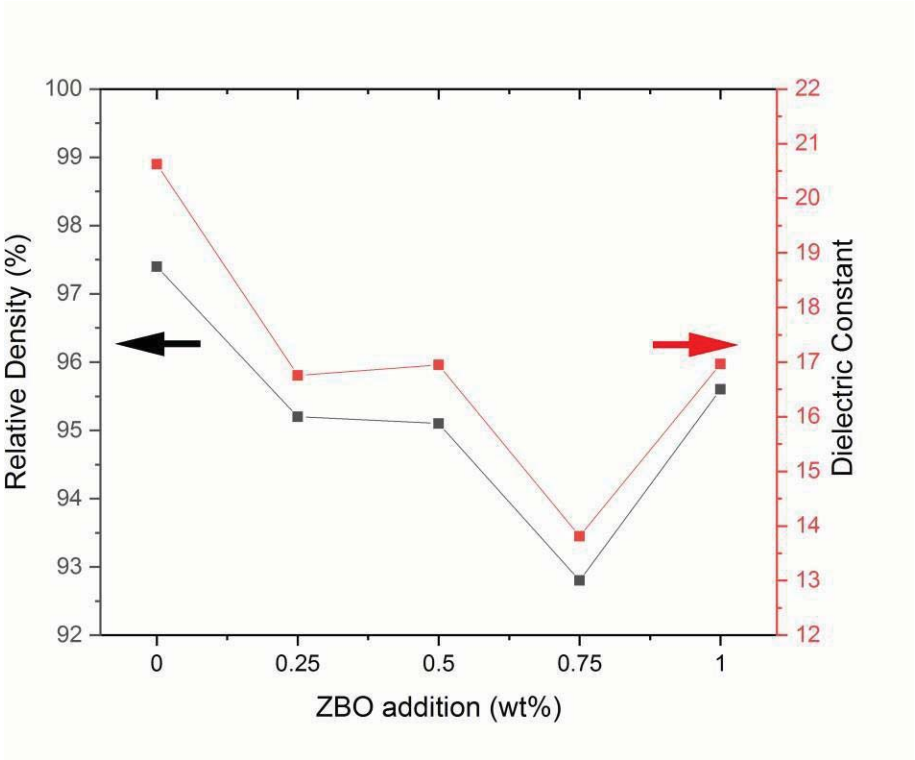

Figure 4.41. Relative density and dielectric constant of ZBO added $M_{0.95}CT$ceramics as a function of ZBO additions.

4.2.3.2. Dielectric Constant and Dielectric Loss

The highest value was obtained from the additive-free $M_{0.95}CT$ ceramics as illustrated in Figure 4.42. With increasing ZBO addition, dielectric constant decreased. The highest 16.9 was obtained for the 1.00 wt% ZBO-added $M_{0.95}CT$ ceramic. The decrease in is related with the polarization of cations per unit volume. As polarization increases per unit volume, the increases too. The polarizations of Mg^{2+}, Ca^{2+} and Zn^{2+} cations are 1.33×10^{-24} cm^3, 3.17×10^{-24} cm^3 and 0.78×10^{-24} cm^3, respectively [47]. Zn^{2+} cation have lower polarization compared to Mg^{2+} and Ca^{2+} present in the additive-free $M_{0.95}CT$ ceramic. Hence, decreased with increasing ZBO additions. At all frequencies, the values were almost constant with increasing frequencies. It is the proof of the reliable measurements of values.

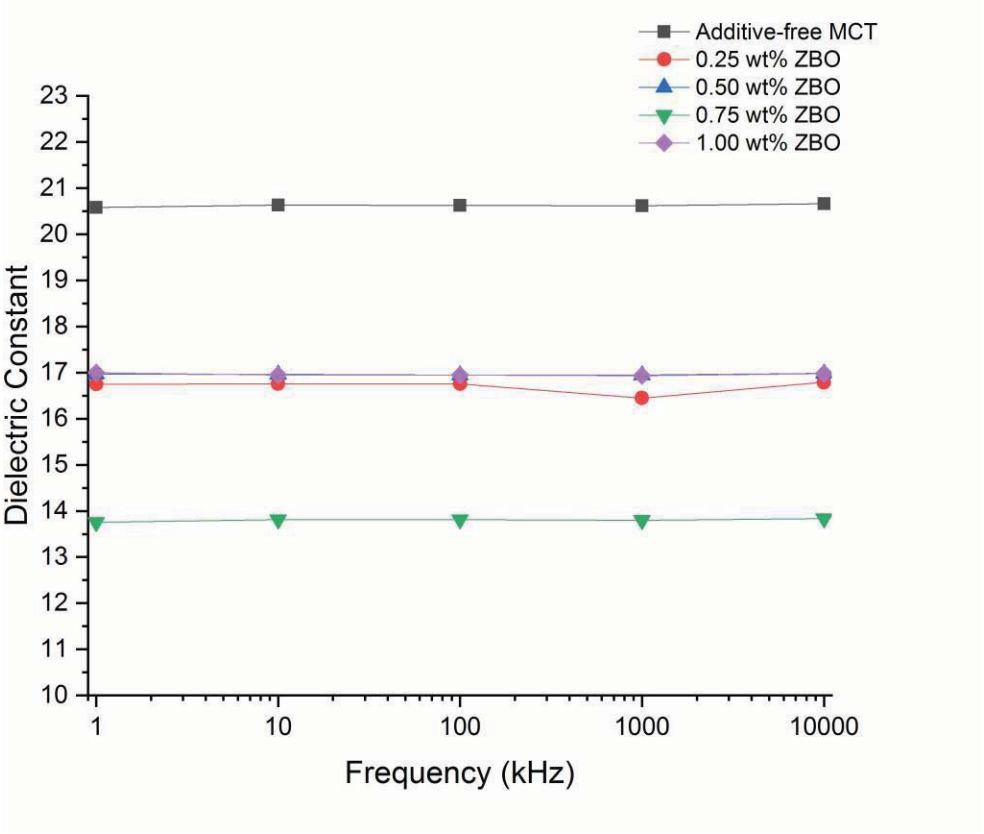

Figure 4.42. Dielectric constant of additive-free and ZBO added $M_{0.95}CT$ ceramics at different frequencies.

The relation between dielectric loss and testing frequency of $M_{0.95}CT$ ceramics with different ZBO additions from 1 kHz to 40 MHz is given in Figure 4.43. As ZBO addition increased, the dielectric losses of $M_{0.95}CT$ ceramics also increased. Additive-free $M_{0.95}CT$ ceramic provided the minimum dielectric loss compared with ZBO-added $M_{0.95}CT$ ceramics.

As ZBO amount was increased in $M_{0.95}CT$ structure, grain size increased too. It is commonly known that the domain size increases with increasing grain size [47]. Therefore, with decreasing grain boundaries the domain boundaries decreased. As a consequence, the dielectric loss increased.

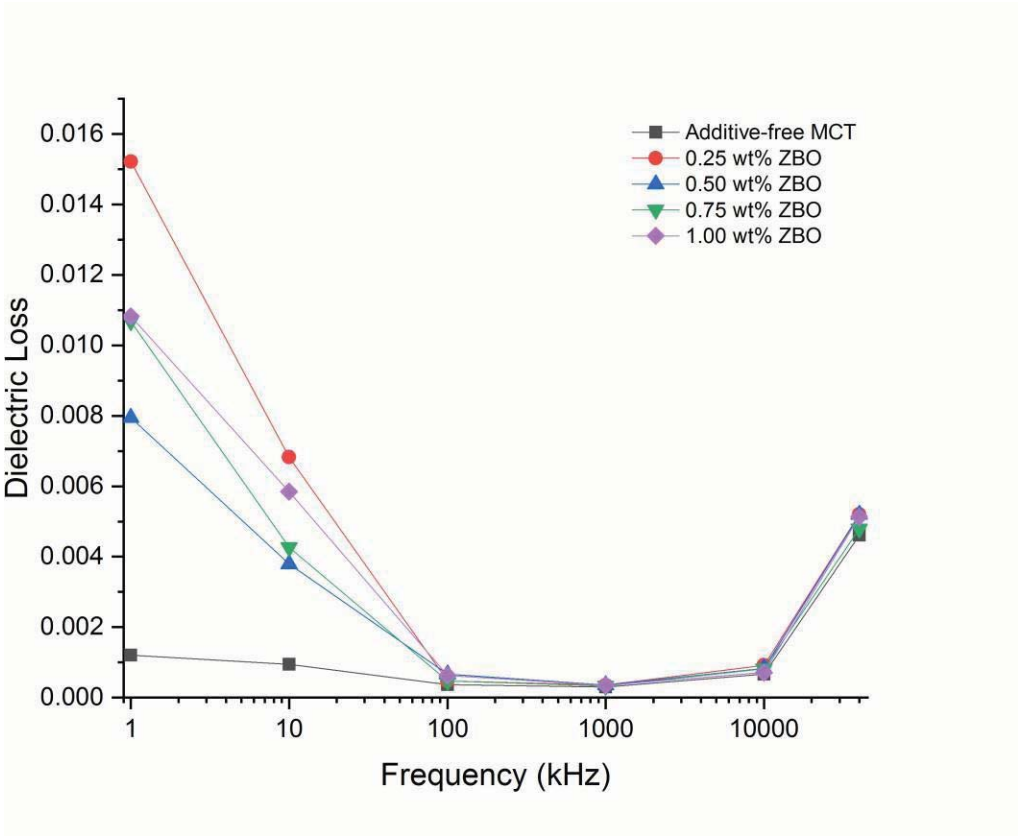

Figure 4.43. The relationship between dielectric loss and testing frequency of $M_{0.95}CT$ ceramics with different ZBO addition.

When compared to the studies reported in the literature, the results of this study prove that it is possible to fabricate $M_{0.95}CT$ ceramic with high density and optimum dielectric properties without a sintering aid addition at low temperatures.

A comparison of the results of this study with those of the selected studies reported in the literature was shown in Table 4.13. When compared to the selected studies, the highest densification was obtained with the additive-free $M_{0.95}CT$ ceramic. ZBO added $M_{0.95}CT$ ceramics have compatible density values with other studies. However, a lower ε_r was obtained. The dielectrical measurement was analyzed at different frequencies. At microwave frequencies it is possible to calculate more precise dielectrical results with different measurements techniques.

Table 4.13. *The effects of different sintering aids to $M_{0.95}CT$ ceramics.*

Sintering Aid (amount)	**Sintering Temperature (°C)**	**Frequency Range**	**Dielectric Constant**	**Density (g/cm^3)**	**Reference**
ZnO (1 wt%)	1300	7 GHz	20	3.2	[12]
ZnO (0.25 wt%)	1250	9.5 GHz	20.8	3.8	[11]
H_3BO_3 (0.50 wt%)	1220	Not given	21.54	3.7	[8]
B_2O_3 (2 wt %)	1200	8 GHz	21.2	3.72	[9]
ZBO (1.00 wt%)	1250	10 MHz	16.9	3.75	Present study
Pure $M_{0.95}CT$	1250	10 MHz	20.7	3.82	Present study

CHAPTER 5

CONLUSIONS

It is possible to fabricate $M_{0.95}CT$ ceramics with high density and improved dielectric properties without a sintering aid addition at low temperatures by the mixed oxide method. The microstructural studies of additive-free $M_{0.95}CT$ ceramic and ZBO added $M_{0.95}CT$ ceramics revealed that $M_{0.95}CT$ ceramics consist of $MgTiO_3$ main and $CaTiO_3$ minor phases. Unwanted $MgTi_2O_5$ intermediate phase is inhibited with an appropriate production practice and better densification conditions. The formation of main and minor phases was enhanced and unwanted intermediate phases were hindered before sintering by using nano size particles and by applying a regulated calcination process twice. Therefore, it is possible to obtain better densification at lower temperatures. Dielectric properties of ceramics are directly related to the microstructure as grain size and defects influence the dielectric properties. The microstructures with high sintered density provide the best dielectric properties. Dielectric properties was enhanced at lower sintering temperatures without a sintering aid. A relative density of 97.5%, a of 20.6 and a dielectric loss of 0.0003 (1 kHz-40 MHz) are obtained with additive-free $M_{0.95}CT$ ceramic sintered at 1250 °C for 4 h.

The incorporations of small amounts (0.25, 0.50, 0.75, and 1.00 wt%) of $Zn_3B_2O_6$ were made to the $MgO\text{-}CaO\text{-}TiO_2$ system as liquid phase sintering aid. The results revealed that $Zn_3B_2O_6$ is not a proper sintering aid for the $M_{0.95}CT$ ceramics since it causes the development of improper microstructure (large grain size, defects, unwnated phases etc.). Densification and dielectric constant of 0.75 wt% $Zn_3B_2O_6$ added $M_{0.95}CT$ ceramic decreased to 92% of theoretical density and 13.8, respectively but, dielectric loss increased to 0.0006.

FUTURE STUDIES

The dielectric property measurements in terms of dielectric constant and tanδ can be systematically done at microwave frequencies to observe dielectric behavior with increasing frequencies. In order to obtain more precise dielectric measurements with increasing frequency, an appropriate dielectric measurement method must be used.

Temperature coefficient of resonant frequency ( ) can be examined to obtain the temperature stability of ceramics at resonant frequency. It must be near-zero value.

The formation possibility of $(Mg_{1-x}Zn_x)TiO_3$ can be investigated to explain the microstructure-deielctric property relation in case of the presence of ZBO compound.

REFERENCES

[1] Wakino, K., Nishiwa, and T., Tamura, H. 1990. Dielectric resonator materials and their applications for mobile communication systems, British Ceramic Transactions and Journal, 89. 39-43.

[2] Huang, C. L., and Weng, M. H., 2001. Improved high Q value of $MgTiO_3$-$CaTiO_3$ microwave dielectric ceramics at low sintering temperature, Materials Research Bulletin, 36. 2741-2750.

[3] Wakino, K. 1989. Recent developments of dielectric resonator materials and filters, Ferroelectrics, 91. 69-86.

[4] Kell, R. C., and Greenham, G. C. E. 1973. High permittivity temperature stable ceramic dielectrics with low microwave loss, Journal of American Society, 56. 352.

[5] Li, L., Gao, Z., Liu, Y., Cai, H. and Li, S. 2015. Influence of $LaAlO_3$ additive to $MgTiO_3$-$CaTiO_3$ ceramics on sintering behavior and microwave dielectric properties, Materials Letters, 140. 5-8.

[6] Fang, Y., Miao, K., Feng, S., Cao, J., Wang, H., and Xu, S. 2012. Sintering behavior and microwave dielectric properties of 95MCT ceramics prepared from different size powders by sol-gel method, Advanced Materials Research, 557-559. 923-927.

[7] Pan, C. L., Shen, C. H., Lin, W. C., and Lin, S. H. 2014. Effect of B_2O_3 glass on the sintering and microwave dielectric properties of $MgTiO_3$-$CaTiO_3$, Applied Mechanics and Materials, 666. 27-30.

[8] Huang, C. L., Pan, C. L., and Hsu, J. F. 2002. Dielectric properties of (1-x)$(Mg_{0.95}Co_{0.05})TiO_3$-$xCaTiO_3$ ceramic system at microwave frequency, Materials Research Bulletin, 37. 2483-2490.

[9] Chen, Y. C., Tsao, S. M., Lin, C. S., Wang, S. C. and Chien, Y. H. 2009. Microwave dielectric properties of $0.95MgTiO_3$-$0.05CaTiO_3$ for application in dielectric resonator antenna, Journal of Alloys and Compounds, 471. 347-351.

[10] Huang, C. L., Hou, J. L., Pan, C. L., Huang, C. Y., Peng, C. W., Wei, C. H. and Huang, Y. H. 2008. Effect of ZnO additive on sintering behavior and microwave dielectric properties of $0.95MgTiO_3$-$0.05CaTiO_3$ ceramics, Journal of Alloys and Compounds, 450. 359-363.

[11] Huang, C. L., Pan, C. L., and Shium, S. J. 2002. Liquid phase sintering of $MgTiO_3$-$CaTiO_3$ microwave dielectric ceramics, Materials Chemistry and Physics, 78. 111-115.

[12] Ichinose, N., and Yamamoto, H. 1997. Effect of additives on microwave dielectric properties in low temperature firing $(Mg,Ca)TiO_3$ based ceramics, Ferroelectrics, 201. 255-262.

[13] Ferreira, V. M., Azough, F. Freer, R., and Baptista, J. L. 1997. The effect of Cr and La on $MgTiO_3$ and $MgTiO_3$-$CaTiO_3$ microwave dielectric ceramics, Journal of Materials Research, 12. 3293-3299.

[14] Huang, C. L. and Pan, C. L, 2002. Low temperature sintering and microwave dielectric properties of $(1-x)MgTiO_3$-$xCaTiO_3$ ceramics using bismuth addition, Japanese Journal of Applied Physics, 41. 707-711.

[15] Li, L., Gao, Z., Liu, Y., Cai, H. and Li, S. 2015. Influence of $LaAlO_3$ additive to $MgTiO_3$-$CaTiO_3$ ceramics on sintering behavior and microwave dielectric properties, Materials Letters, 140. 5-8.

[16] Wang, K., Zhou, H., Sun, W., Chen, X., and Ruan, H. 2018. Solid-state reaction mechanism and microwave dielectric properties of $0.95MgTiO_3$-$0.05CaTiO_3$ ceramics, Journal of Materials Science, 29. 2001-2006.

[17] Dong, Li., Dong, G., Li. Y. and Zhang, X. 2014. Preparation and investigation on properties of the $MgTiO_3$-$CaTiO_3$ microwave ceramic materials, Advanced Materials Research, 997. 419-423.

[18] Sebastian, M. T. 2008. Dielectric materials for wireless communication, Publication of Elsevier.

[19] Gurov, V. A. 2008. Solid-state electronics, Moscow, Tekhnosfera, 19.

[20] Callister, W. D-Jr., and Rethwisch D. 2009. Materials Science and Engineering: An Introduction 8. Ed. Newyork, USA, Wiley Publication.

[21] Kingery, W. D., Bowen, H. K., and Uhlmann, D. R., 1975. Introduction to ceramics 2nd Ed. Newyork, USA, Wiley Publication.

[22] Harrop, P.J. 1972. Dielectrics, London, England, Butterworth Publishers.

[23] Sirdeshmukh, D. B., Sirdeshmukh, L., and Subhadra, K. G. 2006. Micro- and Macro-Properties of Solids: Thermal, Mechanical and Dielectric Properties, Berlin, Heidelberg: Springer.

[24] Chen, L. F., Ong, C. K., Neo, C. P., Varadan, V. V. and Varadan, V. K. 2004.Microwave Electronics: Measurement and Material Characterization, John Wiley & Sons Publication.

[25] Webster, J. (ed.), 1999. Dielectrics and Electrical Insulation, Detroit, USA, Wiley Publication.

[26] Büyüköztürk, O., Yu, T. Y., and Ortega, J. A. 2006. A methodology for determining complex permittivity of construction materials based on transmission-only coherent, wide-bandwidth free-space measurements, Cement&Concrete Composites, 28. 349-359.

[27] Anderson, C. 2006. Determining the complex permittvity of materials with waveguide-cutoff method, Baylor University, Degree Programme in Electrical and Computer Engineering, Master's Thesis.

[28] Geyer, R. G. 1990. Dielectric Characterization and Reference Materials. Technical Note 1338, National Institute of Standards and Technology.

[29] Burtfoot, J. C. 1967. Ferroelectrics: An introduction to the physical principles. Van-Nostrand-Reinbold, London.

[30] Regmi, A. 2016. Reflection measurement of building materials at microwaves, University of Oulu, Degree programme in Wireless Communication Engineering. Master's Thesis, 17 p.

[31] Kremer, F., and Schönhals, A. 2003. Broadband Dielectric Spectroscopy, Berlin, Heidelberg: Springer.

[32] Moulsen, A. J. and Herbert, J. M. 1999. Electroceramics, Materials, Properties and Application. Chapman and Hall, London, 1st Edition.

[33] Petzelt, J., Pacesova S., Fousek, J. Kamba, S. and Zeleny V. 1989. Dielectric spectra of some ceramics for microwave applications in the range 1010-1014 Hz, Ferroelectrics, 77-85, 1989.

[34] Tang, K., Wu, Q. and Xiang, X. Y. 2012. Low temperature sintering and microwave dielectric properties of zinc silicate ceramics, Journal of Materials Science: Material Electron, 23. 1099-1102.

[35] Agilent-Technologies. 2006. Basics of measuring the dielectric properties materials of material.

[36] Jilani, M. T., Rehman, M. Z., Khan, A. M., Khan, M. T. and Ali, S. M. 2012. A Brief of measuring techniques for characterization of dielectric materials. ITEE Journal, 1. 1.

[37] A. P. G. a. R. N. C. 2006. A Review of RF and microwave techniques for dielectric measurement on polar liquids, IEEE Transactions on Dielectric and Electrical Insulation, 13. 727-743.

[38] Rahaman, M. N. 2003. Ceramic Porcessind and Sintering, Marcel Decker, New York.

[39] Wang, F. Y. F. 1976. Treatise on Materials DScience and Technology: Ceramic Fabrication Processes. Academic Press, New York. 9.

[40] Fahrenholtz, W. G., 2004. Ceramic Engineering 111 Sintering. Ceramic Engineering Department, University of Missouri-Rolla.

[41] Kalem, V. 2011. Development of piezoelectric ceramics for ultrasonic motor applications, Middle East Technical University.

[42] Shannon, R. D. 1976. Revised effective ionic radii and systematic studies of interatomic distances in halides and chalcogenides, Acta Crystallographia, A32. 751-767.

[43] Baek, J. G., Isobe, T. and Senna, M. 1996. Mechanochemical effects on the precursor formation and microwave dielectric characteristics of $MgTiO_3$, Solid State Ionics, 90. 269-279.

[44] Liou, Y. C. and Yang, S. L. 2007. Calcium doped $MgTiO_3$- $MgTi_2O_5$ ceramics prepared using a reaction- sintering process, Materials Science and Engineering B, 142. 116-120.

[45] German, R. M. Sintering Theory and Practice. 1996. Wiley, New York.

[46] Witherspoon, K. C., Cross, B. J. and Hellested, M. D. 2013.Combşned electron and X-ray excitation for spectrometry in the SEM. Microcopy Today, 8. 21-24.

[47] Pendleton, M. W., Washburn, D. K., Ellis, E. A. and Pendleton, B. B. 2014. Comparing the Detection of Iron-Based Pottery Pigment on a Carbon-Coated Sherd by SEM-EDS and by Micro-XRF-SEM. Yale Journal of Biology and Medicine, 87. 15-20.

[48] Piagai, R., Kim, I., Park, J. and Kim, Y. 1998. Microwave dielectric properties of Magnesium Calcium Titanate ceramics prepared by semi-alkoxide methods, Journal of Korean Society, 32. 367-370.

[49] Silverman, B. D. 1962. Microwave Absorption in Cubic strontium Titanate, Phys. Rev. 125. 1921.

[50] Lowndes, R. Structural and Microwave Dielectric Properties of Ceramics of $Ca_{(1-x)}Nd_{2x/3}TiO_3$. 2012. Master Thesis, University of Manchester, Manchester.

[51] Dorey, R. Ceramic Thick Films for MEMS and Microdevices. 2012. Publication of Elsevier.]

[52] Keysight Technologies. Basics of measuring the dielectric properties of materials. Application Note. Literature Number: 5989-2589EN.

[53] Wum, X. G., Wang, Chen, Y. H. and Zhou, D.. 2012. Synthesis and microwave dielectric properties of $Zn_3B_2O_6$ ceramics for substrate application. Journal of American Society, 95. 1793-1795.

[54] Valant, M., Suvorov, D., Pullar, R. C., Sarma, K. and Alford, N. M. 2006. A mechanism for low-temperature sintering. Journal of European Ceramic Society, 26. 2777-2783.

[55] Bastin, G. F. and Heijligers, H. J. M. 1986. Quantitative electron probe microanalysis of boron in binary borides. Publication of the Laboratory for Physical Chemistry, 111.

[56] Fisher, J. G., Kim, M. S., Lee, H. Y. and Kang, S. J. L. 2004. Effect of Li_2O and PbO additions on abnormal grain in the $Pb(Mg_{1/3}Nb_{2/3})O_3$-35 mol% $PbTiO_3$ system, Journal of American Ceramic Society, 87. 937-942.

APPENDICES

Theoretical density of $0.95MgTiO_3$-$0.05CaTiO_3$ ceramic was calculated according to lattice crystallographic parameters given in the PDF card of $MgTiO_3$ (a=5.054 Å, c=13.898 Å), of $CaTiO_3$ (a=5.380 Å, b=5.4337 Å, c=7.6269 Å). $MgTi_2O_5$ was not considered in calculations because it occurred very small amount in structure. The volume unit cells of $MgTiO_3$ and $CaTiO_3$ were obtained as 307.4×10^{-24} cm^3 and 222.4×10^{-24} cm^3, respectively from the PDF cards. $MgTiO_3$ has 6 atoms in each unitcell; whereas, $CaTiO_3$ has 4 atoms in each unitcell. Theoretical densities of each compound were calculated seperately and multiply with the molar ratios of $MgTiO_3$ and $CaTiO_3$. Consequently, of $0.95MgTiO_3$-$0.05CaTiO_3$ ceramic was calculated as $3.92g/cm^3$.

$$= \frac{\cdot}{\cdot}$$

where Z: Number of atoms associated with each unit cell

: Atomic weight

V: Volume of unit cell

: Avogadro's number (6.022×10^{23} atoms/mol